

## ABSTRACT

Convection from Manufactured Ice Roughness with Varying Flux Boundary Conditions

Christopher Wade Walker, M.S.M.E.

Committee Chairperson: Stephen T. McClain

It is well understood that aircraft wing icing adds weight, increases drag coefficients, decreases lift coefficients, and reduces stall margin, which can lead to aircraft accidents. To predict the shape of these ice accretions, codes, such as the NASA LEWICE code, have been created that step through time and solve an energy balance for an iced airfoil. A critical part of this energy balance is convection over the initial ice roughness. However, determining the convective heat transfer over the initial ice roughness is difficult. Previous methods have been developed for measuring the convective heat transfer for ice roughness with constant thermal boundary conditions. This work investigates the effect of variable heat flux boundary conditions on convective heat transfer, and improves upon the techniques used to obtain convective heat transfer measurements for realistic ice roughness patterns.

Convection from Manufactured Ice Roughness with Varying Flux Boundary Conditions

by

Christopher Wade Walker, B.S.M.E.

A Thesis

Approved by the Department of Mechanical Engineering

---

William Jordan, Ph.D., Chairperson

Submitted to the Graduate Faculty of  
Baylor University in Partial Fulfillment of the  
Requirements for the Degree  
of  
Master of Science in Mechanical Engineering

Approved by the Thesis Committee

---

Stephen T. McClain, Ph.D., Chairperson

---

Lesley M. Wright, Ph.D.

---

Yang Li, Ph.D.

Accepted by the Graduate School

August 2014

---

J. Larry Lyon, Ph.D., Dean

Copyright © 2014 by Christopher Wade Walker

All rights reserved

## TABLE OF CONTENTS

LIST OF FIGURES	viii
LIST OF TABLES	xiv
NOMENCLATURE	xv
ACKNOWLEDGMENTS	xviii
DEDICATION	xx
CHAPTER ONE	1
Introduction	1
Motivation	1
Objectives of Work	3
Presentation Outline	4
CHAPTER TWO	5
Technical Background and Literature Review	5
Heat Transfer and Fluid Mechanics	5
Boundary Layers	5
Roughness	9
Aircraft Icing Background	10
Icing Terms	10
Icing Process	10
Literature Review	13
Early Icing Studies	13



Recent Icing Studies	19
Icing Roughness Studies	23
Icing Tunnel Roughness Studies	23
Heat Transfer Studies	27
Summary of Literature Review	38
CHAPTER THREE	42
Materials and Methodology	39
Roughness Experiments	39
Materials	39
Roughness Test Plate	41
Test Plate Structure	43
Wiring and Thermocouples	43
Mylar Film	46
Tail	47
Roughness Panels	48
Infrared Camera	55
Traversing System	56
IR Window System	57
Pitot-Static Probe	57
Measurement Cart	58
Labview Monitoring	59
Baylor University Subsonic Wind Tunnel	59
Z-series Inlet Measurements	60

Thermal Boundary Layer Probe	60
Methods	60
Heat Transfer Experiment	61
Thermal Boundary Layer Traces	63
Transmissivity Experiment	64
Materials	65
Transmissivity Test Plate	66
Methods	68
Plexiglas Thermal Conductivity	69
Materials	69
Methods	72
CHAPTER FOUR	74
Data Reduction and Uncertainty Analysis	74
Transmissivity Experiment	74
Thermal Conductivity Experiment	75
Data Reduction	75
Uncertainty Analysis	76
Roughness Experiments	77
Data Reduction	77
Heat Transfer Experiments	77
Smooth Roughness Panel Validation	80
Air Properties	86
Thermocouple Calibration	86

Thermal Boundary Layer Traces	87
Uncertainty Analysis	87
CHAPTER FIVE	90
Results and Discussion	90
Transmissivity Experiment Results	90
Thermal Conductivity Experiment Results	92
Roughness Experiment Results	93
Heat Transfer Experiments	93
Thermal Boundary Layer Traces	112
CHAPTER SIX	116
Conclusions	116
Summary of Work	116
Future Work	117
APPENDICES	119
Appendix A	120
Appendix B	128
Appendix C	147
Appendix D	165
REFERENCES	169

## LIST OF FIGURES

Figure 1.1:	Energy balance on an unheated airfoil [2]	2
Figure 2.1:	Velocity boundary layer	5
Figure 2.2:	Thermal boundary layer	6
Figure 2.3:	Flat plate in parallel flow for a) constant heat flux and b) unheated starting length [6]	8
Figure 2.4:	Viscous and thermal boundary layers for varying heat flux conditions [6]	8
Figure 2.5:	Enhancement relative to the unperturbed boundary layer [7]	9
Figure 2.6:	Ice accretion scheme for an unswept wing [9]	11
Figure 2.7:	Ice accretion scheme for a swept wing [10]	12
Figure 2.8:	Feathers developing on an airfoil [11]	12
Figure 2.9:	Horn icing on an airfoil [12]	13
Figure 2.10:	Formation of scallops on an airfoil [11]	13
Figure 2.11:	Wilder correlation agreement with experimental results [15]	15
Figure 2.12:	Different types of icing for common icing parameters [15]	16
Figure 2.13:	“Shadow effect” illustrated [17]	17
Figure 2.14:	Regions of the “lobster tail” [17]	18
Figure 2.15:	Ice formation at different temperatures [8]	19
Figure 2.16:	Illustration of critical distance [19]	20
Figure 2.17:	Critical distance at different sweep angles with varying LWC [19]	21
Figure 2.18:	Critical distance at different sweep angles with varying temperature [19]	21

Figure 2.19	Effect of sweep angle on critical distance at various velocities [20]	22
Figure 2.20:	Smooth zone illustrated [9]	24
Figure 2.21:	Roughness diameter vs. freezing fraction [9]	24
Figure 2.22:	Smooth-zone width vs. accumulation parameter [9]	25
Figure 2.23:	Accumulation parameter vs. non-dimensional zone-width [25]	26
Figure 2.24:	Roughness element growth [11]	27
Figure 2.25:	Nusselt number comparison for horn accretions vs. a clean airfoil [28]	28
Figure 2.26:	One systematic roughness pattern used in Poinsatte [29]	29
Figure 2.27:	Frossling numbers along the surface for various flight tests [29]	30
Figure 2.28:	Systematic roughness elements used [30]	30
Figure 2.29:	Enhancement with varying Reynolds number [30]	31
Figure 2.30:	Enhancement with varying turbulence intensity [30]	31
Figure 2.31:	Mildly rough glaze cast [31]	32
Figure 2.32:	Test setup [31]	33
Figure 2.33:	Frossling numbers of the surface [31]	33
Figure 2.34:	Test setup [7]	33
Figure 2.35:	Roughness elements used [7]	33
Figure 2.36:	Energy balance used [7]	34
Figure 2.37:	Enhancement over a single element [7]	34
Figure 2.38:	Enhancement relative to the unperturbed boundary layer [7]	34
Figure 2.39:	ES-DEM model compared to Henry [32]	35
Figure 2.40:	Rime icing heat transfer coefficients [33]	36
Figure 2.41:	Glaze icing heat transfer coefficients [33]	36

Figure 2.42:	Rapid prototyped realistic roughness model [34]	37
Figure 2.43:	Convective contour map for realistic ice roughness [5]	37
Figure 3.1:	Test setup for a) heat transfer tests b) thermal boundary layer Traces	40
Figure 3.2:	Roughness test plate [5]	42
Figure 3.3:	Roughness test plate side view [5]	42
Figure 3.4:	Roughness panels removed	42
Figure 3.5:	Test plate structure [5]	44
Figure 3.6:	Thermocouple and Mylar film locations, dimensions in inches [5]	45
Figure 3.7:	Roughness test plate wiring diagrams [5]	45
Figure 3.8:	Gold deposited Mylar film between copper electrodes	46
Figure 3.9:	Tail fin	47
Figure 3.10:	Finished roughness panel from the 053096 pattern	48
Figure 3.11:	Coding diagram for the Lagrangian droplet simulator	49
Figure 3.12:	a) Raw simulator output, b) truncated results, c) truncated and stretched results, d) truncated, stretched, and scaled results	50
Figure 3.13:	Simulator data transformation to fill the entire test plate [5]	52
Figure 3.14:	052996 Solidworks model roughness scheme with row and column nomenclature	53
Figure 3.15:	Copmleted roughness panels for the a) turbulent calibration, b)052996 pattern, and c) 053096 pattern	55
Figure 3.16:	FLIR SC4000 IR camera	55
Figure 3.17:	Traversing system for the a) IR camera and b) thermal boundary layer probe	56
Figure 3.18:	a) IR windows and b) window support system	57

Figure 3.19:	a) Current transducers, b) DAQ modules, c) power sources, and d) whole cabinet	59
Figure 3.20:	Thermocouple probe and traversing system	60
Figure 3.21:	Test section covered with black felt shroud	62
Figure 3.22:	General test setup for the transmissivity experiment	65
Figure 3.23:	Transmissivity test plate	66
Figure 3.24:	Large thermocouple created in-house	67
Figure 3.25:	Thermal conductivity plates	70
Figure 3.26:	Thermal conductivity plate after grinding off excess epoxy	71
Figure 3.27:	Thermal conductivity plates	71
Figure 3.28:	Increase in validity of 1-D assumption with jet impingement	72
Figure 3.29:	Thermal conductivity plates during testing	73
Figure 4.1:	Energy balance for the thermal conductivity experiment	75
Figure 4.2:	Thermal circuit for the thermal conductivity experiment	75
Figure 4.3:	Visual 1-D energy balance for roughness test plate	77
Figure 4.4	Smooth-laminar temperature profile (K)	81
Figure 4.5:	Smooth-laminar convective map ( $\text{W}/\text{m}^2\text{K}$ )	81
Figure 4.6:	Smooth-laminar $\pm 0.5''$ average centerline (raw results)	82
Figure 4.7:	Smooth-turbulent temperature profile (K)	82
Figure 4.8:	Smooth-turbulent convective map ( $\text{W}/\text{m}^2\text{K}$ )	83
Figure 4.9	Smooth-turbulent $\pm 0.5''$ average centerline (raw results)	83
Figure 4.10:	Smooth-laminar $\pm 0.5''$ average centerline (finalized results)	85
Figure 4.11:	Smooth-turbulent $\pm 0.5''$ average centerline (finalized results)	85

Figure 5.1:	IR-Thermocouple Comparison	91
Figure 5.2:	Legend for thermocouple temperatures in Table 5.1	93
Figure 5.3:	Convective heat transfer map for smooth-laminar with a) constant heat flux, b) decreasing heat flux, c) increasing heat flux, and d)unheated starting length	94
Figure 5.4:	Convective heat transfer map for smooth-turbulent with a) constant heat flux, b) decreasing heat flux, c) increasing heat flux, and d) unheated starting length	95
Figure 5.5:	Convective heat transfer map for 052996 (Large Roughness) with a) constant heat flux, b) decreasing heat flux, c) increasing heat flux, and d) unheated starting length	96
Figure 5.6:	Convective heat transfer map for 053096 (Small Roughness) with a) constant heat flux, b) decreasing heat flux, c) increasing heat flux, and d) unheated starting length	97
Figure 5.7:	One inch lateral average along the test plate for smooth-laminar a) constant heat flux, b) decreasing heat flux, c) increasing heat flux, and d) unheated starting length	98
Figure 5.8:	One inch lateral average along the test plate for smooth-turbulent a) constant heat flux, b) decreasing heat flux, c) increasing heat flux, and d) unheated starting length	99
Figure 5.9:	One inch lateral average along the test plate for 052996 (Large Roughness) a) constant heat flux, b) decreasing heat flux, c) increasing heat flux, and d) unheated starting length	100
Figure 5.10:	One inch lateral average along the test plate for 053096 (Small Roughness) a) constant heat flux, b) decreasing heat flux, c) increasing heat flux, and d) unheated starting length	101
Figure 5.11:	Thermocouple pair legend	102
Figure 5.12:	Smooth-laminar convective coefficients for varying heat flux boundary conditions	105
Figure 5.13:	Smooth-turbulent convective coefficients for varying heat flux boundary conditions	105
Figure 5.14:	053096 convective coefficients for varying heat flux boundary conditions	106



Figure 5.15:	052996 convective coefficients for varying heat flux boundary conditions	106
Figure 5.16:	Smooth-laminar Stanton numbers for varying heat flux boundary conditions	107
Figure 5.17:	Smooth-turbulent Stanton numbers for varying heat flux boundary conditions	107
Figure 5.18:	053096 Stanton numbers for varying heat flux boundary conditions	108
Figure 5.19:	052996 Stanton numbers for varying heat flux boundary conditions	108
Figure 5.20:	Enhancement ratio for the rough surfaces relative to the constant flux and unheated starting length smooth surface theoretical predictions	111
Figure 5.21:	Nondimensinoal thermal boundary layer traces for the smooth-turbulent a) constant heat flux, b) decreasing heat flux, c) increasing heat flux, and d) unheated starting length	113
Figure 5.22:	Nondimensinoal thermal boundary layer traces for the 052996 a) constant heat flux, b) decreasing heat flux, c) increasing heat flux, and d) unheated starting length	114
Figure 5.23:	Nondimensinoal thermal boundary layer traces for the 053096 a) constant heat flux, b) decreasing heat flux, c) increasing heat flux, and d) unheated starting length	115
Figure 5.24:	052996 section two thermal boundary layer trace comparison	116
Figure 5.25:	053096 section two thermal boundary layer trace comparison	116

## LIST OF TABLES

Table 3.1	Key parameters of the “052996 Run 4” case at various stages of conditioning [5]	51
Table 3.2:	Key parameters of the “053096 Run 1” case at various stages of conditioning [5]	51
Table 3.3:	Target heat flux values to be matched for boundary conditions	63
Table 4.1:	Conduction correction coefficient values	84
Table 4.2:	Uncertainty calculations for each parameter in data reduction	89
Table 5.1:	IR-Thermocouple Comparison for Transmissivity Experiment	90
Table 5.2:	Data from Thermal Conductivity Experiment	92
Table 5.3:	Convective heat transfer coefficients for each roughness pattern	103
Table 5.4:	Stanton numbers for each roughness pattern (all values have been multiplied by $10^3$ )	104

## NOMENCLATURE

$A_c$	Accumulation parameter
$A_t$	Total heater cross-sectional area
$B_T$	Correlated uncertainty
$c$	Chord length
$c_c$	Conductive correction coefficient for the $c^{\text{th}}$ section (1, 0.9, 1.05, 1.1, 1.05)
$D$	Roughness element diameter
$d_{cr}$	Critical distance
$D_{\text{mean}}$	Average roughness element diameter
$E$	Voltage
$h$	Convective heat transfer coefficient
$H$	Roughness element height
$h_{\text{lam}}$	Theoretical flat plate laminar convective heat transfer coefficients
$h_{\text{turb}}$	Theoretical flat plate turbulent convective heat transfer coefficients
$I$	Current
$k_f$	Fluid thermal conductivity
$k_p$	Plexiglas thermal conductivity
$L_{\text{ha}}$	Length of heated area
$N$	Number of samples of data set
$Nu$	Nusselt number
$P$	Roughness element spacing

$P_{\text{mean}}$	Average roughness element spacing
$Pr$	Prandtl number
$q_{\text{cond}}''$	Conductive heat flux
$q_{\text{conv}}''$	Convective heat flux
$q_{\text{gen}}''$	Heat flux generation
$q_{\text{rad}}''$	Radiation heat flux
$q_w''$	Wall heat flux
$Re$	Reynolds number
$S$	Standard deviation of data set
$S_E$	Roughness pattern standard deviation
$St$	Stanton number
$t$	Plexiglas thickness
$T_\infty$	Freestream temperature
$T_{\text{FSn}}$	Freestream thermocouple reading at section n
$T_{\text{IR}}$	IR camera temperature reading
$T_{\text{Probe}}$	Thermocouple probe temperature
$T_s$	Surface temperature
$T_{\text{SS}}$	Subsurface calibrated thermocouple reading
$t_{\text{st}}$	Student t value
$T_{\text{TC,C}}$	General thermocouple reading during calibration
$T_{\text{TC,cal}}$	General calibrated thermocouple temperature
$T_{\text{TC,S}}$	General steady-state thermocouple reading
$T_{\text{UP}}$	Under the plate calibrated thermocouple reading

$u$	Fluid velocity
$U_{\infty}$	Freestream velocity
$U_{\text{fixed}}$	Fixed uncertainty associated with measurement
$U_{\text{rand}}$	Random uncertainty
$W_{\text{ha}}$	Width of heated area
<i>Greek</i>	
$\alpha$	Thermal diffusivity
$\delta$	Velocity boundary layer height
$\delta_T$	Thermal boundary layer height
$\varepsilon$	Emissivity (0.95)
$\zeta$	Unheated starting length
$\eta$	Freezing fraction
$\theta_f$	Nondimensionalized temperature
$\mu$	Fluid viscosity
$\rho_{\text{ice}}$	Ice density
$\sigma$	Stefan-Boltzmann constant (5.67E-08)
$\tau$	Ice accretion time
$\tau_w$	Wall thermal conductivity

*Acronyms*

IRT	Icing Research Tunnel
LWC	Liquid content
MVD	Median volumetric diameter
IR	Infrared

## ACKNOWLEDGMENTS

I offer my greatest thanks to Dr. Stephen McClain for not only serving as my advisor, but as my friend. His patience, insight, and encouragement were invaluable to this document. I would also like to thank Dr. Lesley Wright and Dr. Yang Li for serving as members of my thesis defense committee. The lessons you both have taught me have certainly shaped this document, and I am honored to have you on my committee.

I also owe much thanks to Logan Tecson. Logan started working on this grant in 2012, and I continued his work in 2013. I was very lucky to have a predecessor as intelligent, hardworking, and organized as Logan. The solid foundation Logan built has offered a smooth transition in continuing the efforts of this grant.

I would also like to thank Ashley Orr for his excellent craftsmanship, friendship, and the knowledge he has given me. I greatly appreciate the assistance and comedic relief of my fellow graduate students Timothy Shannon, Charlie Brown, Weston Harmon, Blake Heller, Ricardo Betancourt, Trae Liller, Jake Christoph, and Carl Reed.

I would like to thank my parents. Mom and Dad, thank you for your encouragement and sacrifice. I appreciate them more than I can express. Finally I thank my soon-to-be wife Lauren. The love and support you have given me was invaluable during this process.

This work was part of NASA Collaborative Agreement No. NNX12AB85A. I greatly appreciate the guidance of the members of the Icing Research Branch at NASA

Glenn Research Center. Any opinions presented in this document are those of the author and do not reflect the views of NASA or the United States government.

## DEDICATION

To my family and soon-to-be wife



## CHAPTER ONE

### Introduction

#### *Motivation*

It is well understood that aircraft wing icing adds weight, increases drag coefficients, decreases lift coefficients, and reduces stall margin. Ice accretion also results in a loss of aircraft control, which in turn causes accidents. Between the years of 1982 to 2000, the National Transportation Safety board reported 583 aviation accidents and 800 fatalities due to airframe icing [1].

There are two general categories of ice accretion control: ice accretion prevention, and de-icing. Ice accretion prevention techniques focus on preventing ice from building up on the wing through the use of devices such as electric heaters or pneumatic boots. De-icing techniques allow ice to accrete, and use chemicals to clean the wings in between landings and takeoffs. However, if ice is allowed to accrete, it becomes necessary to predict the reduction in performance the ice accretion will have on the aircraft. Given the shape of an ice structure, methods are available to predict the lift and drag on an accreted airfoil. But accurately predicting these shapes has proven to be difficult.

Several ice accretion prediction codes have been introduced in an effort to predict the shape of an accretion given icing cloud conditions. These codes step through time and solve an energy balance to predict where impinging droplets will freeze. The first energy balance was performed by Messinger [2], shown in Figure 1.1.

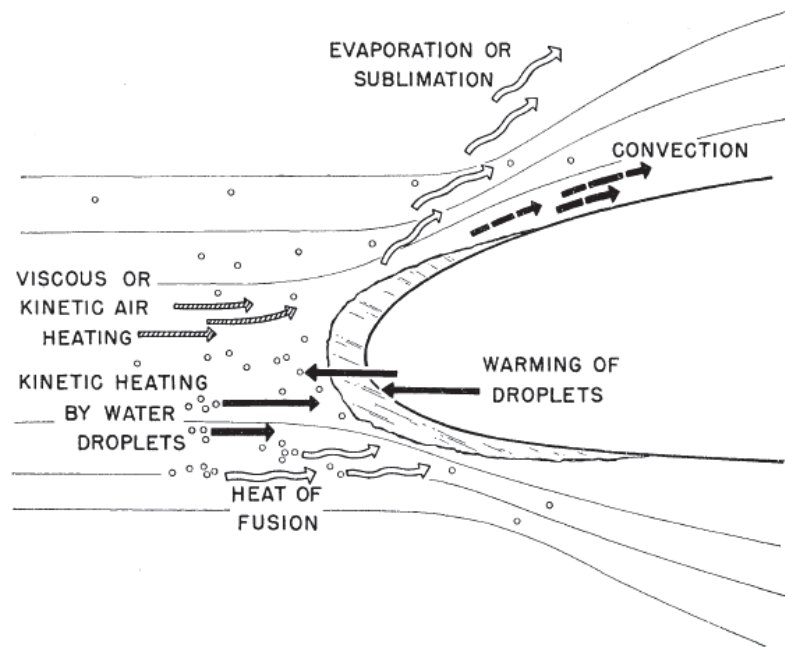


Figure 1.1: Energy balance on an unheated airfoil [2]

Many codes have been based on the Messinger model, including the NASA LEWICE code. Most of the terms in the Messinger model are well understood. However, once the initial ice roughness pattern is obtained the flow field becomes complicated, and there is no simple method to determine the convective heat transfer. It is preferred to use a semi-empirical approach and obtain convective heat transfer coefficients experimentally. Many ice accretion codes have used convection heat transfer coefficients based on the sand-grain roughness work done by Nikuradse and Schlichting [3-4]. It is now understood that the sand-grain roughness assumption yields a poor prediction of convection heat transfer coefficients, and a method for obtaining convective heat transfer data for realistic ice roughened surfaces is needed.

Tecson [5] evaluated the convective heat transfer for realistic ice roughness with constant heat flux boundary conditions. Because ice accretions are not constant thickness along an airfoil, the heat flux through these accretions is not constant. Convective heat

transfer enhancement is dependent on the heat flux boundary conditions, these effects must be studied in order to accurately predict the convective heat transfer coefficients used in ice accretion codes.

### *Objective*

This work aims to achieve the following three objectives: 1) measure convective heat transfer coefficients for realistic icing surfaces, 2) improve upon the quality of the measurements made in Tecson [5], and 3) determine the importance of thermal boundary conditions on heat transfer enhancement.

To accomplish objectives one and three, a test plate with the following four interchangeable roughness patterns was created: a test plate with smaller roughness elements and a smooth starting length (designated as 053096), a test plate with larger roughness elements (designated as 052996), a smooth test plate (designated as smooth-laminar), and finally a smooth test plate with a leading edge trip strip (designated smooth-turbulent). The smooth test plates served as a benchmark for experimental results. On each of these four patterns, two tests were performed to investigate the effects of ice roughness on heat transfer: a steady-state convective heat transfer coefficient test and a thermal boundary layer trace. Throughout the work, these experiments will be termed the roughness experiments.

To accomplish objective two, a test plate was created to test the transmissivity assumption made in Tecson [5]. An experiment was also performed to measure the thermal conductivity of the Plexiglas used in the heat transfer test plate. Throughout the work these will be referred to as the transmissivity and thermal conductivity experiments.

### *Presentation Outline*

Chapter two offers a technical background in heat transfer, fluid mechanics, and aircraft wing icing. Chapter two also contains a literature review in the field of aircraft wing icing. Chapter three contains a description of the materials used in the experiments, as well as the experiment methodology. Chapter four breaks down the data reduction equations and the uncertainty analysis used in each of the experiments. Chapter five contains a results and discussion section. Finally chapter six offers conclusions to be made about the results of these experiments.

## CHAPTER TWO

### Technical Background and Literature Review

#### *Heat Transfer and Fluid Mechanics*

##### *Boundary Layers*

This work includes measuring the shape of thermal boundary layers. Therefore, it is helpful to explain what a boundary layer is, and why it is important.

A velocity boundary layer, shown in Figure 2.1, is characterized by a deviation from the freestream velocity close to the wall. This occurs because of the presence of viscosity. As the molecules in the moving fluid interact with the motionless wall, the molecules in contact with the wall are slowed to essentially zero velocity. Other molecules in the fluid then interact with these slowed molecules, creating a velocity profile similar to that shown in Figure 2.1 for flow over a flat plate. The distance from the wall to the height where  $u(y)$  is approximately  $U_\infty$  is referred to as the boundary layer thickness,  $\delta$ . As shown in Figure 2.1,  $\delta$  is a function of the distance from the leading edge.

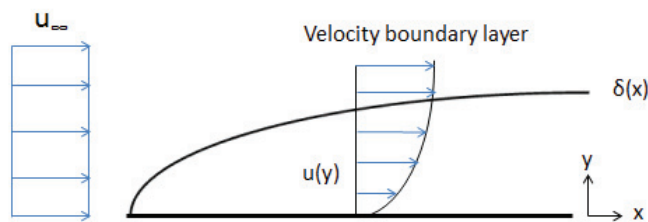


Figure 2.1: Flat-plate velocity boundary layer

The thermal boundary layer is similar to the velocity boundary layer in that it is characterized by a deviation from the freestream temperature near the wall. If the freestream temperature and the wall temperature are different, the freestream temperature will change as it interacts with the wall temperature as shown in Figure 2.2.

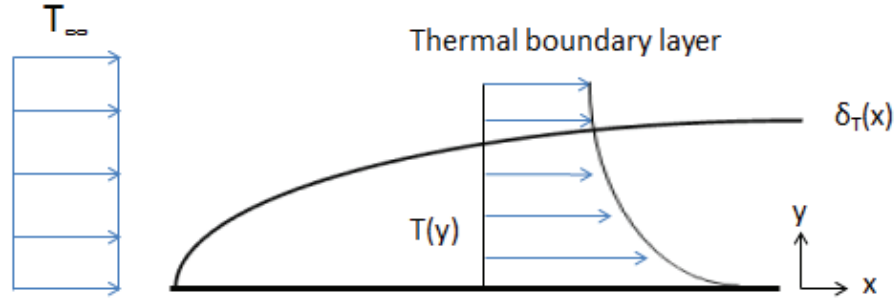


Figure 2.2: Thermal boundary layer

Both velocity and thermal boundary layers are important. Velocity boundary layers determine shear stress, as given by Eq. 2.1, where  $\mu$  is fluid viscosity.

$$\tau_w = \mu \frac{\partial u}{\partial y}_{y=0} \quad (2.1)$$

Shear stresses are important on an airfoil in icing conditions because they can affect how a water droplet moves along the surface of an airfoil, and as a result affect the roughness pattern. In a similar manner, the shape of a thermal boundary layer dictates convective heat transfer, as presented by Eq. 2.2, where  $k_f$  is the fluid thermal conductivity.

$$q''_w = -k_f \frac{\partial T}{\partial y}_{y=0} \quad (2.2)$$

Clearly this is very important to icing, as it dictates the convection term in the ice accretion energy balance.

Velocity and thermal boundary layers can be related through a nondimensional parameter called the Prandtl number. The Prandtl number can be defined as the ratio of kinematic viscosity to thermal diffusivity. Because the velocity boundary layer is well understood for a flat plate in both laminar and turbulent flow, the thermal boundary layer can be obtained by relating these boundary layers through the Prandtl number.

Furthermore, because convective heat transfer is dependent on the shape of the thermal boundary layer, a relation for the convective heat transfer coefficient can also be obtained through the Prandtl number. The relation for a flat plate in laminar flow is given by Eq. 2.3, and the relation for a flat plate in turbulent flow is given by Eq. 2.4.

$$h_{lam} = 0.453 Re^{\frac{1}{2}} Pr^{\frac{1}{3}} k_f x^{-1} \left( 1 - \left( \frac{\zeta}{x} \right)^{\frac{3}{4}} \right)^{-\frac{1}{3}} \quad (2.3)$$

$$h_{turb} = 0.0308 Re^{\frac{4}{5}} Pr^{\frac{1}{3}} k_f x^{-1} \left( 1 - \left( \frac{\zeta}{x} \right)^{\frac{9}{10}} \right)^{-\frac{1}{9}} \quad (2.4)$$

Note that  $\zeta$  is the unheated starting length, which is the length of the flat plate that the fluid encounters before a temperature difference is present. Eq. 2.3 and 2.4 will be vital in the development of the data reduction presented in chapter four.

If a flat plate exhibits a constant heat flux, the velocity and thermal boundary layers develop at proportional rates. When an unheated starting length present, this is not the case. Eq. 2.3 and 2.4 account for the fact that the velocity and thermal boundary layer are not developing at a proportional rate. Consider the unheated starting length proposed in McClain et al. [6], shown in Figure 2.3.

In Figure 2.3a, the velocity and thermal boundary layers begin to develop as soon as they interact with the plate, therefore they develop proportionally. In Figure 2.3b, the

velocity boundary layer begins to develop the same way it did as in case a. However, the thermal boundary layer does not begin to develop until the heated section, as shown in Figure 2.4, where  $\theta_f$  is the nondimensionalized thermal boundary layer. When a roughness pattern is present, the importance of the boundary conditions is magnified because of the interaction between the thermal boundary layer and the roughness element. For the unheated starting length boundary layer shown in Figure 2.4, the steep gradient allows for a quick change from the wall temperature to the freestream temperature. As a result, the roughness element is exposed to colder freestream temperature along its height than the isothermal boundary layer. Therefore heat transfer should be higher for the roughness element.

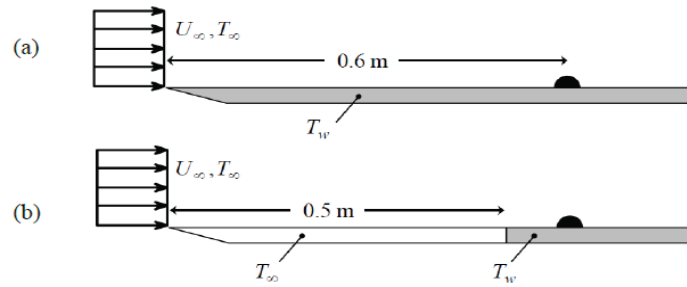


Figure 2.3: Flat plate in parallel flow for a) constant heat flux and b) unheated starting length [6]

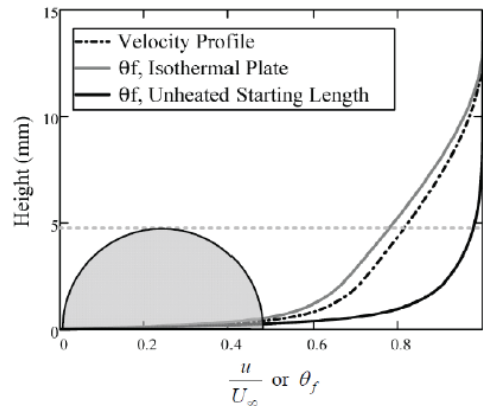


Figure 2.4: Viscous and thermal boundary layers for varying heat flux conditions [6]



## Roughness

The first investigations into the effect of surface roughness were performed by Nikuradse [3] and Schlichting [4], using sand-grain roughness elements along pipe walls and flat plates. They found that roughness increases fluid mixing, and as a result increases turbulence. Because of the increase in turbulence, heat transfer is also increased.

However, small sand-grain roughness elements behave differently than icing roughness elements, which are larger than the sand-grain roughness elements. Elements larger than an unperturbed boundary layer were investigated by Henry [7]. Figure 2.5 shows heat transfer enhancement versus the size of the element relative to the unperturbed boundary layer increases.

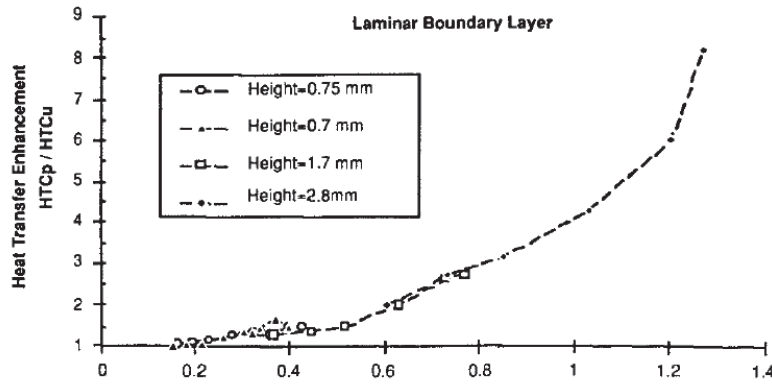


Figure 2.5: Enhancement relative to the unperturbed boundary layer [7]

As can be seen from Figure 2.5, enhancement increases as the element becomes larger than the unperturbed boundary layer, therefore studying roughness elements with accurate height to unperturbed boundary layer ratio is critical. Therefore, simple sand-grain roughness correlations cannot be used to approximate ice accretion results.

## *Aircraft Icing Background*

### *Icing Terms*

The following terms are commonly used in icing research. Understanding these definitions is vital to comprehending the icing literature.

Liquid water content (LWC):	LWC is the mass of water in a cloud per amount of dry air.
Freezing fraction:	The freezing fraction is a nondimensional ratio of impinging water droplets that freeze to total impinging water droplets.
Rime icing:	This is characterized by an ice buildup protruding directly into the flow, and occurs at low freestream temperatures.
Glaze icing:	This type of icing occurs at freestream temperatures just below freezing, and is characterized by an icing buildup outside of the stagnation region.
Horn Icing:	Horn icing is characterized by the presence of two horn shapes that project from both sides of an airfoil. This type of icing primarily occurs on unswept wings.
Scallops (Lobster Tails):	This type of icing is similar to horn icing but has gaps in it as it runs along the wing. This type of icing primarily occurs on swept wings.
Sweep Angle:	The angle a wing makes with a line perpendicular to the body of the aircraft.

### *Icing Process*

One of the first detailed attempts to observe the icing process was performed by Olsen and Walker [8], which used high speed cameras to film the icing process on an airfoil inside of NASA's icing research tunnel (IRT). They determined that as super-cooled water droplets impinge on an airfoil, they begin to coalesce with one another and

grow. Eventually droplets may grow enough that drag forces on the droplet begin to move in back along the airfoil. Droplets continue to move until they freeze. Eventually, there is an initial layer of roughness on the airfoil that dictates heat transfer. This initial roughness layer will look different for swept and unswept wings. It is important to note that although this was the general observations made, this process is not universal.

In glaze icing conditions, unswept wings, also referred to as the two-dimensional case because of the lack of cross flow along the airfoil, will typically exhibit a smooth zone and a rough zone as shown in Figure 2.6. The presence of these zones occurs because heat transfer is not high enough in the smooth zone to freeze the water droplets in this region, and they run to the rough zone.

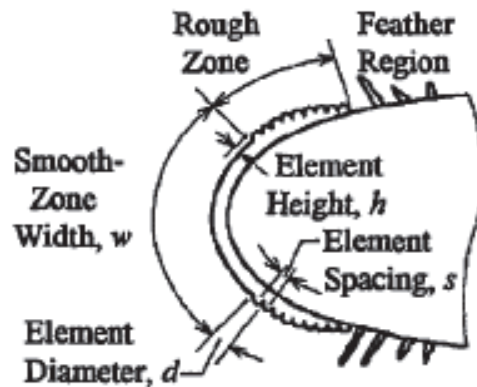


Figure 2.6: Ice accretion scheme for an unswept wing [9]

Swept wings, also referred to as the three-dimensional case, generally do not have a smooth zone. This is because the presence of cross flow increases heat transfer near the leading edge of the airfoil. Therefore droplets freeze before drag forces are strong enough to move them. The lack of a smooth zone is shown in Figure 2.7.

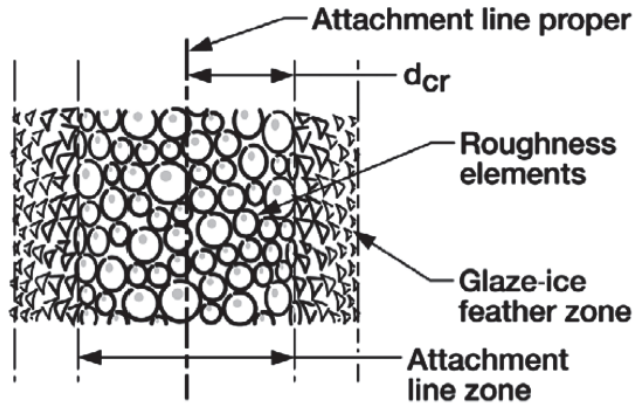


Figure 2.7: Ice accretion scheme for a swept wing [10]

After an initial roughness layer has been deposited, feathers will begin to form on the airfoil, as shown in Figure 2.8. Feathers are simply protrusions that develop into the flow because of water droplets continuing to freeze in that location. They typically grow in the marked locations in Figures 2.6-2.7. For unswept wings, these feathers will then grow into horns, shown in Figure 2.9. For swept wings, feathers will grow into scallops, shown in Figure 2.10. Swept wings exhibit scallops instead of horns because cross flow brings in water droplets at an angle. This leads to gaps in structure development. As one might expect, the shapes of scallops are much more difficult to predict than horn icing. Not only must heat transfer data be acquired, but a model for how scallops are initiated is needed.



Figure 2.8: Feathers developing on an airfoil [11]

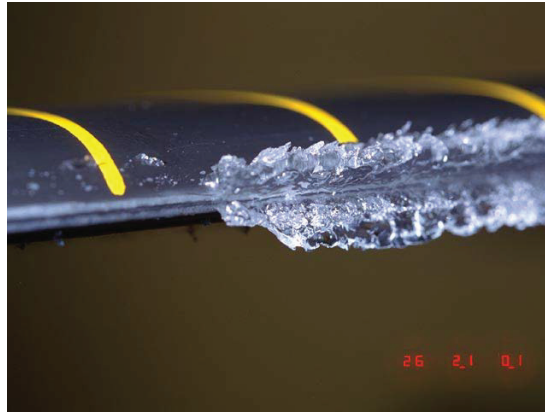


Figure 2.9: Horn icing on an airfoil [12]



Figure 2.10: Formation of scallops on an airfoil [11]

### *Literature Review*

#### *Early Icing Studies*

When aircraft icing was first encountered, the primary focus was on preventing it from accreting by chemical or physical means. In 1952 Lewis et al. [13] conducted a series of tests in NASA's icing research tunnel (IRT) to investigate the effectiveness of electric heaters in preventing icing buildup. The results indicated that a continuously heated parting strip at the airfoil leading edge was necessary for quick ice removal. The study determined the most energy efficient method was to use short intense energy bursts

to clear icing. If short bursts were used instead of continuous heating energy costs could be reduced by up to  $1/20^{\text{th}}$ . This method allowed for ice accretion, and prompted ice accretion studies.

Shortly after this, Messinger [2] performed one of the first studies to investigate the equilibrium temperature of an unheated airfoil at varying flight conditions in 1952. It was a purely theoretical investigation that developed relationships for heat flux losses at various equilibrium surface temperatures using energy balances. This study developed the “freezing fraction,” which is a ratio of water droplets that freeze to total impinging water droplets. Despite its age the “Messinger Model” and his freezing fraction are still used today in many ice accretion codes. Messinger’s energy balance can be solved to determine heat transfer between water droplets and the airfoil, and therefore determine when a droplet freezes.

In 1954 Von Glahn et al. [14] used the IRT to study the effect of icing on the drag coefficient of swept aircraft wings with the following varying parameters: air speed, angle of attack, and liquid water content (LWC). The results of the study concluded that glaze icing caused a significant increase in the sectional drag coefficient, while rime icing minimally increased the drag coefficient, for ice accretions of equal mass. Von Glahn et al. [14] witnessed that glaze icing was more severe as temperatures approached  $32^{\circ}\text{F}$ . Most importantly, they witnessed scallop formation, and were the first to offer a suggestion as to why it occurs. They hypothesized that high points were created in the icing formation that intercepted more impinging water droplets, and increased the size of the lobster tail. The studies’ research was significant because it shifted the focus away from rime icing, and started more investigation into glaze icing and scallop formation.

Over the next twenty years, research continued in the areas of ice prevention and early attempts to predict the shape of ice buildup were made. One of the more notable attempts was made by Wilder [15]. Ice structures were grown on an airfoil in the IRT at set icing conditions. The ice structure was then removed, and a plastic cast was created. The physical characteristics of the ice shape could then be measured. Wilder measured three lengths on the ice buildup: the stagnation thickness, which was the distance from the airfoil to the stagnation point, the upper surface thickness, which was the distance from the airfoil to the upper tip of the buildup, and finally the lower surface thickness, which was the distance from the airfoil to the lower tip of the buildup. Using these three measurements, Wilder was able to produce Figure 2.11. Note that the x axis is the theoretical ice thickness,  $I$ , which can be calculated based on icing conditions and known characteristics of the airfoil. Using the same IRT data used to generate Figure 2.11, Wilder was also able to generate Figure 2.12.

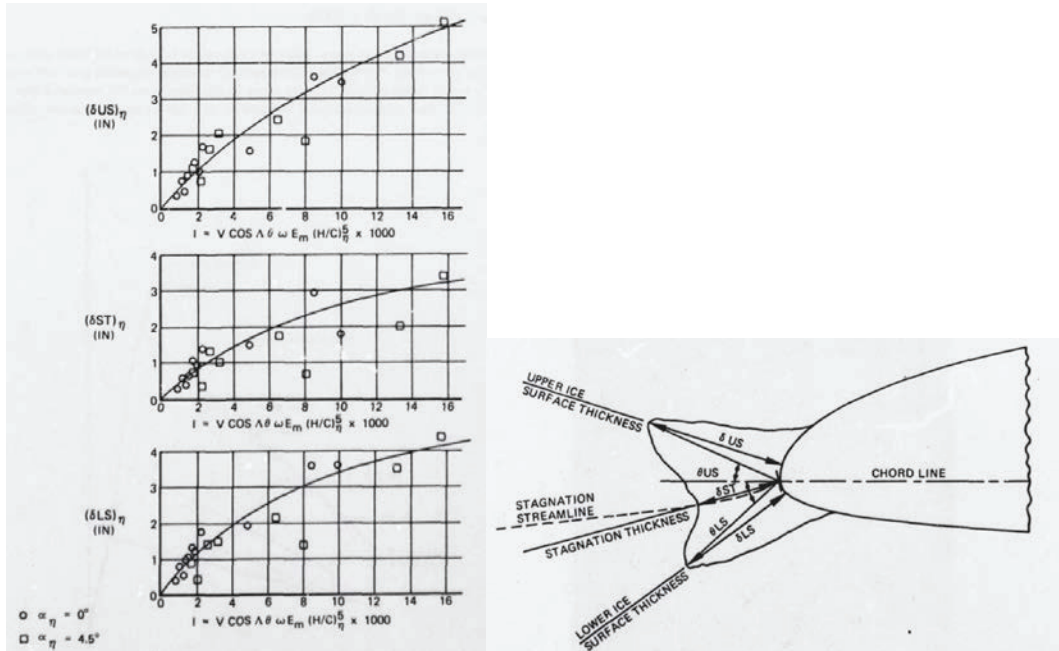


Figure 2.11: Wilder correlation agreement with experimental results [15]

Figure 2.11 shows how Wilder's correlation (the lines) agrees with data from the IRT with angles of attack of  $0^\circ$  and  $4.5^\circ$ . In general, the correlation appears to be more accurate for angles of attack of  $0^\circ$  rather than  $4.5^\circ$ . Figure 2.12 shows the type of icing that is likely to form at various airspeeds and temperatures (one set of icing parameters). Figure 2.12 can be a particularly useful tool, as glaze icing can be significantly more dangerous than rime icing.

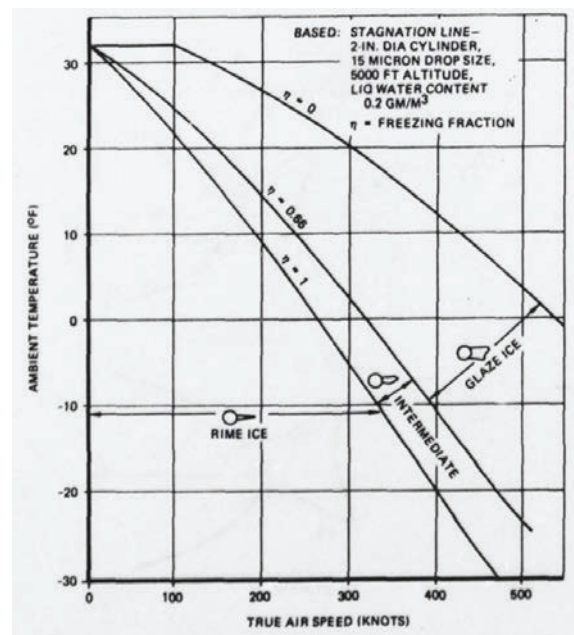


Figure 2.12: Different types of icing for common icing parameters [15]

Wilder's work was built upon through the 1980s and by the 1990s NASA's ice accretion prediction code, LEWICE, was accurate for specific two dimensional ice accretions cases, and extended it to three dimensions (swept wings). In 1992, to get "real world" icing data to test the LEWICE 3-D icing predictions, Reehorst [16] extended an airfoil from a DHC-6 DeHavilland Twin Otter aircraft. The icing conditions in the clouds were measured and recorded. After the icing structure was grown, the airfoil was brought



into the cabin to be studied. Reehorst found that LEWICE did not predict the scallop formation well. The code was tweaked in an effort to produce better agreement, but a scallop formation model was needed for better results.

In 1993, Hedde and Guffond [17] discovered that ONERA's Icing code, which is similar to LEWICE but developed in France, also had poor agreement with swept wings due to scallop formation. Therefore they attempted to model the scallops as a two phase process: an initiation phase, and a growth phase. In the initiation phase, water droplets are assumed to freeze on impact, and create behind them a zone where no droplets can freeze, as shown in Figure 2.13. This initial droplet soon catches others, and the growth phase begins. In the growth phase, the lobster tail (scallop) is split into two regions, as shown in Figure 2.14. The top of the lobster tail is assumed to be completely frozen because of the higher heat transfer. Any droplets that impinge on this area freeze in place. The bottom of the lobster tail is assumed to be a liquid film, and any droplets that impinge on this area add to the height of the lobster tail. After testing the updated code, it was successful in predicting the growth of the lobster tails, but the spacing between the tails was not as predicted. This work is important because it was the only model attempted for scallop growth until recent work.

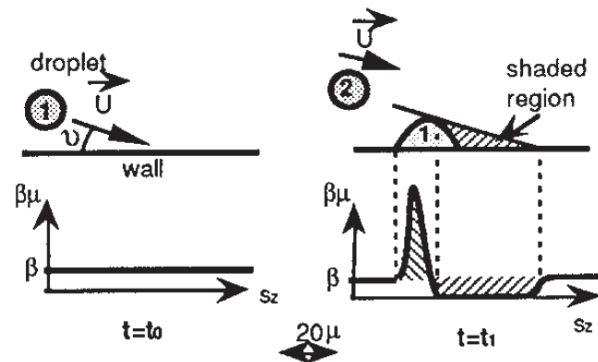


Figure 2.13: "Shadow effect" illustrated [17]

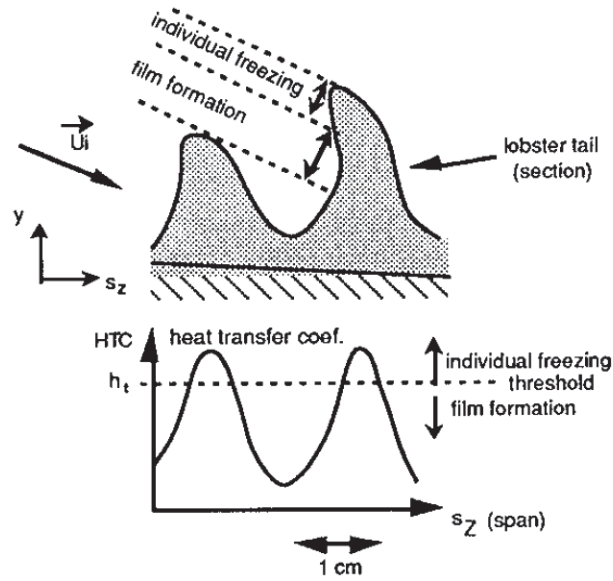


Figure 2.14: Regions of the “lobster tail” [17]

As previously mentioned, Olsen and Walker [8] used high speed cameras in the IRT to capture the icing process at varying icing parameters. In their work they discovered that water droplets coalesce on the surface of the airfoil and grow until drag forces overcome surface tension and sweep them along the airfoil, called water droplets shedding. These water droplets then freeze, and the ice accretion process begins. Because this discovery showed that water droplets do not freeze on impact, it proved Hedde and Guffond’s model to be unrealistic. Figure 2.15 shows how water droplet shedding affects the shape of the ice structure.

Viewing Figure 2.15 with the new idea of water droplet shedding, the shapes make sense in that the distance the water droplets shed is related to how quickly they freeze. Therefore in rime icing, formed at colder temperatures, the water droplets freeze almost immediately and shed very little. Near freezing temperatures, the beads shed back along the airfoil and then freeze.

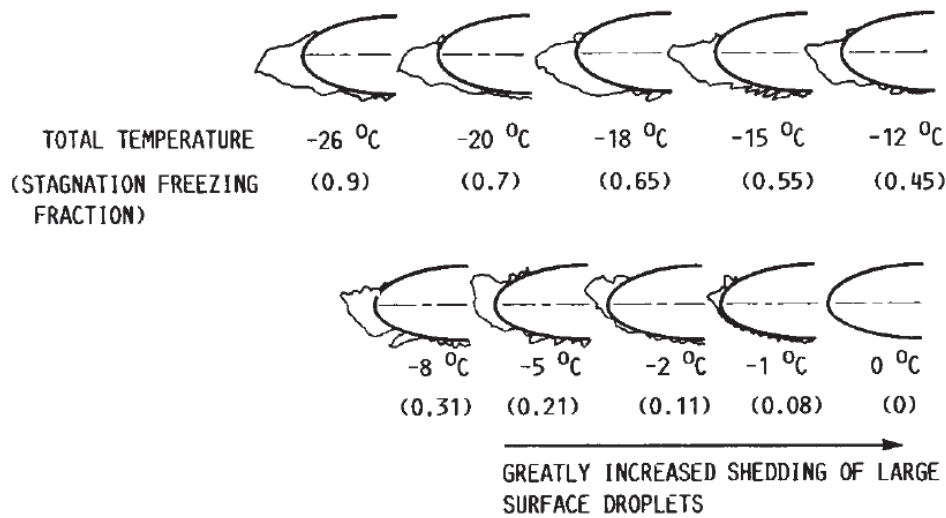


Figure 2.15: Ice formation at different temperatures [8]

### *Recent Icing Studies*

In 1998, Vargas and Reshotko [18] launched the first in depth investigation into what causes scallop formation. A NACA 0012 airfoil was placed in the IRT at sweep angles of 45°, 30°, and 15°. Video and photographic data were taken of the icing growth, and castings were made of the icing formation. They concluded that roughness elements from ice accretion develop into “feathers” that grow perpendicular to streamlines. These feathers then come together to form scallops. This is an important discovery in icing, because as they state “it ties scallop formation with local effects on 3D roughness elements.” Therefore when local effects are understood, scallop formation can then be better understood.

Vargas and Reshotko [19] continued their experiments, and in 2000 set out to determine how LWC and temperature affect the critical distance in ice accretion. The critical distance, as illustrated in Figure 2.16 ( $d_{cr}$ ), is the distance from the attachment line

to the spot where roughness elements begin to form feathers. Note that in Figure 2.16, it is drawn so that the reader is looking at the airfoil head on, hence the flow is impinging into the page.

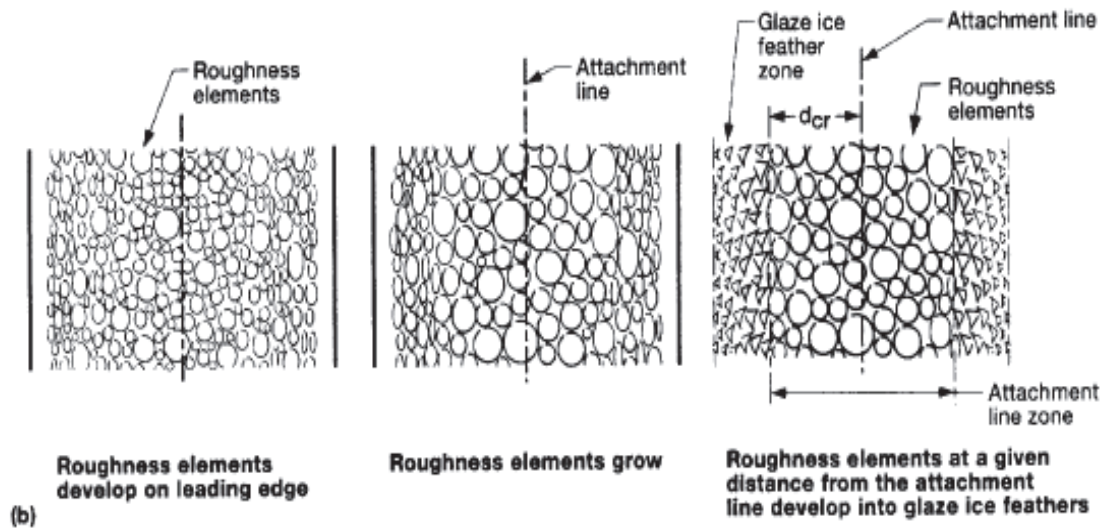


Figure 2.16: Illustration of critical distance [19]

The experiment was again conducted in the IRT. A benchmark case was chosen, and the LWC and free stream temperature were varied and compared to the benchmark case. This was done at sweep angles from  $0^\circ$  to  $45^\circ$  in increments of  $5^\circ$ . The results showed the following:

- As the LWC was decreased, the critical distance was decreased.
- As the LWC was decreased, full scallops developed at lower sweep angles.
- As the free-stream temperature is decreased, the critical distance was decreased.

Samples of the results for free-stream velocity of 150mph are shown in Figures 2.17 and 2.18. The results for other free-stream velocities are similar.

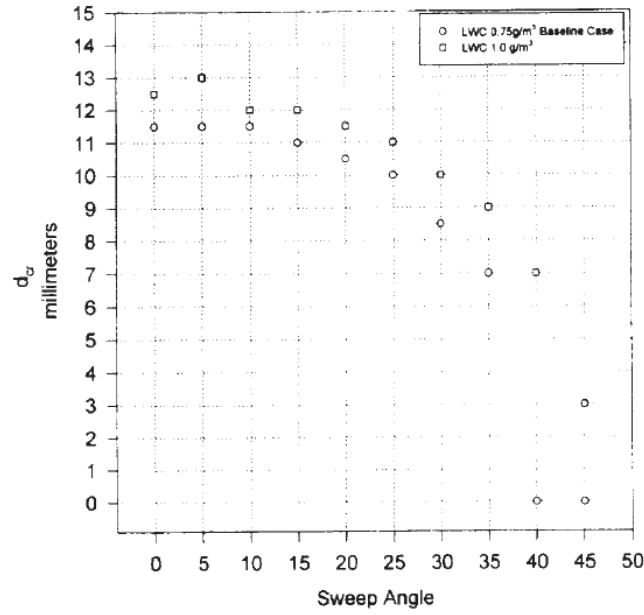


Figure 2.17: Critical distance at different sweep angles with varying LWC [19]

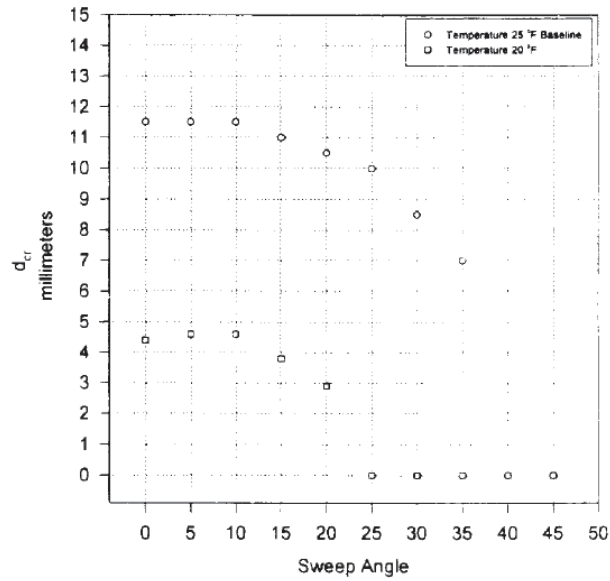


Figure 2.18: Critical distance at different sweep angles with varying temperature [19]

In a separate experiment Vargas and Reshotko [20] again varied the sweep angle of a NACA 0012 airfoil from 0° to 45° in increments of 5°, but the effort was focused on

investigating free-stream velocity on critical distance. The results are shown in Figure 2.19.

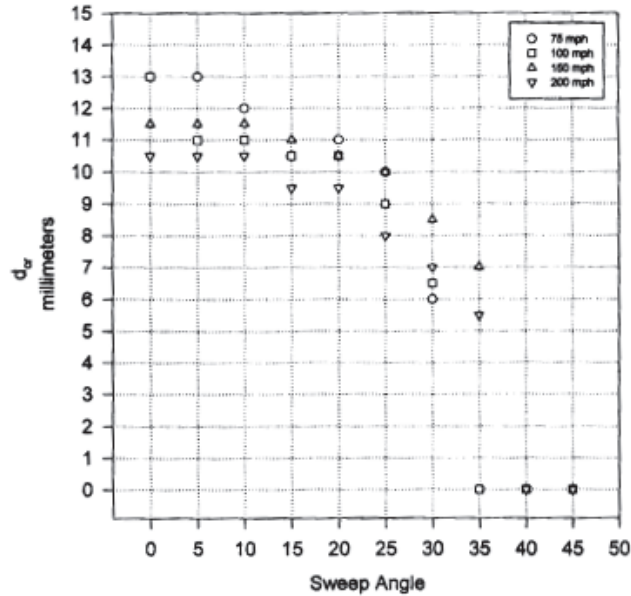


Figure 2.19: Effect of sweep angle on critical distance at various velocities [20]

As shown in Figure 2.19, as the sweep angle was increased to 25° the critical distance decreased. When the sweep angle was increased passed 25° the critical distance began to rapidly approach zero.

The presence of ice roughness zones that Vargas and Reshotko were witnessing was confirmed in Hansman et al. [21], which studied the effect of roughness on glaze ice. Ice structures were grown in 3 different testing facilities. Photographic data of this was acquired. Hannsman et al. determined that glaze icing could be broken up into zones: a smooth zone, a rough zone, and a zone where feathers grew.

Wright et al. [22] used the studies from Vargas and Reshotko to update the LEWICE software. The assumptions used in LEWICE 2.0 were reviewed, and some were invalidated. The most important assumption revisited was that all incoming water

droplets impinge on the surface. This assumption was determined to be incorrect, as water droplets actually splash when impacting the surface. As a result, some mass is lost and redistributed to other parts of the surface. An effort was made to better account for this fact in this study, and agreement of LEWICE predictions with experimental results was increased.

### *Icing Roughness Studies*

The following studies focus on the initial icing roughness, and how it affects ice accretion buildup. These studies have been important to the techniques used in this research, because they build on the roughness observations made in these experiments.

*Icing tunnel roughness studies.* Shin [23] performed one of the first studies to focus solely on the roughness formed by ice accretion. Shin varied icing parameters in the IRT. He concluded the following results:

- Roughness height increases with warmer temperatures and higher LWC values.
- Roughness height is related to the size of the boundary layer.
- Decreasing temperatures, increasing airspeed, and increasing LWC move the beginning of the rough zone closer to the stagnation region.

Anderson and Shin used the IRT to develop correlations for roughness-element diameter, and smooth-zone width based on the freezing fraction and accumulation parameter [9]. Roughness-element diameter is a parameter of particular importance because as later studies show heat transfer is determined by the size of the roughness element relative to the boundary layer. Figure 2.20 illustrates what the smooth-zone width is, and the results are given in Figures 2.21 and 2.22.

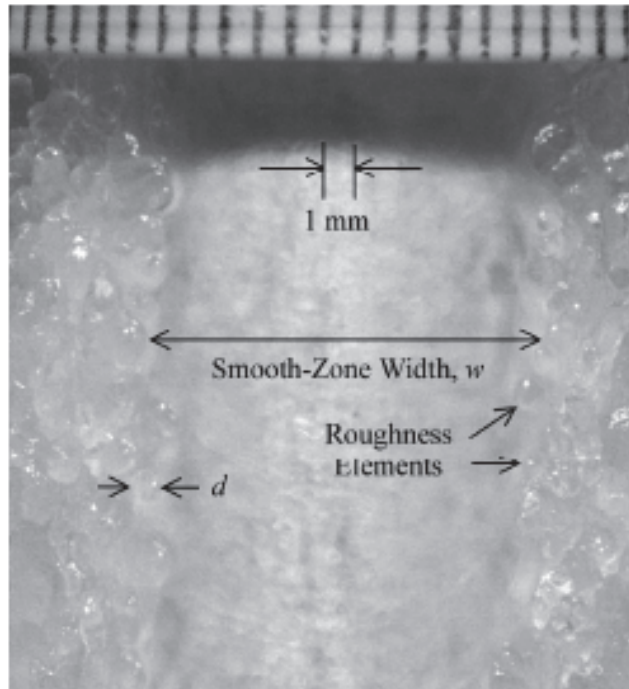


Figure 2.20: Smooth zone illustrated [9]

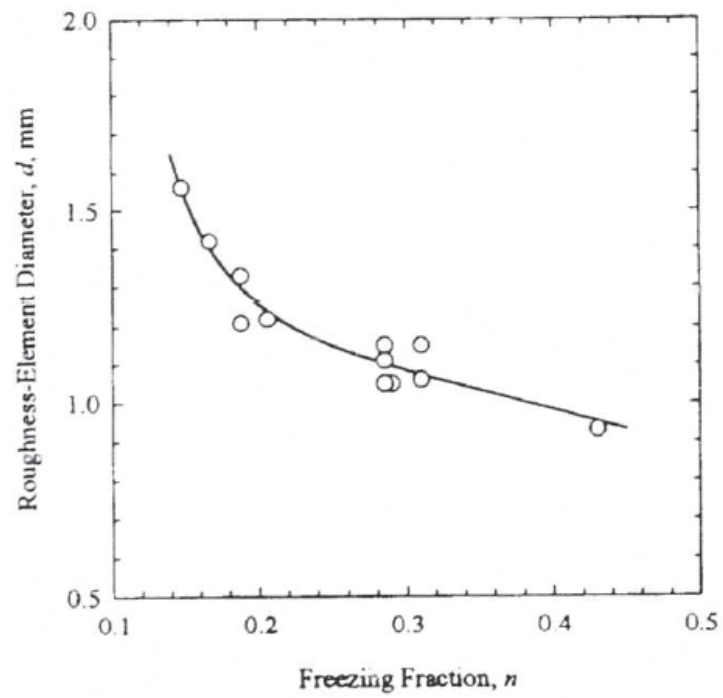


Figure 2.21: Roughness diameter vs. freezing fraction [9]



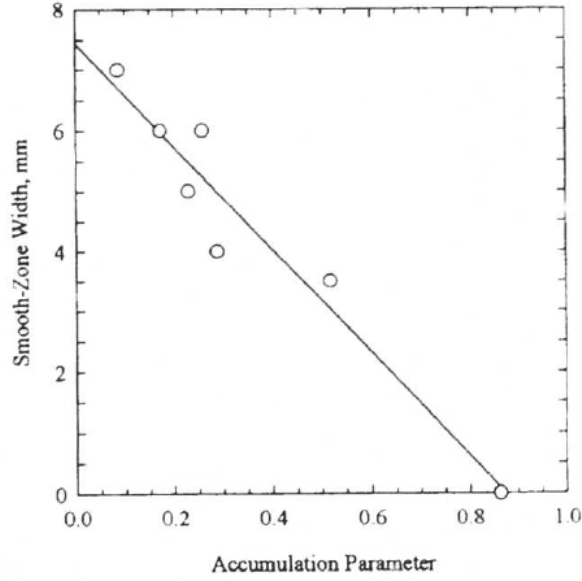


Figure 2.22: Smooth-zone width vs. accumulation parameter [9]

The accumulation parameter,  $A_c$ , is a nondimensional parameter that is proportional to the rate at which ice accretes. As Bragg et al. [24] defines it, “the accumulation parameter is a nondimensional mass flux and can be thought of as the length of ice growth in airfoil chords that would form on an imaginary flat plate placed perpendicular to the freestream flow for a time  $t$ .” A larger accumulation parameter indicates a larger rate of ice accretion and vice versa. The accumulation parameter is defined in Eq. 2.5, where  $V$  is the freestream velocity,  $LWC$  is the liquid water content,  $\tau$  is the accretion time,  $\rho_{ice}$  is the density of ice, and  $c$  is the chord length.

$$A_c = \frac{V(LWC)\tau}{\rho_{ice}c} \quad (2.5)$$

In a follow up experiment, Anderson [25] nondimensionalized the smooth-zone width and the element diameter using the leading edge airfoil radius, and then attempted to relate these nondimensional values to the accumulation parameter. To accomplish this, Anderson collected additional data from the IRT. The results are shown in Figure 2.23.

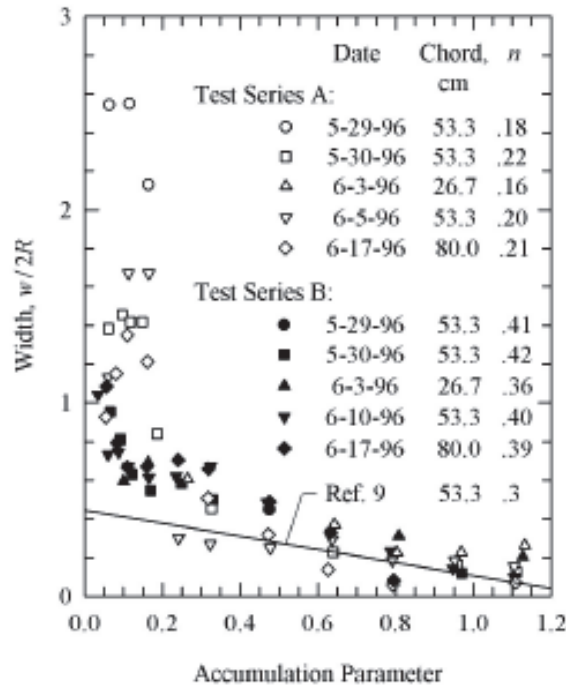


Figure 2.23: Accumulation parameter vs. nondimensional zone width [25]

As can be seen from Figure 2.23, the results match well with the correlation at higher accumulation parameters. Anderson concluded that element diameter was independent of the accumulation parameter. These relations provide promise in horn icing prediction. If these concepts can be related to the accumulation parameter, then it becomes easier to predict the roughness patterns for two-dimensional ice accretions.

After Anderson's experiments, it was noted that there was uncertainty in the process of roughness elements growing into horns. To investigate this, Tsao and Anderson [26] used high-speed imaging in the IRT to observe feather growth. They determined that feather angles were strongly dependent on stagnation freezing fraction. They further determined that the location and angle of feathers determine the location and angle of horn icing. They failed to determine the cause for large feather structures observed in some icing conditions.

To fill in some of the gaps in previous work, Vargas and Tsao [11] collected close-up photographic data on a NACA 0012 swept airfoil to study the growth of roughness elements into feathers in more detail. The data confirmed previous beliefs that roughness elements grow into feathers. More specifically, roughness elements freeze into pointed shapes (although a reason is not given). These pointed shapes join with other elements to form ridges. These ridges develop into feathers. A 2D drawing of this is shown in Figure 2.24. Although this experiment may seem qualitative, it is quite important to the development of ice accretion codes. As previously mentioned ice accretion codes step through time. Video studies, help code designers have an idea how to step through time. Although this research only focuses on heat transfer for initial icing roughness, these observations help researchers to understand the next steps to take.

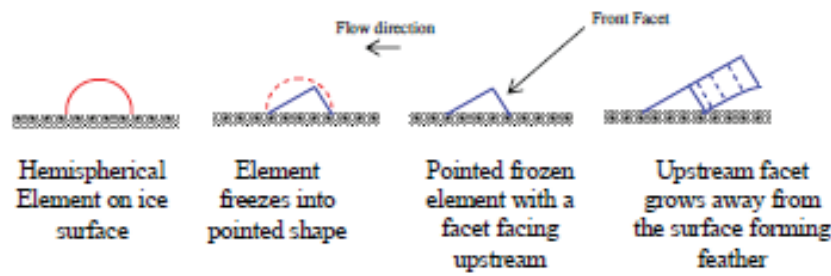


Figure 2.24: Roughness Element Growth [11]

*Heat transfer studies.* Van Fossen et al. [27] investigated the effect of surface roughness and free stream turbulence on heat transfer from icing structures grown in the IRT on a cylinder. After being grown in the IRT, the structures were cast, and could then be heated to obtain heat transfer measurements. They concluded that surface roughness causes the boundary layer to transition, increasing heat transfer. Heat transfer in the stagnation region was determined to increase as free stream turbulence increases.

Pais et al. [28] investigated heat transfer coefficients for horn icing (unswept wings). Horn-like icing structures were placed in a subsonic wind tunnel at the University of Kentucky. These structures were heated with foil heaters, and a steady-state method was used to acquire heat transfer data. Results, shown in Figure 2.25, indicated that heat transfer for a horn shape is different than heat transfer for a clean airfoil. Figure 2.25 compares Nusselt number values for an ice accreted airfoil (stars) versus a clean airfoil (asterisks). Note that the area of highest heat transfer is the upper horn, showing a 25% increase from the clean airfoil. This experiment is similar to the work being done in this research in the use of foil heaters to obtain heat transfer measurements. However, the efforts by Pais [28] obtain data for an ice accretion further in time, focusing on the end result of horn icing. Also, this is a little lacking, in that no roughness is present on the structure, as in the case of real ice accretion.

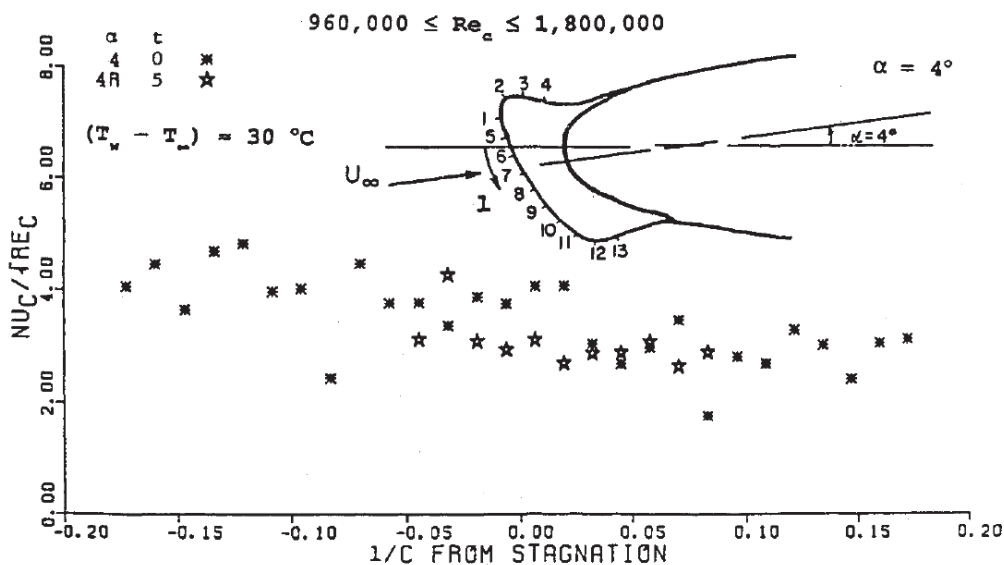


Figure 2.25: Nusselt number comparison for horn accretion vs. a clean airfoil [28]

Poinsatte et al. [29] attached systematic roughness elements to a NACA 0012 airfoil. A few different semispherical patterns were used; one is shown in Figure 2.26. Heat transfer coefficients for the roughness elements were obtained in both real flight tests and in the IRT. It was determined that the roughness elements increased heat transfer. As shown in Figure 2.27 the data obtained in the IRT and real flight tests were very similar. Note that “w/o air” and “w/ air” tests were the tests conducted in the IRT. Although not necessarily surprising, this study is important because it serves as a testament to the trustworthiness of IRT results. Note from Figure 2.27 that there is very little difference between the results obtained in real flight and the IRT.

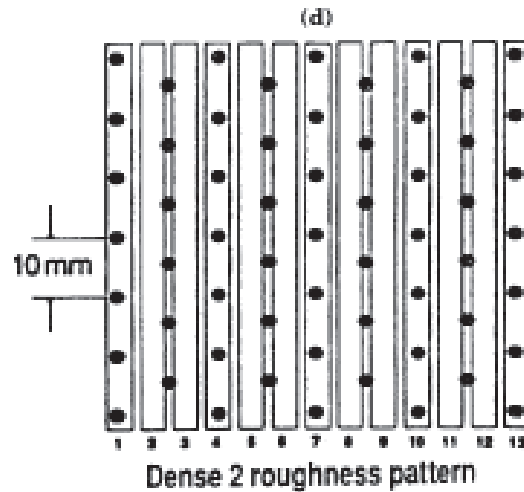


Figure 2.26: One systematic roughness pattern used in Poinsatte [29]

Like Poinsatte, Bragg et al. [30] investigated heat transfer using systematic roughness but focused on the smooth to rough zone. They placed systematic roughness elements, shown in Figure 2.28, along the NACA 0012 airfoil with a chord length of 21 inches, and then used IR lamps to heat the test area and an IR camera to record local heat transfer enhancement.

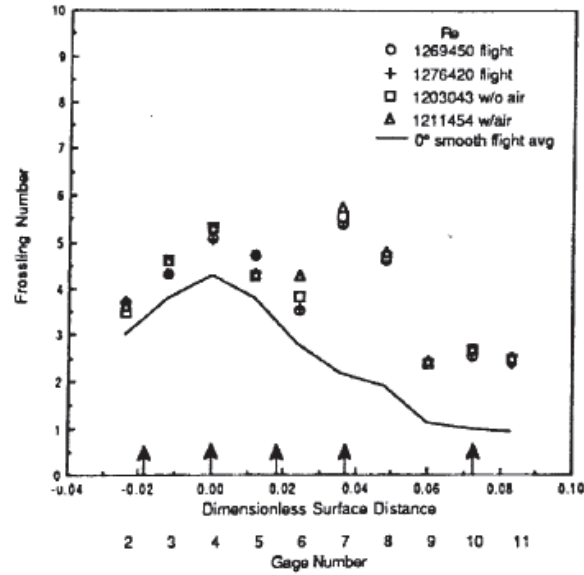


Figure 2.27: Frossling numbers along the surface for various flight tests [29]

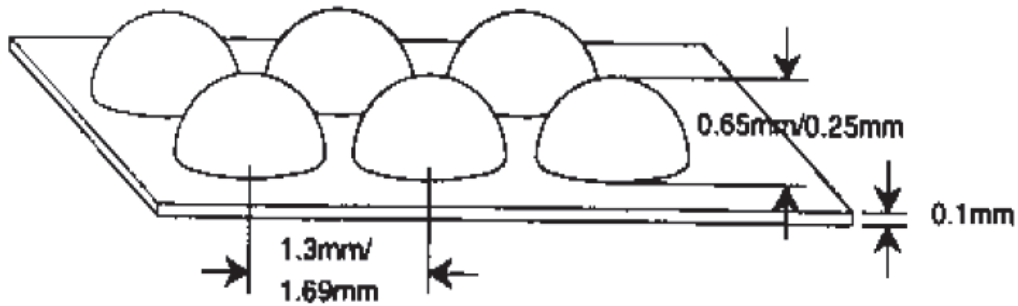


Figure 2.28: Systematic roughness elements used [30]

Heat-transfer effect of varying Reynolds number is shown in Figure 2.29, and the effect of varying turbulence intensity is shown in Figure 2.30. Note that this data was obtained by taking IR measurements along a single line. Figure 2.29 shows that heat transfer is higher at higher Reynolds numbers. There was no transition seen over the rough surface at these low turbulence intensities. Figure 2.30 shows that heat transfer values are similar for all turbulence intensities (the lines are the data in Figure 2.29).

However, at higher turbulence intensities there is a drop off in heat transfer enhancement (relative to a smooth NACA 0012). Bragg et al. contribute this to an earlier turbulence transition, not seen in Figure 2.29. The important takeaway from this study is that in the early studies of icing heat transfer studies, there was a focus on using systematic roughness to simulate icing roughness.

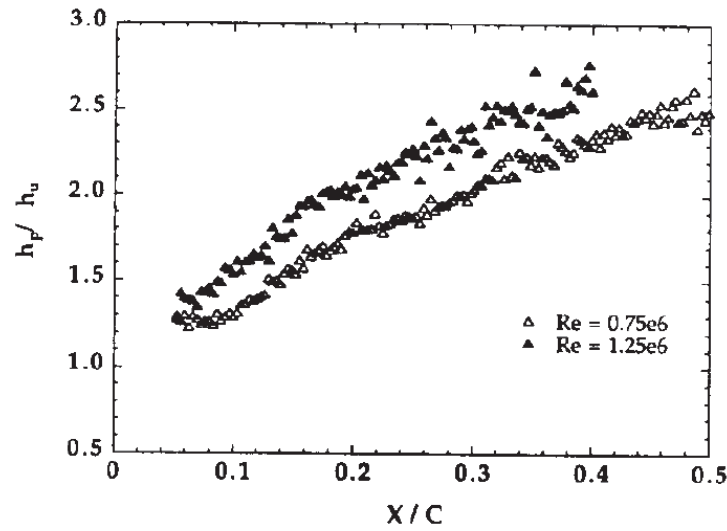


Figure 2.29: Enhancement with varying Reynolds number [30]

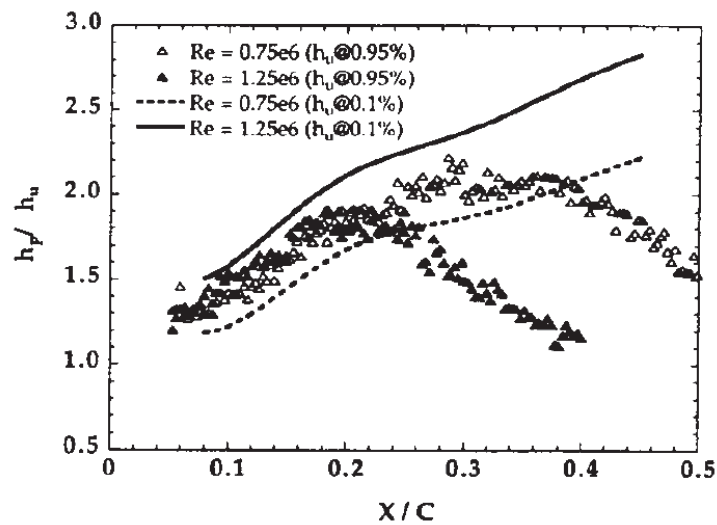


Figure 2.30: Enhancement with varying turbulence intensity [30]

In an effort to move away from Bragg et al. and Poinsatte's systematic roughness, Dukhan et al. [31] created casts, one of which is shown in Figure 2.31, of glaze ice roughness grown in the IRT. They then instrumented the casts with heating tiles, shown in Figure 2.32, to obtain heat transfer coefficients. The results, shown in Figure 2.33, indicate that the systematic roughness used in previous experiments underestimates heat transfer. Figure 2.33 compares the Frossling numbers from the casts to the Frossling numbers of Poinsatte's roughness patterns. Note that for the horizontal axis: negative numbers are on top of the airfoil cast, positive numbers are on bottom of the airfoil cast, and 0 corresponds to the stagnation region tile. The peaks correspond to the smooth to rough transition, and in these areas the real ice roughness Frossling numbers can be 110% higher than the systematic roughness patterns. This experiment demonstrated the importance of using realistic ice roughness to obtain heat transfer coefficients for icing prediction. It also showed that systematic roughness underestimates heat transfer in the smooth to rough transition, where the horns are expected to eventually grow.

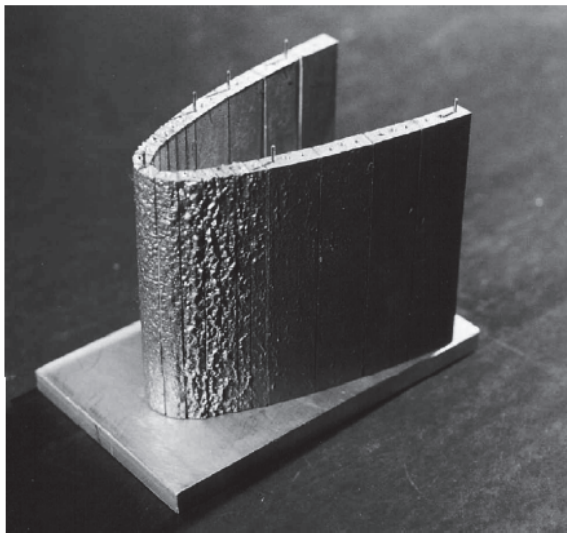


Figure 2.31: Mildly rough glaze ice cast [31]



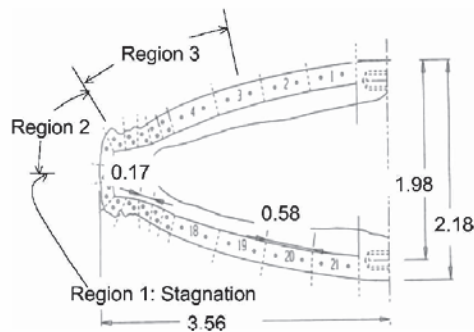


Figure 2.32: Test setup [31]

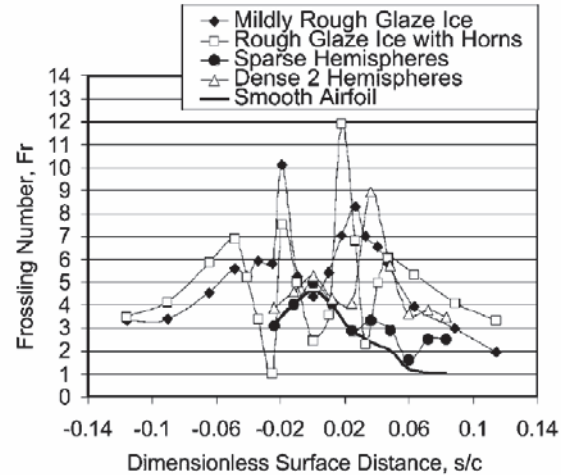


Figure 2.33: Frossling numbers of the surface [31]

Instead of focusing on the roughness pattern as a whole, Henry et al. tested the effect of single surface irregularities on local convective heat transfer [7]. Roughness elements of varying sizes were placed on a flat plate. The plate was heated with IR heat lamps, and the temperature profile was gathered using an IR camera. The experimental setup is shown in Figures 2.34 and 2.35. Local convective heat transfer coefficients could then be calculated using the energy balance shown in Figure 2.36. Two key results of Henry's work are presented in Figures 2.37 and 2.38

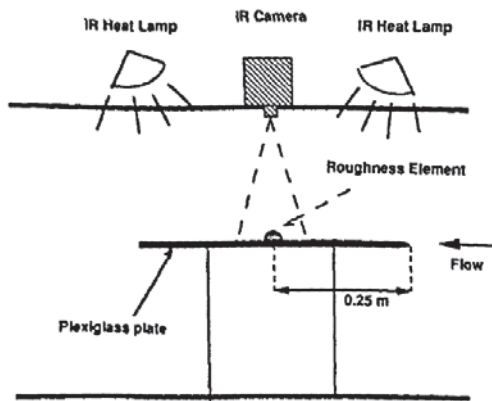


Figure 2.34: Test setup [7]

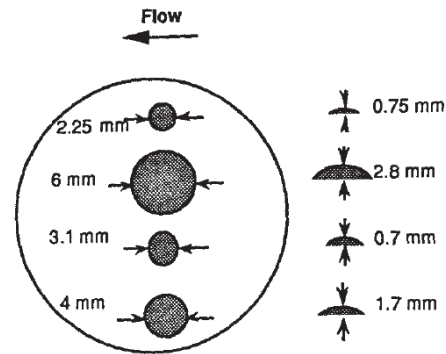


Figure 2.35: Roughness elements used [7]

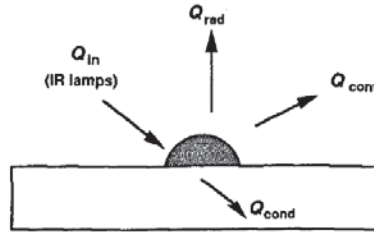


Figure 2.36: Energy balance used [7]

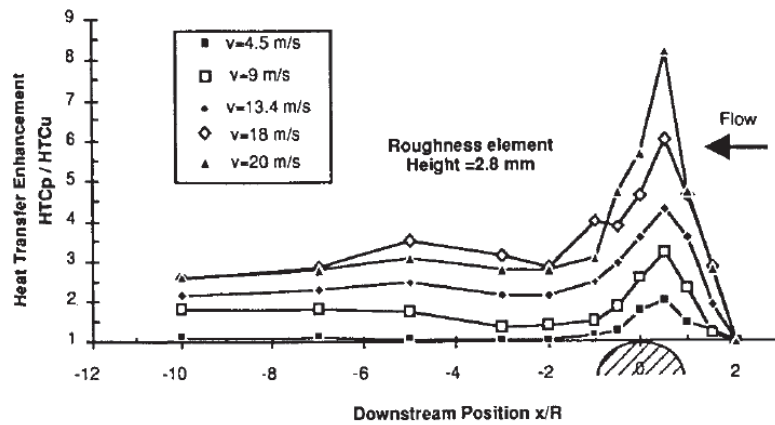


Figure 2.37: Enhancement over a single element [7]

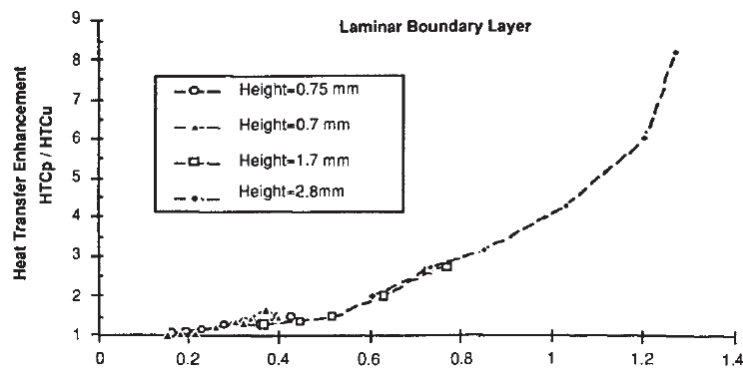


Figure 2.38: Enhancement relative to the unperturbed boundary layer [7]

Figure 2.37 shows the heat transfer enhancement relative to a smooth surface for a single roughness element. Note that the highest heat transfer enhancement is just upstream of the center point. Henry notes this as the probable reason for feathers growing

into the streamlines. Figure 2.38 shows the effects of roughness element size relative to boundary layer size. For roughness elements smaller than the unperturbed boundary layer, as roughness element size increases, heat transfer enhancement increases linearly. Once the roughness element is larger than the boundary layer, heat transfer enhancement increases exponentially.

Although, Henry captured some important general trends, McClain et al. [32] showed that the results were not properly interpreted because the thermal conductivity effects in the roughness elements were not accounted for in the energy balance. For roughness elements with low thermal conductivity, as in Henry [9], the temperature differences must be accounted for. McClain et al. [32] created an extended surface discrete element model (ES-DEM), which essentially treats the roughness elements as fins. The results of this model compared to Henry [9] are shown in Figure 2.39. This figure shows that Henry [9] underestimates the apparent enhancement.

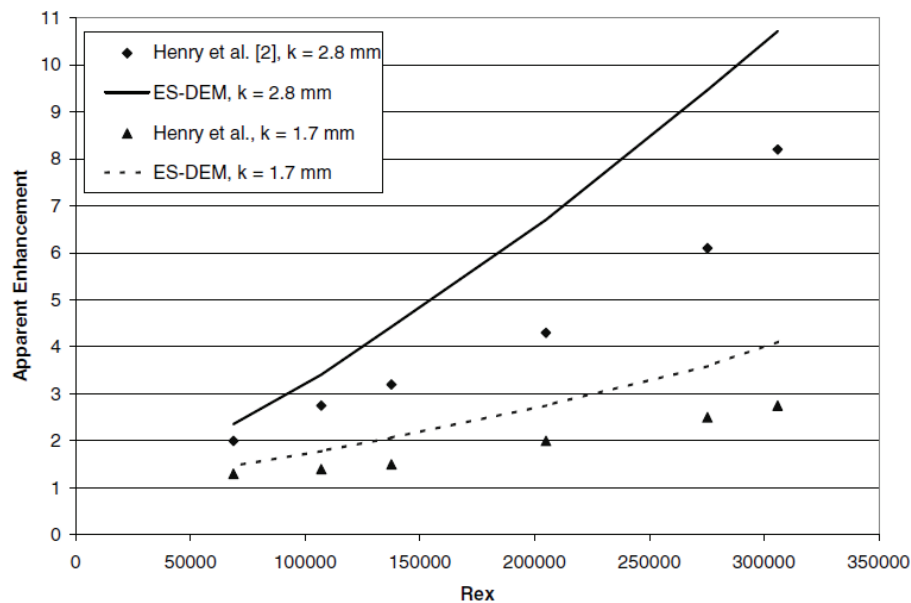


Figure 2.39: ES-DEM model compared to Henry [32]

In another study Henry et al. [33] obtained heat transfer coefficients for ice accretion inside of an icing tunnel. The surface of the airfoil was heated by laser source, and an IR camera was used to obtain temperature profiles. They concluded that the largest enhancement in glaze icing is where the horns begin to grow, which is consistent with previously mentioned studies. Their results for a rime ice case and a glaze ice case are shown in Figures 2.40 and 2.41. These figures show that for rime icing conditions, the convective heat transfer coefficients are fairly constant. However, for glaze icing conditions, the convective heat transfer coefficients vary more, and as a result are more difficult to predict.

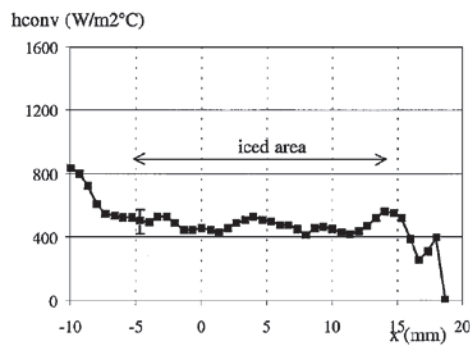


Figure 2.40: Rime icing heat transfer coefficients [33]

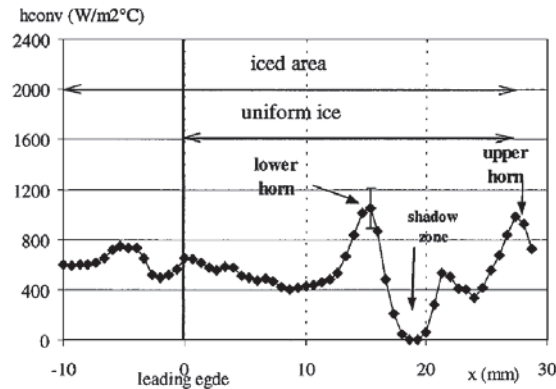


Figure 2.41: Glaze icing heat transfer coefficients [33]

Tecson et al. [34] developed a method to create realistic ice roughness that can be mapped to a flat plate. This flat plate can then be used to obtain heat transfer data. A code was developed that randomly places droplets, and then joins touching droplets to represent coalescence. The results are then modified to represent icing data captured from Anderson's studies. These results can be rapid prototyped to produce the roughness shown in Figure 2.42.



Figure 2.42: Rapid prototyped realistic roughness model [34]

Using the rapid prototyped model shown in Figure 2.41, Tecson [5] acquired heat transfer data for realistic ice roughness elements. A steady-state, constant heat flux method was used to obtain the heat transfer coefficients ( $\text{W}/\text{m}^2\text{K}$ ) shown in Figure 2.42.

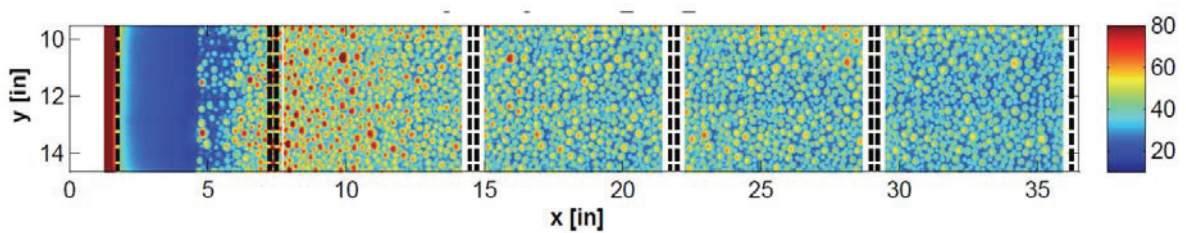


Figure 2.43: Convective heat transfer coefficient contour map for realistic ice roughness [5]

Traditionally, approaches to obtaining convective heat transfer for ice accretions could be broken up into two categories: using systematic roughness patterns, or creating molds of real ice accretions. Tecson's work is important because it seeks to bridge the gap between these two categories, by manufacturing real ice roughness. This work seeks to expand on Tecson by determining the effect of variable thermal boundary conditions on the roughness patterns used in Tecson [34].

### *Summary of Literature Review*

A review of work done in the field of aircraft icing over the past century has been provided. Messinger began the first energy balance, and his work was built upon to create ice accretion codes. These accretion codes were built upon by using icing tunnels to investigate how ice accretes, what initial ice roughness patterns look like, and how these initial roughness patterns effect future ice growth. Many studies have investigated convective heat transfer for these icing studies. One of the more recent studies, Tecson [5], involves mapping realistic ice roughness to a flat plate, and then using IR imaging to acquire detailed convective maps. Results were only obtained for constant heat flux cases. Because airfoil ice accretion is not uniformly thick, the heat flux boundary conditions vary. The purpose of this research is to expand upon the work done by Tecson [5] by investigating the effect of variable heat flux conditions on convective heat transfer.

There is still much research to be done in this field. Very little investigation has been done into three-dimensional ice accretion. This is because these shapes are complicated, and this adds complexity to experimental techniques. Because the method presented in this research can be applied to any shape despite its complexity, it is possible to later apply this same technique to swept airfoil ice accretions.

## CHAPTER THREE

### Materials and Methodology

To further understand convective heat transfer for ice roughness, three experiments were performed: roughness experiments, a transmissivity experiment, and a thermal conductivity experiment. The roughness experiments focus on obtaining heat transfer data for variable heat flux boundary conditions. The transmissivity experiment focuses on testing the transmissivity assumption used in Tecson [5]. The thermal conductivity experiment focuses on improving upon the thermal conductivity value used in Tecson [5]. This chapter provides a summary of the equipment and materials used, and the experimental procedure performed in this research. This chapter is broken into the following three sections: 1) materials and methodology of the roughness experiments, 2) materials and methodology of the camera transmissivity experiment and 3) materials and methodology of the thermal conductivity experiment.

#### *Roughness Experiments*

##### *Materials*

The roughness experiments section encompasses two experiments: the steady-state heat transfer tests used to obtain convective heat transfer coefficients, and the thermal boundary layer traces. This section describes the materials used in these two experiments. Figure 3.1a shows the experimental setup for a steady-state heat transfer test. Figure 3.1b shows a similar diagram for the thermal boundary layer traces. There is

only one difference between the two: Figure 3.1a has an IR camera on a one-dimensional traverse, while Figure 3.1b has a temperature probe on a two-dimensional traverse. Each component in Figure 3.1 is described in further detail later in this chapter.

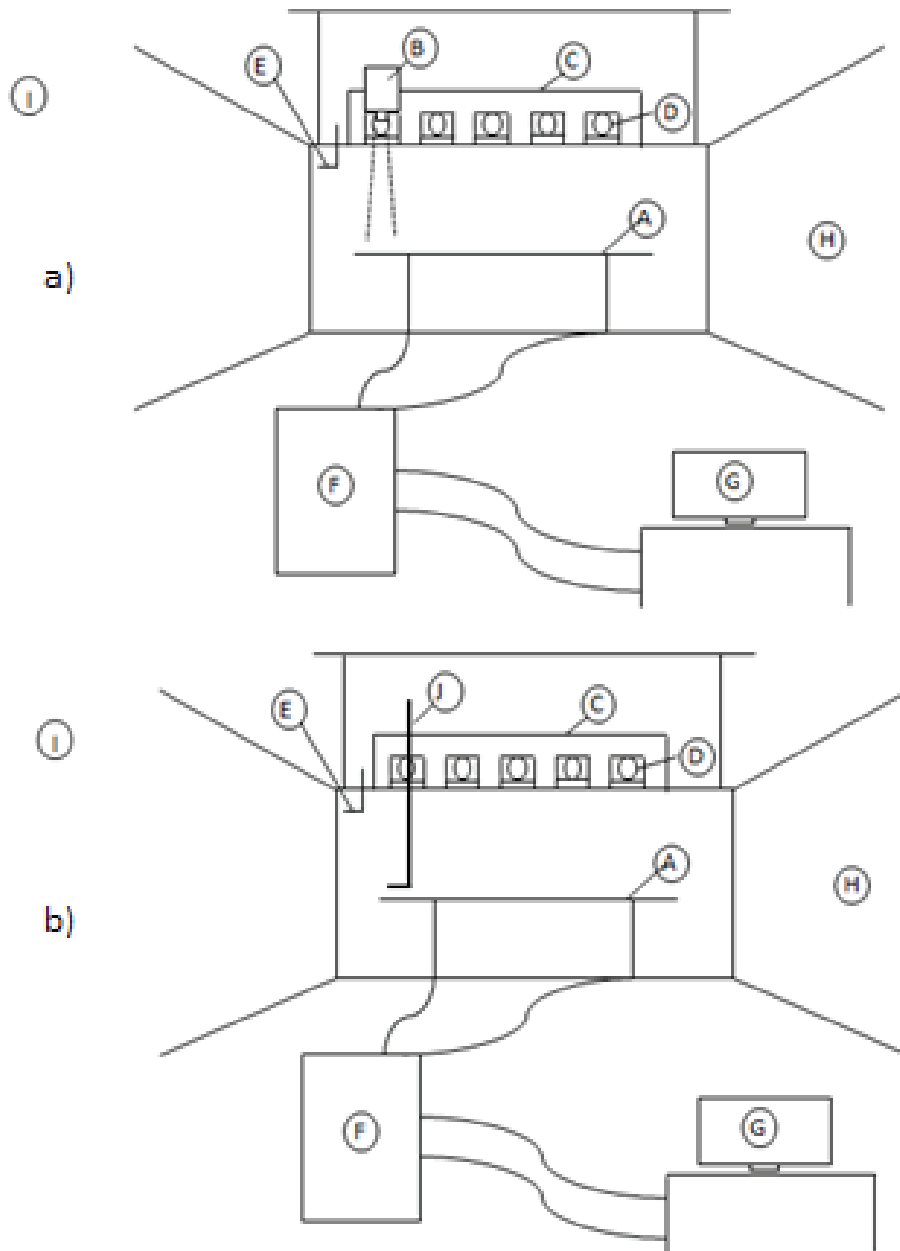


Figure 3.1: a) Test setup for a) heat transfer tests and b) thermal boundary layer traces



The following is a list of components:

- A) Roughness test plate
- B) Infrared (IR) camera
- C) Traversing system
- D) IR window system
- E) Pitot-static probe
- F) Cart of measurement devices and power sources
- G) Labview monitoring
- H) Baylor subsonic wind tunnel
- I) Z-series inlet measurements
- J) Velocity or Temperature Probe

*Roughness test plate.* Note that all work on the creation of the roughness test plate and the creation of the roughness panels was performed by Tecson [5]. Enough information will be provided for a basic level of understanding on how the roughness test plate and its roughness panels were created, but if additional information is required, refer to Tecson [5]. The general setup of the roughness test plate is shown in Figure 3.2. Figure 3.3 shows the side view of the test plate. Figure 3.4 shows the underlying heater with a roughness panel removed.

The general design of the roughness test plate is as follows. The test plate has 25 removable panels. These panels can be interchanged with four different roughness patterns: a smooth set of panels, a smooth set of panels with a leading edge trip strip, a large roughness (052996), and a small roughness with a smooth starting length (053096). The center row of five panels can be heated using Mylar film heaters with known voltage

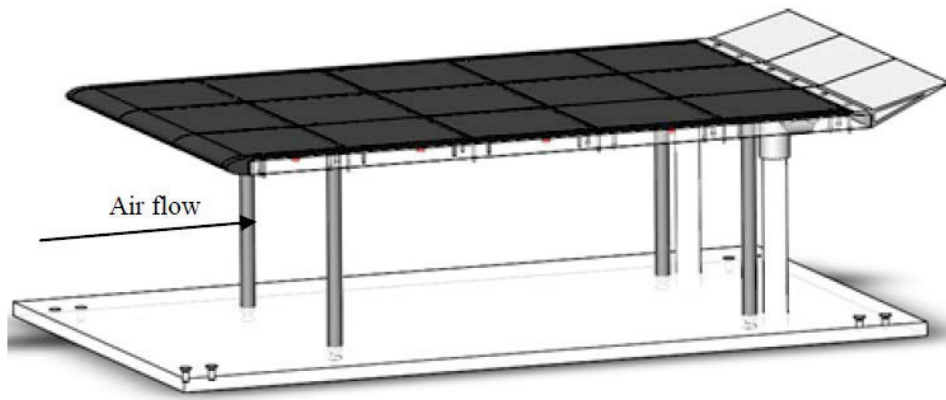


Figure 3.2: Roughness test plate [5]

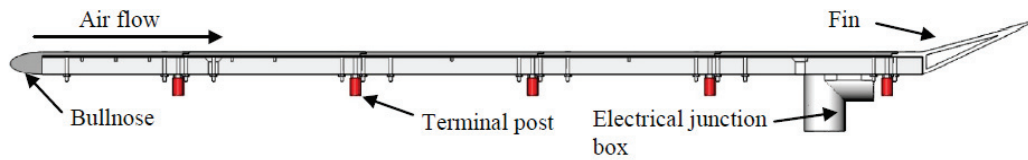


Figure 3.3: Roughness test plate side view [5]

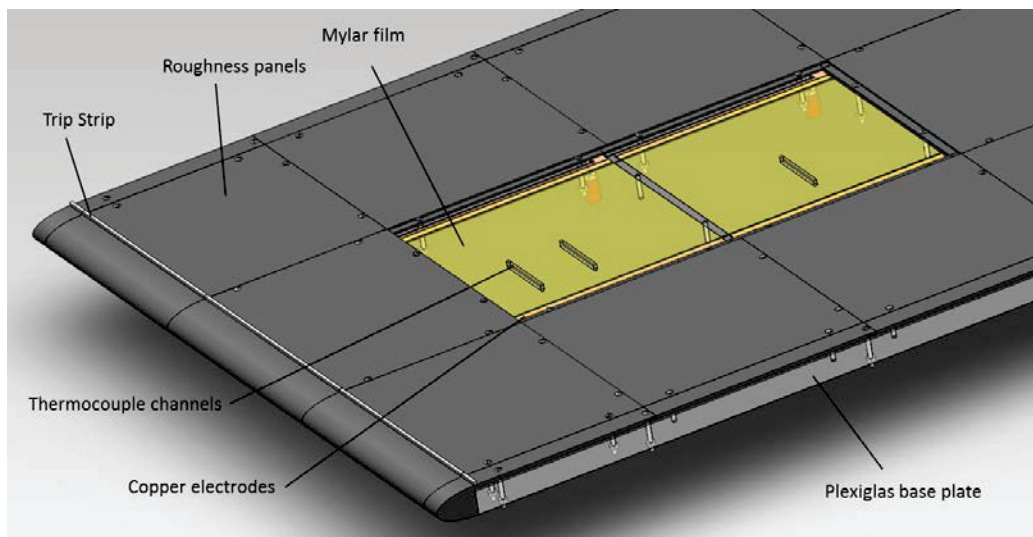


Figure 3.4: Roughness panels removed

and current. The temperatures at the top and bottom of the Plexiglas base plate are recorded using sixteen thermocouple pairs along the test plate to obtain a heat flux

through the Plexiglas. Heat transfer measurements can then be made on the top of the roughness panels using an IR camera. A set of five subsystems of the roughness test plate will be discussed in further detail:

- 1) Test plate structure
- 2) Wiring and thermocouples
- 3) Mylar film
- 4) Tail
- 5) Roughness panels

Test plate structure. The bare structure of the test plate is shown in Figure 3.5. A router with a 1/2 inch diameter straight bit was used to machine the electrode channels shown below to a depth of 0.035 inches. This allowed copper electrodes shown in Figure 3.5 to sit flush with the top of the Plexiglas base plate. A 1/8 inch diameter straight bit was used to machine the thermocouple channels to a depth of 1/8 inch. The end of the channel away from center was drilled all the way through the bottom of the Plexiglas base plate to serve as a wiring escape hole. The steel leg supports were attached with four 3/8'' 1.5'' long countersunk bolts. The roughness panels were attached with #4 1.25'' long bolts, and secured with #4 nuts.

Wiring and thermocouples. All wiring for sensing and power was routed through schedule 40 PVC piping (electrical junction box), previously shown in Figure 3.2 and Figure 3.3. Eight K type thermocouples were placed in the previously mentioned thermocouples channels (the channels are visible in Figure 3.5). These thermocouples, designated as  $T_{ss}$ , were placed so that the bead was in the center of the test plate, and the

wires were run through the wiring escape hole. An additional eight K type thermocouples were placed directly below the thermocouple channels on the bottom of the Plexiglas base plate. These thermocouples are designated as  $T_{UP}$ . Together the  $T_{SS}$  and  $T_{UP}$  thermocouples allow the heat flux through the Plexiglas to be calculated. The locations of these thermocouples, and the naming scheme used to identify them is shown in Figure 3.6. Finally, another type k thermocouple was attached to the pitot-static probe to measure freestream temperature.



Figure 3.5: Test plate structure [5]

Fourteen gauge wiring was run to each of the five sets of terminal posts to power the heaters. The fourteen gauge wire was fed through current transducers that use the Hall Effect to measure current. Twenty-two gauge wiring was also run to each of the five sets of terminal posts to a DAQ module to measure voltages across the heaters. Note that due to equipment limitations the voltage and current for the fourth section is not monitored with a DAQ module, but rather with two Newport TrueRMS HHM290/N Supermeters. For clarification, a wiring diagram for a single test panel is given in Figure 3.7.

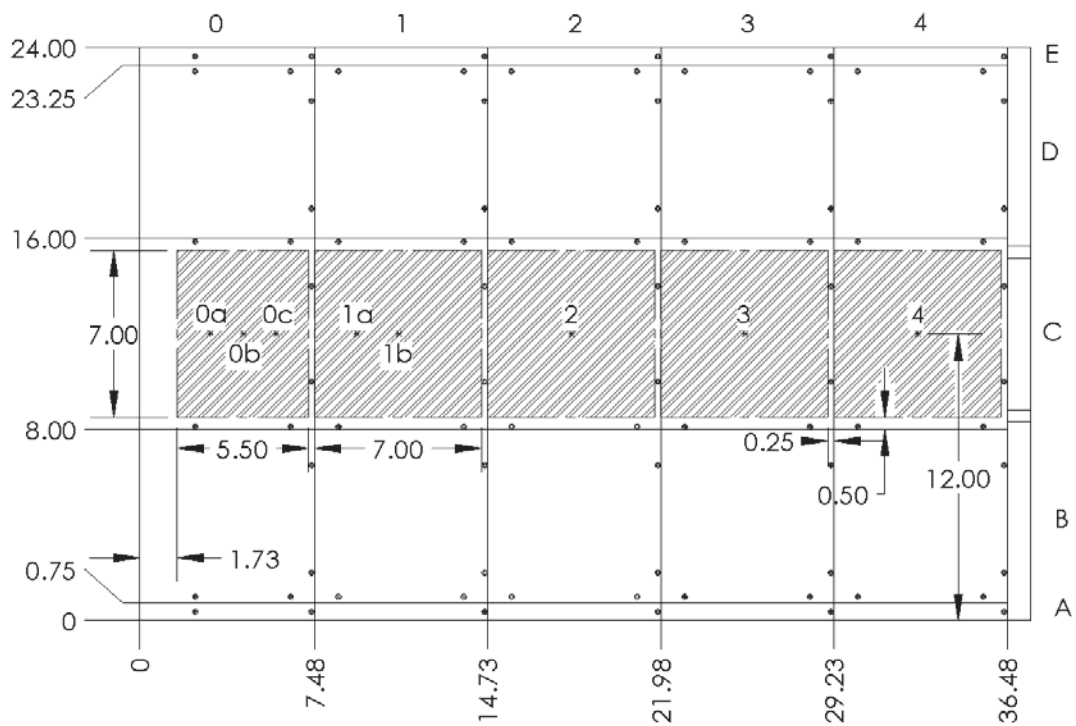
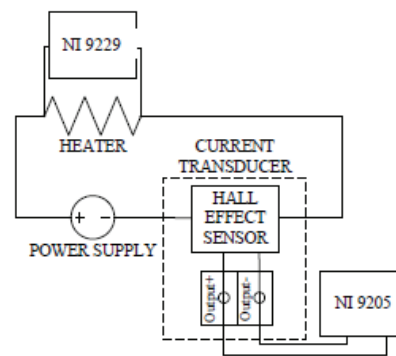
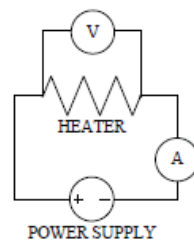


Figure 3.6: Thermocouple and Mylar film locations, dimensions in inches [5]



(a) Sections 0-3



(b) Section 4

Figure 3.7: Roughness test plate wiring diagrams [5]

Mylar film. The gold Mylar film serves as a heater in the apparatus. It was stretched between two copper electrodes, and attached using silver conductive paint, as shown in Figure 3.8. Because the Mylar heaters could not be in contact, small joints were present between the heaters. The size of these joints and the location and size of each heater is shown in the shaded regions of Figure 3.6.

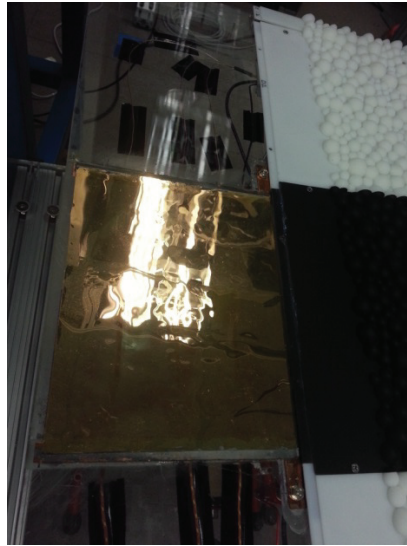


Figure 3.8: Gold deposited Mylar film between copper electrodes

The conductive silver paint between the copper electrodes and the Mylar film ensures limited contact resistance. Because the resistance of the Mylar film is high compared to the copper electrodes and the silver paint, almost all of the heat loss occurs over the Mylar film.

The installation procedure for the Mylar film was as follows. Latex gloves were worn during the procedure to reduce the chance of oils being transferred to the film. The film was cut to size. The application area between the copper electrodes was sprayed with 3M Super 77 adhesive. The center of the film was gently pressed to the surface, and a brayer was used to roll the film out to avoid any air pockets beneath the film. Because



any damage to the film can create a non-uniform heating scheme, great care was taken to reduce the chances of film damage.

*Tail.* A closer look at the tail fin is shown in Figure 3.9. The tail serves as a deterrent to preferential flow over the top of the airfoil. The cross-sectional area of the tail is approximately equal to the cross sectional area of all the instrumentation below the test plate. Therefore the tail helps to ensure that more air is not forced over the top of the plate rather than the bottom, and the mass balance is therefore more equal. Should air from the bottom of the test plate be forced over the top of the test plate, flow separation would occur more easily. Both the tail and the bull nose on the leading edge help to prevent any flow separation as the flow encounters the test plate.



Figure 3.9: Tail fin

Roughness panels. The roughness panels are desired to resemble realistic icing data acquired by Anderson et al. [25] and Shin [23]. Two different roughness schemes were chosen from Anderson et al. to serve as the “target roughness” to match. These cases were referred to as 052996 run 4 and 053096 run 1. Anderson et al. published mean droplet diameter given a range of icing conditions. Shin published data for droplet spacing for a range of mean droplet diameters. These results could be used in combination to conclude what an icing surface should look like given a set of icing parameters. The roughness pattern on each panel is based on these results. A complete roughness panel from the 053096 pattern is shown in Figure 3.10.



Figure 3.10: Finished roughness panel from the 053096 pattern

The first step in creating one of these roughness panels is to use a Lagrangian droplet simulator to create a two-dimensional droplet profile. This simulator produces a



text file with the x and y location of the center of each droplet, along with each droplet's diameter. To operate the simulator, the user enters the simulation area, the impinging droplet diameter, the contact angle between the incoming droplets and the surface, and the number of droplets to impinge. This simulator then runs the following algorithm steps shown in coding diagram in Figure 3.11.

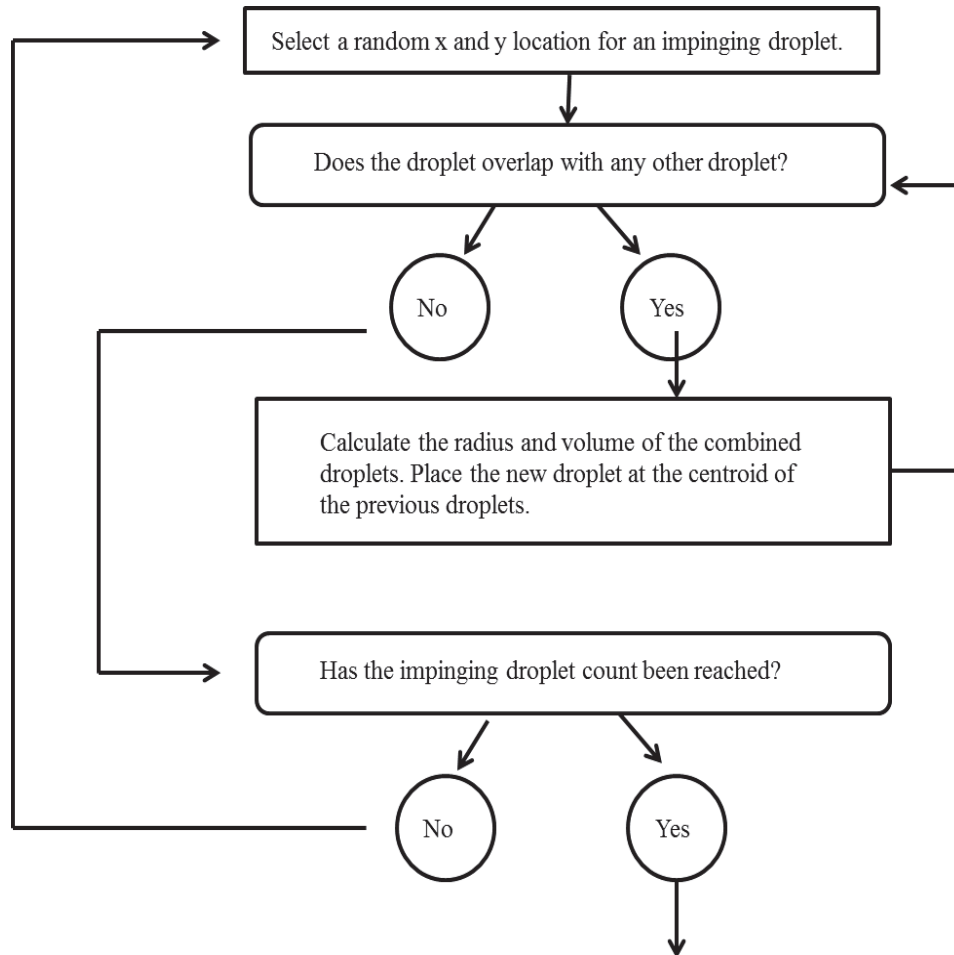


Figure 3.11: Coding diagram for the Lagrangian droplet simulator

Note that the simulator checks if the droplets overlap to simulate coalescence of water droplet molecules. This is a key part of the simulator that helps to make the droplet distribution more realistic.

After being run through the simulator, it was noted that the results varied from the target roughness in three areas: 1) overall average element diameters, 2) diameter standard deviation, and 3) spacing-to-diameter ratio. A series of three data conditioning steps was performed to address each of these issues. The smaller diameters were truncated, the roughness elements were stretched, and finally the roughness elements were scaled in such a way as to closely match the parameters seen in Anderson's [25] experiments. For a more detailed explanation as to how these transformations were performed see Tecson [5]. A visual representation of this process is shown in Figure 3.12, and Tables 3.1 and 3.2 show key parameters at each stage of the conditioning. Note that  $D_{\text{mean}}$  is the mean diameter of the roughness elements,  $S_E$  is the standard deviation of the roughness pattern,  $P$  is the distance between roughness elements, and  $H$  is element height.

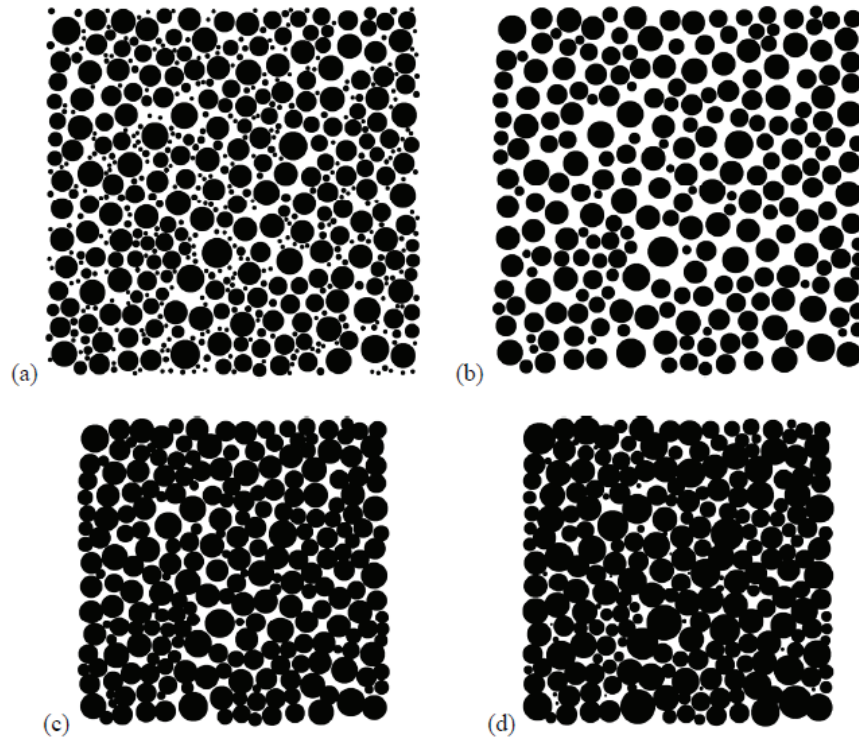


Figure 3.12: a) Raw simulator output, b) truncated results, c) truncated and stretched results, d) truncated, stretched, and scaled results

Table 3.1: Key parameters of the “052996 Run 4” case at various stages of conditioning [5]

Parameter	Reported Data [23,26]	Unconditioned Simulator Data	Truncated	Truncated and Stretched	Truncated, Stretched, and Scaled
$D_{\text{mean}}$ (mm)	0.936	0.583	1.037	1.037	1.037
$S_E$ (mm)	0.372	0.410	0.254	0.254	0.381
$(P/D)_{\text{mean}}$	N/A	1.330	1.057	0.878	1.032
$P_{\text{mean}}/D_{\text{mean}}$	1.2	0.979	1.012	0.840	0.840
H/D	0.515	0.50	0.50	0.50	0.50

Table 3.2: Key parameters of the “53096 Run 1” case at various stages of conditioning [5]

Parameter	Reported Data [23,26]	Unconditioned Simulator Data	Truncated	Truncated and Stretched
$D_{\text{mean}}$ (mm)	0.573	0.472	0.586	0.586
$S_E$ (mm)	0.148	0.201	0.152	0.152
$(P/D)_{\text{mean}}$	N/A	1.143	1.143	0.870
$P_{\text{mean}}/D_{\text{mean}}$	1.2	1.014	1.014	0.840
H/D	0.515	0.50	0.50	0.50

Once the data statistics were similar to the statistics of the target patterns, it was then scaled up by a factor of ten, so that the test section velocity could be reduced from 67 m/s to 6.7 m/s. This scaled data was then formed into a repeatable 15 cm by 15 cm square unit. This unit could then be repeated to fill a 60 cm by 90 cm area, as shown in Figure 3.13.

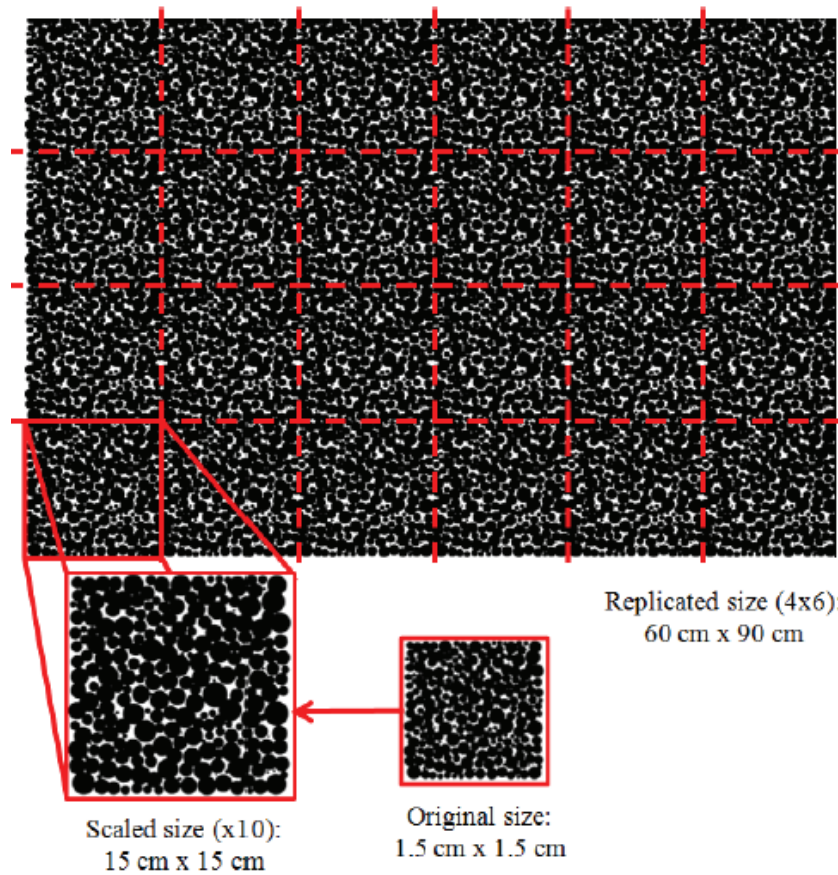


Figure 3.13: Simulator data transformation to fill the entire test plate [5]

This data was then converted into three-dimensional roughness in SolidWorks. Because the printable area of the rapid prototyper is only 20 cm by 20 cm, the 60 cm by 90 cm area shown in Figure 3.13 was divided into 25 smaller sections. Figure 3.14 shows the finalized SolidWorks 052996 roughness pattern with nomenclature used to identify rows and columns. Rows A and E are 0.75'' wide, rows B and D are 7.25'' wide, and row C is 8'' wide. Column 1 is 6'' long, while columns 2 through 5 are 7.25'' long. The roughness panels were printed on an Objet 30 and a Dimension 768 SST. Because of the Objet 30's better resolution, it was used to print row C, as this is the row being measured

with the IR camera. Note that row C is painted with flat black spray paint so that the camera can assume an emissivity of 0.95 in its measurements. This is also the emissivity value used in the data reduction.

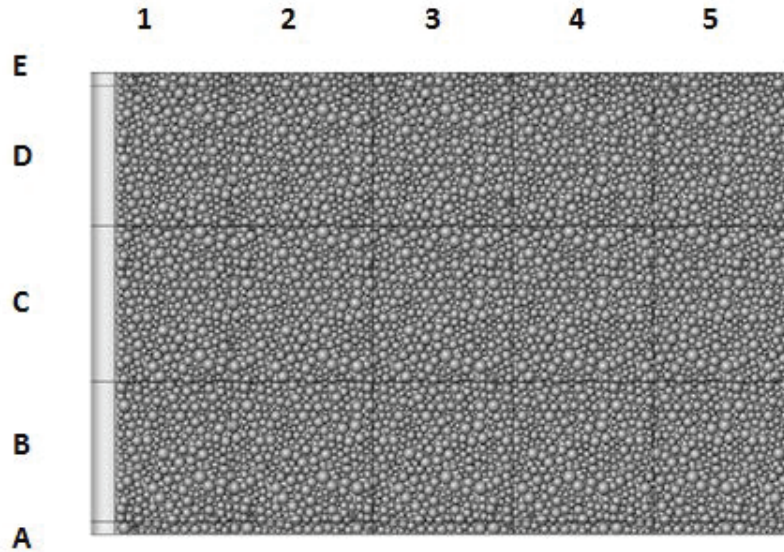


Figure 3.14: 052996 SolidWorks model roughness scheme with row and column nomenclature

The roughness creation process is long, but the steps are relatively simple. The roughness panel creation process can be summarized in the following steps:

- 1) The Lagrangian droplet simulator was used to produce 2D roughness data.
- 2) The simulator data was conditioned to fit more realistic results.
- 3) The conditioned data was Reynolds scaled and a repeatable element was fitted to a 60 cm by 90 cm area.
- 4) The 2D data was converted to 3D data in SolidWorks.
- 5) The area was broken into 25 smaller sections and rapid prototyped.

After the roughness panels were created, a 1/16'' piece of neoprene was attached to the back of the roughness panels with adhesive to ensure good contact pressure



between the roughness panels and the Mylar. #4 1.25'' long screws were then run through the holes in the roughness panels and #4 nuts were used to secure the roughness panels onto the test plate. The tightness of the nuts was adjusted to ensure the panels fit together as smoothly as possible. Final products of the smooth-turbulent, 052996, and 053096 roughness patterns are shown in Figure 3.15. Note that the smooth-laminar pattern is simply the smooth-turbulent pattern without the leading-edge trip strip.



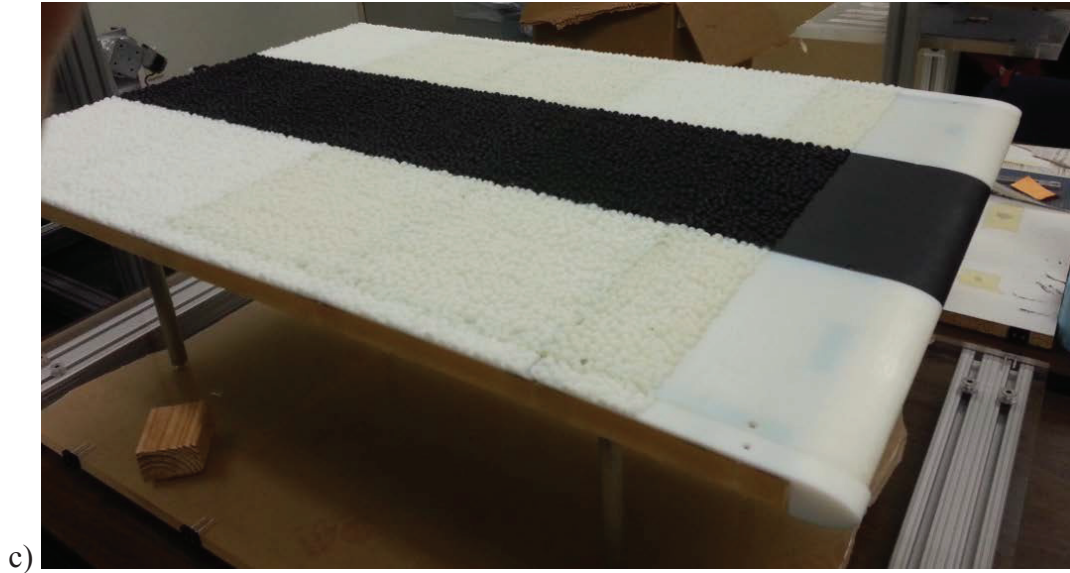


Figure 3.15: Completed roughness panels for the a) turbulent calibration, b) 052996 pattern, and c) 053096 pattern

*Infrared camera.* The camera used was a FLIR SC4000 ThermoVision, shown in Figure 3.16. The IR camera has a 25 mm lens, and an indium-antimonide (InSb) detector capable of generating 320 by 256 pixel maps. As can be seen, it was attached to the traversing system via a metal plate and screws. This allowed the camera to traverse smoothly to each viewing section.



Figure 3.16: FLIR SC4000 IR camera

*Traversing system.* Two traversing systems have been created depending on the desired test. Figure 3.17a shows the one-dimensional traversing system that changes the position of the IR camera. This is the traversing system used in the heat transfer coefficient tests. Figure 3.17b shows the two-dimensional traversing system that carries the temperature probe. This is the traversing system used in the thermal boundary layer tracing tests. Both traversing systems use a Velmex VXM stepper motor to move along the support. These motors are controlled via a Labview interface.

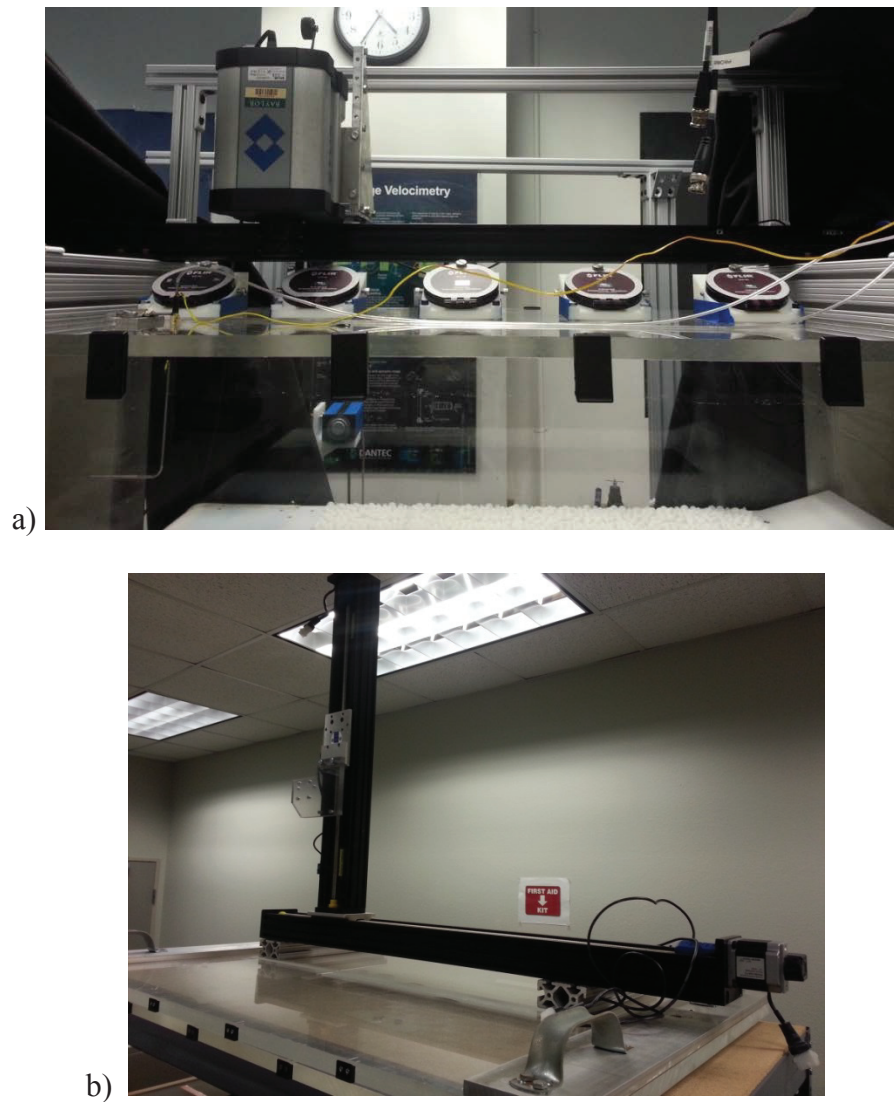


Figure 3.17: Traversing system for the a) IR camera and b) thermal boundary layer probe



*IR window system.* Because radiation does not pass through Plexiglas freely, a set of five FLIR IRW-3C calcium-fluoride windows were needed for proper temperature measurements with the IR camera. The windows, shown in Figure 3.18a, were installed at an angle of  $30^\circ$  to avoid the camera measuring the reflected radiation from itself. To create the angles needed for the windows, the SolidWorks drawing shown in Figure 3.18b was rapid prototyped to serve as a window support system. This support system is also partly visible in Figure 3.18a. The support has four screw holes to hold the part in place, and two set screw holes to hold the window in place.

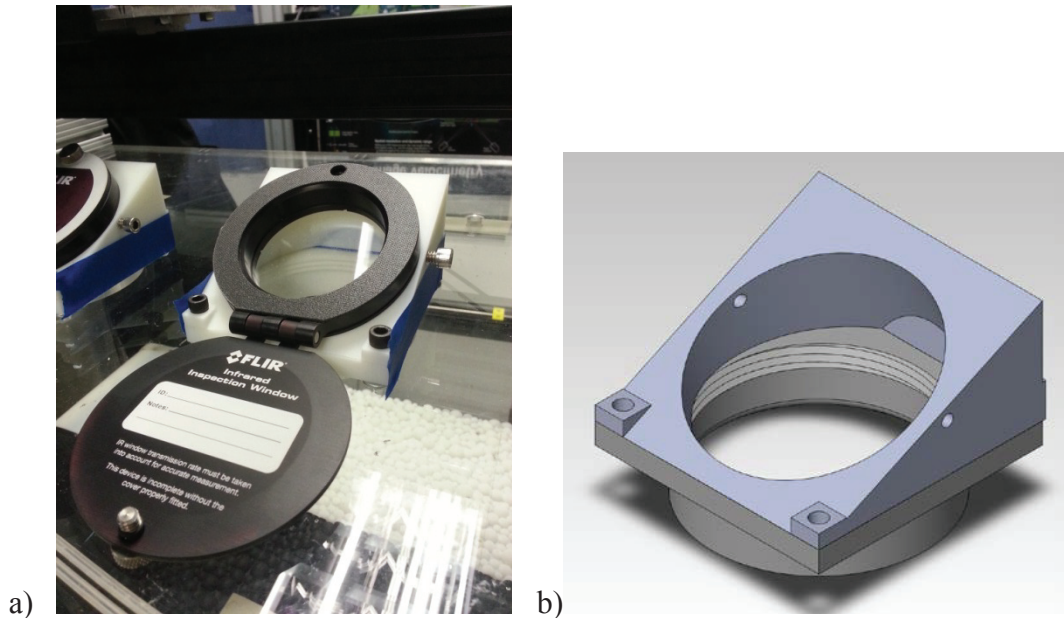


Figure 3.18: a) IR windows and b) window support system

*Pitot-static probe.* The pitot-static probe was installed above the leading edge of the test plate. The pressure difference was measured with an Omega PCL-2A pressure transducer and a PCL-MA-01WC pressure module. This allowed the freestream velocity to be calculated and monitored using a Labview interface.

*Measurement cart.* The measurement cart, shown in Figure 3.19 houses the current transducers, data acquisition (DAQ) systems, power sources, and the voltage meter and ammeter for section four. The current in section 0 was measured using a Powertek CTH/20A/TH/24Vdc Type 1 current transducer. The current in sections 1, 2, and 3 were measured using Powertek CTH/10A/TH/24Vdc Type 1 current transducers (Figure 3.19a). The current transducer measurements were read using an NI 9205 DAQ module. The heat voltage measurements were read using an NI 9229 DAQ module. The thermocouples were read using NI 9211 DAQ modules. These modules were stored in an NI cDAQ-9172 chassis. All DAQ modules are shown in Figure 3.19b. Five BK Precision power supplies were used to heat the five test sections (Figure 3.19c). This cart, shown in Figure 3.19d, was created in Tecson [5]; additional details can be found in that work. The cart allows the roughness patterns to be easily switched. It can be detached from the test plate and rolled away when the wind tunnel test section is removed, and then rewired to the test plate when the next pattern is ready.

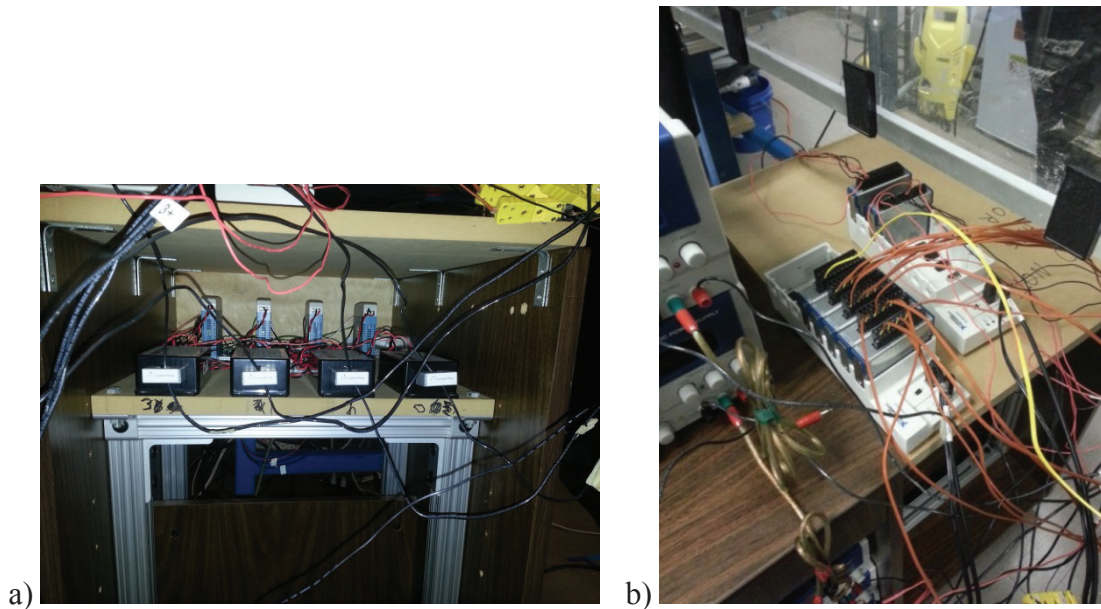




Figure 3.19: a) Current transducers, b) DAQ modules, c) power sources, and d) whole cabinet

*Labview monitoring.* A Labview interface was used to record the data from the DAQ modules, the data from the PCL-2A, and the inlet properties of the tunnel. Labview was also used to program the stepper motor used in the traversing system. This allowed for a Labview program to be used to move the IR camera from window to window. A similar program was used in maneuvering the thermal boundary layer probe. This program will be discussed in more detail in the methods section.

*Baylor University subsonic wind tunnel.* The tunnel used in this experiment was a Model 406B from Engineering Laboratory Design Inc. The tunnel's cross sectional area is 24 inches by 24 inches, with a length of 48 inches. A honeycomb inlet provides a low inlet turbulence intensity of approximately 0.2%.

*Z-series inlet measurements.* A zTHP-P sensor was placed near the inlet of the tunnel. The sensor measures pressure, temperature, and relative humidity. These values were wirelessly transmitted to interface with Labview. These measurements were used to obtain flow properties.

*Thermal boundary layer probe.* A T-type thermocouple attached to a 20'' aluminum probe was used to trace the thermal boundary layer. Figure 3.20 shows the thermocouple probe attached to the two-dimensional traversing system.

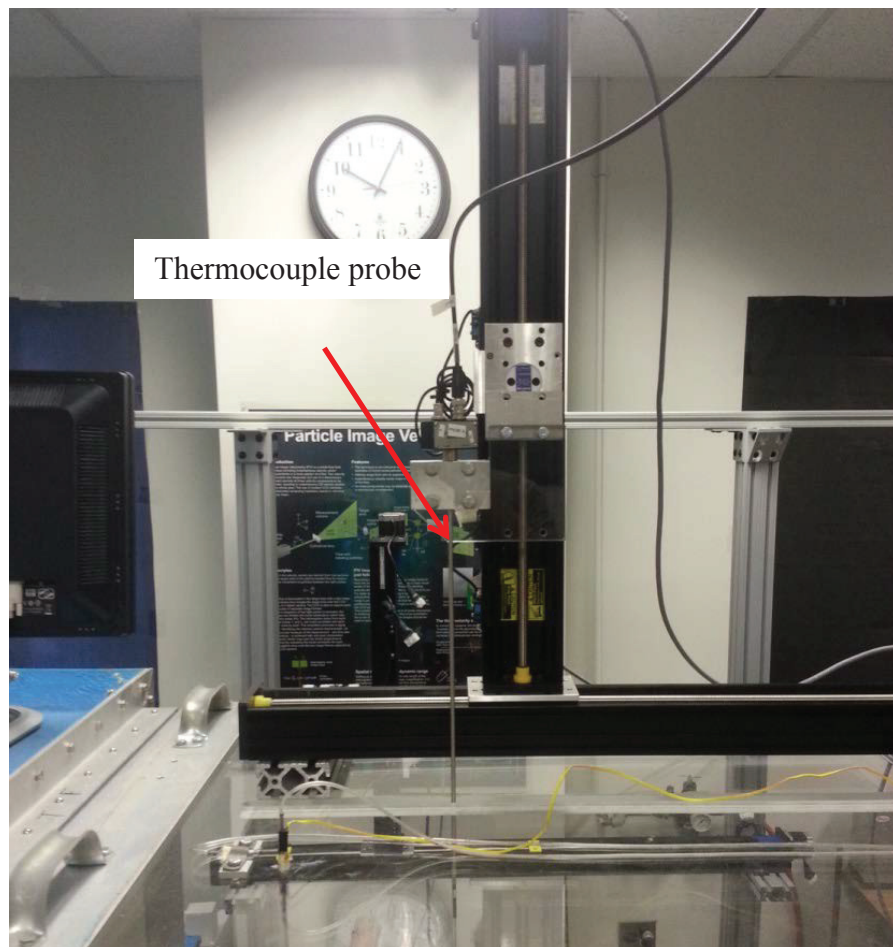


Figure 3.20: Thermocouple probe and traversing system



## *Methods*

Two sets of experiments were performed on each roughness pattern: 1) a heat transfer coefficient experiment and, 2) a thermal boundary layer trace. This section outlines the procedure that was followed for each of these experiments.

*Heat transfer experiment.* There were a few key procedures that were followed the day before testing. The desired roughness scheme was attached to the plate. An effort was made to ensure smooth transitions from panel to panel, and no bowing occurred across the panels. The test plate was raised into the test section of the wind tunnel. The test plate was wired to the measurement cart, and pre-tests were performed to make sure all DAQ inputs were functioning properly. The camera was then focused the day before to allow plenty of time to settle before taking measurements.

The day of testing, the IR camera was powered on and allowed to sit for at least fifteen minutes before any measurements were taken. This allowed the internal temperature of the camera to decrease to its necessary value. The DAQ systems and the current transducers were also powered on. The IR camera software and Labview programs were started. In order to prevent light contamination in the IR camera measurements, a black felt shroud was placed over the test section, shown in Figure 3.21, and the lights directly over the test section were turned off.

To begin testing, the PCL-2A pressure transducer for the pitot-static probe was zeroed. The IR camera was moved to the IR window directly above section zero. The Labview program that reads all DAQ and Z-series measurements was started. The Labview program that controls the stepper motor for the traverse was also started. The camera then recorded 70 frames at a rate of 7 Hz with a pixel map of 256 x 320. The time

the video was taken on the Labview file was recorded. The camera was then moved to the other four sections (using the Labview stepper motor programs) and a video was recorded. When the camera was moved to section four, the voltage and current were manually recorded from the Supermeters into an excel spreadsheet. This initial set of videos is referred to as the calibration videos.



Figure 3.21: Test section covered with black felt shroud

The power sources were then turned on, and the system was allowed to reach steady state before the previous video taking process was repeated. The system typically required two hours to reach steady state. After the measurements were taken for one set of boundary conditions, the power sources were then adjusted for another set of boundary conditions, and the system was allowed to reach steady state. Four different sets of boundary conditions were run in these experiments: a constant heat flux case, a decreasing heat flux case, an increasing heat flux case, and an unheated starting length

case. Table 3.3 gives the target heat flux values for the power sources to be matched to in the experiment.

Table 3.3: Target heat flux values to be matched for boundary conditions

Heating Scheme	Section 0 Flux ( $\text{W/m}^2$ )	Section 1 Flux ( $\text{W/m}^2$ )	Section 2 Flux ( $\text{W/m}^2$ )	Section 3 Flux ( $\text{W/m}^2$ )	Section 4 Flux ( $\text{W/m}^2$ )
Case I	500	500	500	500	500
Case II	300	400	500	500	500
Case III	500	400	300	300	300
Case IV	0	0	500	500	500

All cases were run on the same day to minimize changing air properties. If air properties change too drastically, although Stanton numbers can be directly compared, convection coefficients cannot. For this reason the constant heat flux cases from Tecson [5] were rerun for direct comparison. If the door to the lab was opened, the inside air properties would change slightly. For this reason, great efforts were taken to minimize traffic in and out of the lab while testing was in progress. The system was given time to steady itself if the door was opened before videos were taken. A new set of videos was recorded if the door was opened while a set of videos was being recorded.

*Thermal boundary layer traces.* To perform these tests, the desired roughness pattern was placed into the test section. The wind tunnel ceiling was changed to the two-dimensional traverse, shown in Figure 3.16b. The pitot-static probe, PCL-2A pressure transducer, z-series inlet measurements, and freestream thermocouple from the heat transfer experiments were also used in this experiment. A type T thermocouple was used

as a probe, and was measured through a Labview interface with a NI 9211 DAQ module on an NI-cDAQ-9172 chassis.

The set of heat flux boundary conditions to be measured was chosen. The PCL-2A was zeroed, the Labview software was started, and the tunnel was run at the same velocity as the heat transfer tests. The probe was then lowered as close as possible (within 1/32'') to the surface of the location being measured. A Labview program was designed to run a 6'' trace using 101 geometrically expanding points (with an expansion factor of 1.07). At each point 140 samples were taken at a rate of 14 samples per second. For the 052996 roughness pattern, boundary layer traces were taken at the center of each roughness panel in row c (the black roughness panels that were tested). For the 053096 roughness pattern, boundary layer traces were taken at the center of each roughness panel in row c, and at the smooth to rough transition. This process was performed for all four sets of heating boundary conditions on all roughness patterns except the smooth-laminar.

### *Transmissivity Experiment*

In Tecson [5] it was assumed that there was a transmissivity factor associated with the IR windows. In other words, it was assumed that radiation from the plate was not the radiation being measured by the camera, because of losses in the IR windows. A transmissivity of 0.82 was assumed because it benchmarked the experimental data for the smooth turbulent case to the theoretical prediction for heat transfer coefficients for turbulent flow over a flat plate. An experiment was designed to test this assumption. This section outlines the materials used in the experiment, and the experimental procedure involved with the experiment.



## Materials

Figure 3.22 shows the general test setup for the transmissivity experiment. As can be seen it uses most of the same equipment as the heat transfer experiment. However, this setup uses a different test plate in the tunnel. The list of components is as follows:

- A) The transmissivity test plate
- B) IR camera
- C) IR windows
- D) Pitot-static tube
- E) Cabinet of measurement devices
- F) Labview interface
- G) Baylor University Subsonic wind tunnel

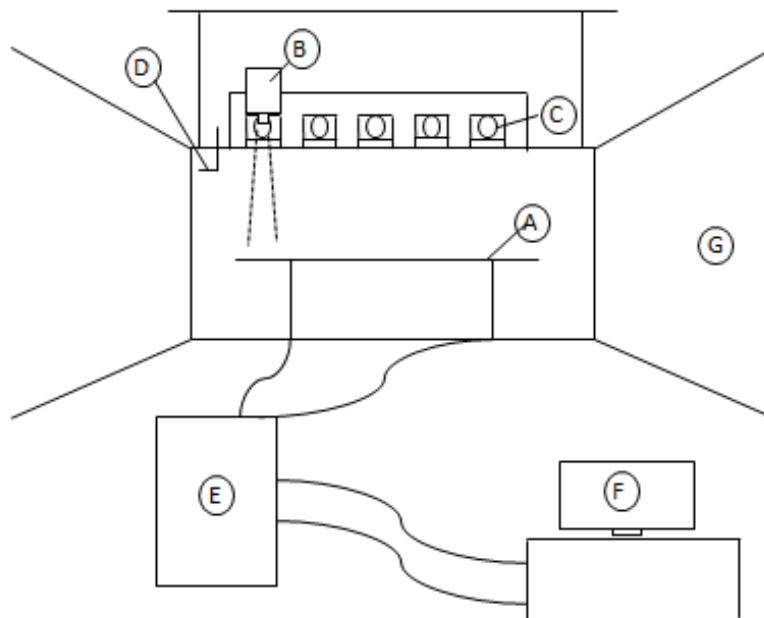


Figure 3.22: General test setup for the transmissivity experiment

Components B through G are the same equipment used in the heat transfer experiments. See the previous materials section for more details on that equipment. The

transmissivity test plate will be described in more detail, as it is different from the test plate used in the heat transfer experiments.

*Transmissivity test plate.* A more detailed look at the transmissivity test plate is given in Figure 3.23. The transmissivity test plate is similar to the roughness test plate in that it has a 3/4" Plexiglas base plate, with two 1/2" grooves for the copper electrodes. Gold Mylar is placed between the electrodes and connected with silver paint. This serves as the heating element for the transmissivity plate. The Plexiglas base plate is held in place by two 1515 80/20 aluminum supports. It was adjusted to sit at a height of 12", which is the same height that the roughness test plate sits. The distance between the test area and the camera was desired to be the same as in the heat transfer test as to not affect the IR temperature measurements.

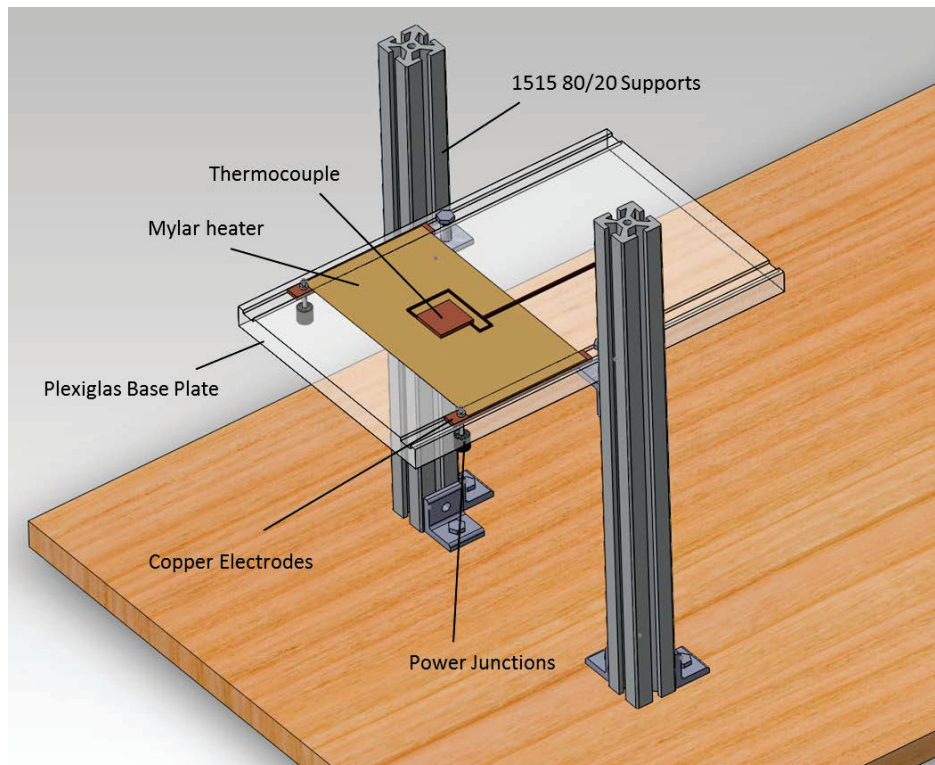


Figure 3.23: Transmissivity test plate

A thermocouple was created and attached to the Mylar heater with epoxy. The thermocouple was attached in such a way as it would sit in the middle of the IR viewing area, and then the heater and thermocouple were spray painted with flat black spray paint (for an assumed emissivity value of 0.95) This thermocouple, shown in Figure 3.24, essentially uses a square 1.25'' piece of copper as the bead. To accomplish this, type K thermocouple wire was soldered to the square piece of copper. This copper bead averages out any temperature effects, and gives the camera a large area make temperature measurements. To calibrate this thermocouple, it was used as a K-type and then dipped into an ice bath and a pot of boiling water. In both cases, an offset of 0.6°C higher than the theoretical temperatures of 0°C and 100°C. This offset was then applied to obtain a true thermocouple reading. The temperature of the camera could then be compared to thermocouple reading to identify a transmissivity value.

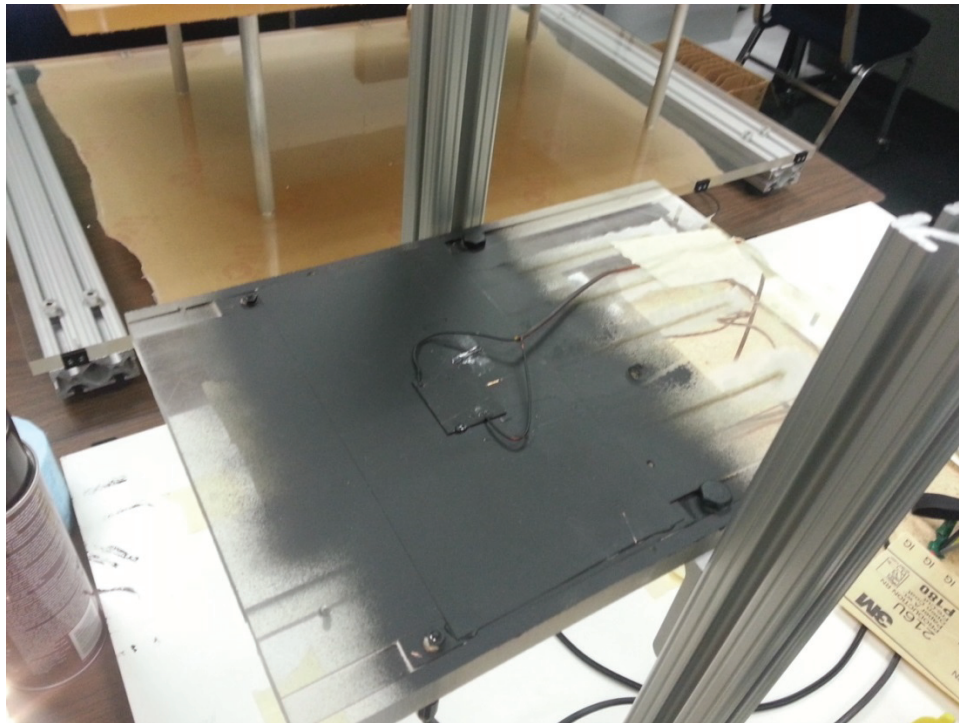


Figure 3.24: Large thermocouple created in-house

The plate was wired using the same equipment used to measure section zero of the heat transfer experiments. The heater was powered with a BK Precision power supply. The current was measured with a Powertek CTH/20A/TH/24Vdc Type 1 current transducer, and read with a NI 9205 DAQ module in an NI cDAQ-9172 chassis. Instead of going through a DAQ module, the voltage was measured using a Newport TrueRMS HHM290/N Supermeter. The thermocouple was read using a NI 9211 DAQ module, in an NI cDAQ-9172 chassis. The pitot-static probe and the PCL-2A pressure transducer were still used to obtain the test section velocity.

### *Methods*

The initial objective of this experiment was to identify a transmissivity value by comparing the temperature of the thermocouple to the temperature measured by the IR value. Therefore, conditions that affect this in the heat transfer experiments were carried into the transmissivity experiment, such as the tunnel velocity and camera settings.

As in the heat transfer experiments, the camera was focused the day before the transmissivity experiment. The day of the experiment the camera was turned on and allowed to sit for a minimum of fifteen minutes. The transmissivity test plate was put into the test section of the wind tunnel, and wired. The test section was covered with a black felt shroud and the overhead lights were turned off to help block light contamination. The Labview file used to record the data was opened. The tunnel was turned on and run at the same velocity as in the heat transfer experiments. The camera then recorded 70 frames at a rate of 7 Hz with a pixel map of 256 x 320. The time the video was taken on the Labview file was noted. The heater was then turned on to a low voltage and current to yield a low temperature increase. Another video was then taken. This process was then

repeated for five thermocouple temperatures ranging from 20°C to 40°C, as this was the range of temperatures witnessed in the heat transfer experiments.

It is important to note that it was assumed the transmissivity values of each IR window would be the same. Therefore only the transmissivity of the IR window in section zero was measured.

### *Plexiglas Thermal Conductivity*

Rather than assume the manufacture's given thermal conductivity value of 0.18 W/mK, an experiment was designed to measure the thermal conductivity of the Plexiglas base plate. One reason for this was the epoxy filled thermocouple channels in the base plate. It was hypothesized that the 1/8'' channel of epoxy could increase the total thermal conductivity of the system.

### *Materials*

To accomplish the objective of measuring the thermal conductivity, two identical Plexiglas plates were attached together, with a heater in the middle, as shown in Figure 3.25. Because the objective was to measure the thermal conductivity of the Plexiglas-epoxy system, the plates were prepared in the same way as the roughness test plate was built. The plates were 8'' by 8'' with a 3/4'' thickness. The plates were machined with a 1/8'' thermocouple channel that ran from the center of the plate to an inch from the edge. A hole was drilled at the end of the channel to allow the wire to escape. K-type adhesive thermocouples were placed onto the back of the test plates. K-type thermocouples were also placed into the channels, and then filled with epoxy. Once the epoxy dried, the

excess epoxy was ground off, and the surface of the Plexiglas roughed up, as this was the procedure followed in Tecson [5]. This step is shown in Figure 3.26.

Both plates were machined with half inch electrode channels. One plate had a set of copper electrodes that were 8'' long, while the other had a set of electrodes that were 8.75'' long. This was done to allow power connections to be set up at the edge of the test plate. Gold deposited Mylar was attached between the electrodes using 3M Super 77 adhesive, with the conductive side down to the set of longer electrodes (termed the power side). Silver paint was placed between the Mylar and the electrodes to ensure low contact resistance. The final two plates are shown in Figure 3.27.

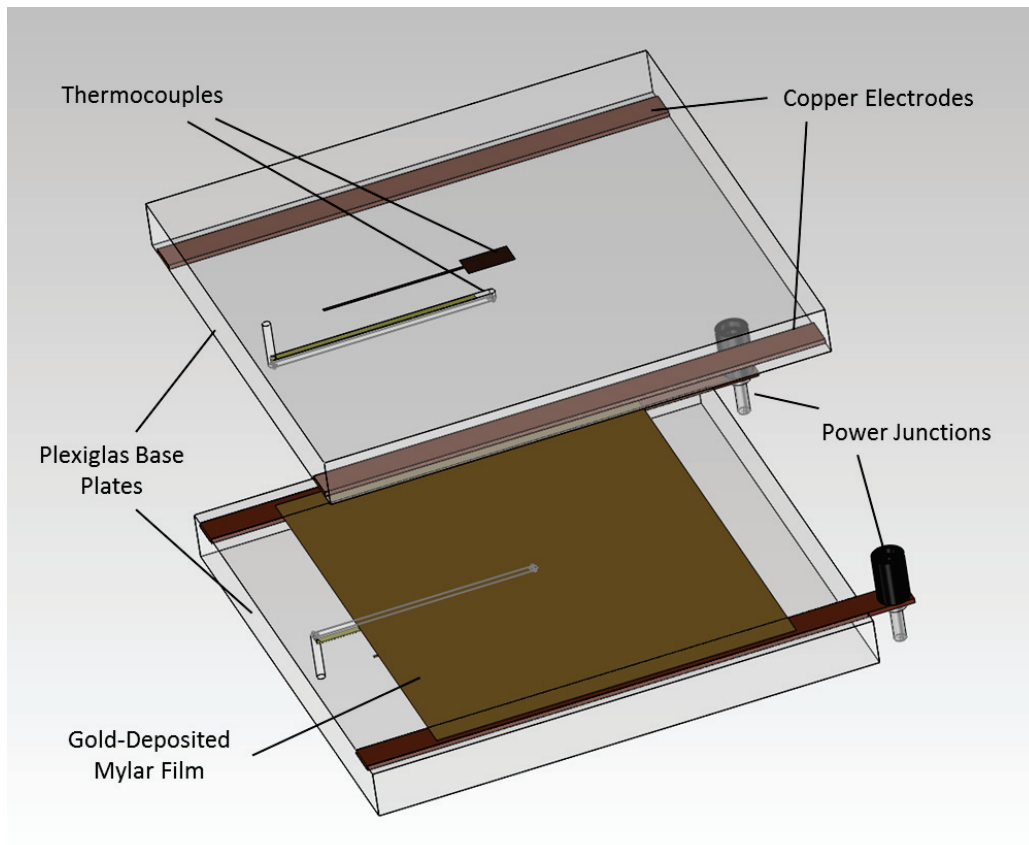


Figure 3.25: Thermal conductivity plates



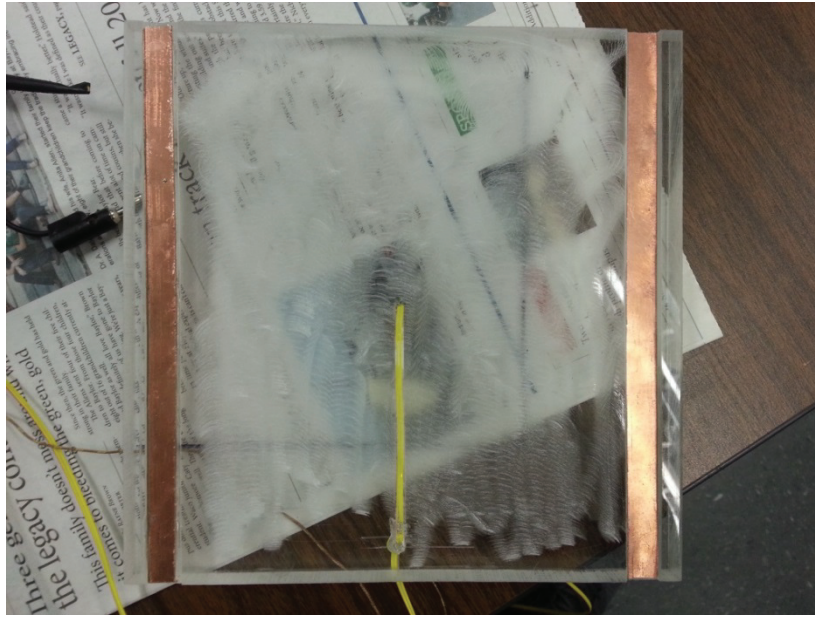


Figure 3.26: Thermal conductivity plate after grinding off excess epoxy

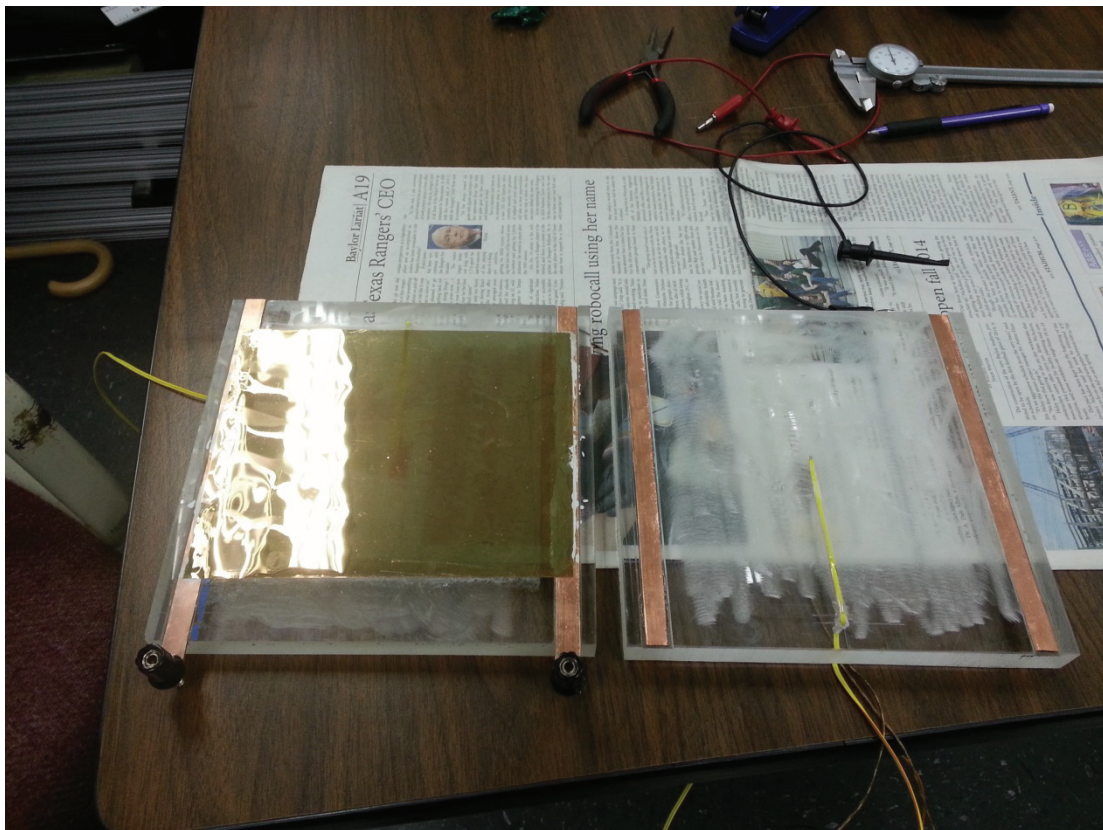


Figure 3.27: Thermal conductivity plates

The voltage and the current through the Mylar were measured using two Newport TrueRMS HHM290/N Supermeters. The four thermocouples were read using a NI 9211 DAQ module, in an NI cDAQ-9172 chassis, so that a Labview interface could be used. The heater was powered using a BK precision power supply.

### *Methods*

To begin testing, the two plates were tightly taped together so that the thermocouples were aligned as closely as possible. The plates were then clamped at the edges to ensure low contact resistance. The plates were set on a small piece of Styrofoam (to minimize any heat losses through the bottom of the system), the equipment was wired, and the necessary Labview program was started. Two fans were placed on each side of the plates at an equal distance to keep the heat loss one dimensional. The jet impingement that occurs on the face plate creates a thermal resistance that is much lower than the side walls of the test plate. Therefore, with jet impingement occurring on the outside of the plates, the heat loss is more likely to occur through the face of plate, rather than towards the edges of it. This concept is illustrated in Figure 3.28.

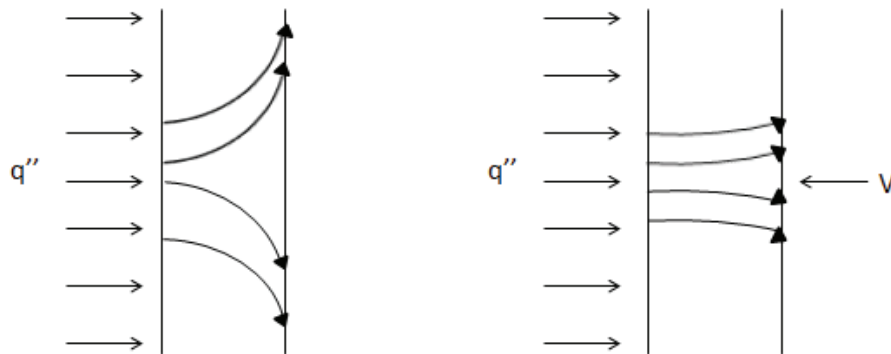


Figure 3.28: Increase in validity of 1-D assumption with jet impingement



The fans and the heater were powered. The system was allowed to come to steady state. The voltage, current, and time from the Labview file were manually recorded. The plates during the experiment are shown in Figure 3.29.

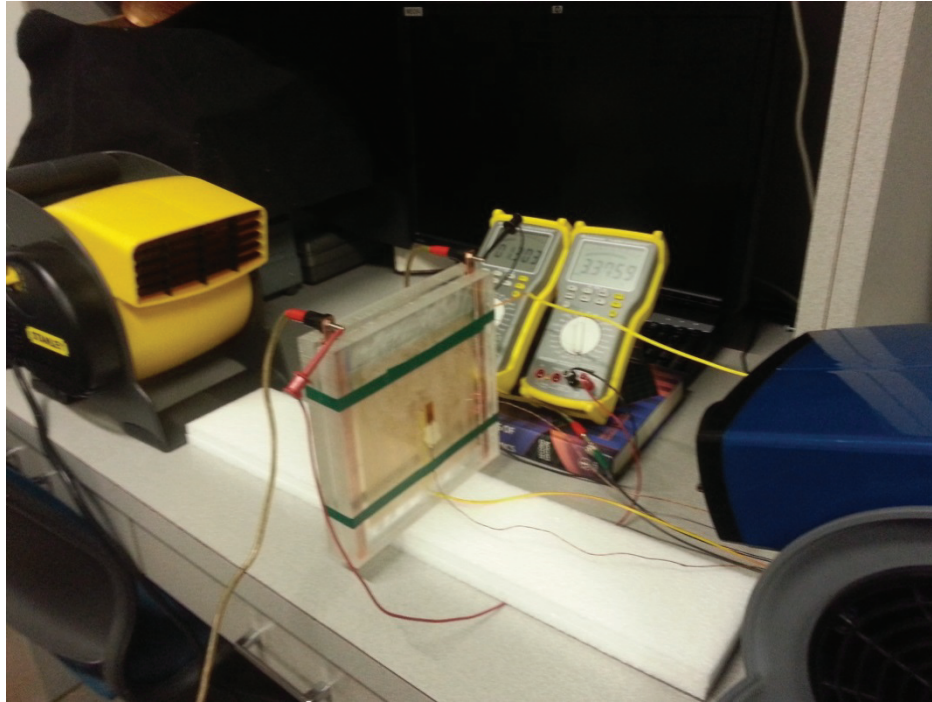


Figure 3.29: Thermal conductivity plates during testing

## CHAPTER FOUR

### Data Reduction and Uncertainty Analysis

In this chapter, the data reduction process used in each the three experiments is developed, and the uncertainty analysis used in each case is presented. These processes are first presented for the transmissivity experiment, followed by the thermal conductivity experiment, and finally the roughness experiments.

#### *Transmissivity Experiment*

The purpose of this experiment was to compare IR camera measurements to thermocouple measurements. As discussed in Chapter Three, the thermocouple used was an in-house constructed thermocouple with a 0.5'' by 0.5'' piece of copper to serve as the bead. This allowed for an area averaged temperature to be obtained for the IR measurements. To do this, the set of videos at the highest temperature was used to identify the four corner pixels of the thermocouple (the thermocouple was clearly distinguishable when the transmissivity test plate was hotter). The pixels were then averaged to obtain an IR measurement. The thermocouple was calibrated to the IR measurements in the same manner as the heat transfer experiments.

No explicit data reduction equation and no uncertainty analysis were needed for this experiment. As the results in Chapter Five will show, the temperature reading from the IR camera was within 0.1°C to the temperature readings from the thermocouple. For this reason, it was assumed that the transmissivity value of all the windows was equal to one. Therefore, the end result of this experiment was not the production of a

transmissivity value, but rather to serve as a justification for removing it from the analysis performed in Tecson [5].

### *Thermal Conductivity Experiment*

#### *Data Reduction*

The purpose of this experiment was to obtain a thermal conductivity value to be used in the roughness experiments. The energy balance for the experimental procedure described in Chapter 3 is shown in Figure 4.1, and the thermal circuit for this energy balance is shown in Figure 4.2.

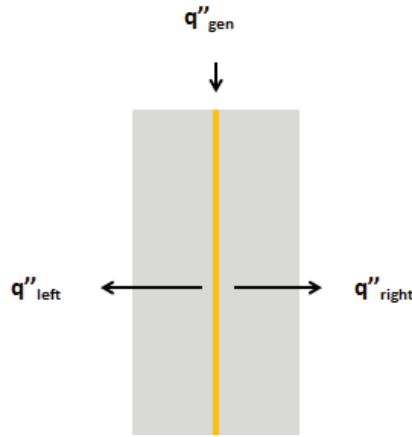


Figure 4.1: Energy balance for the thermal conductivity experiment

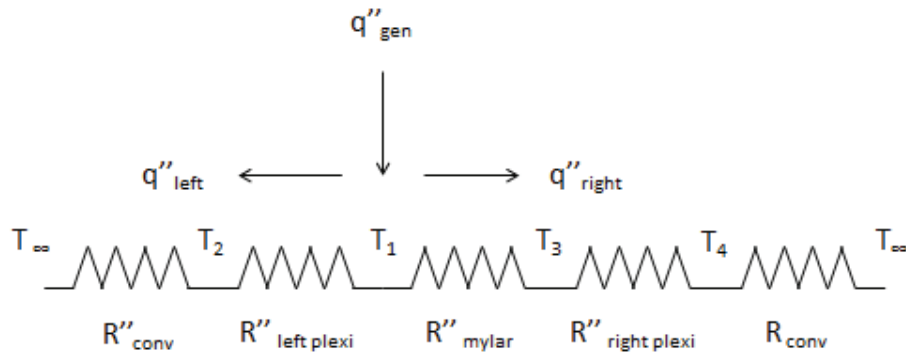


Figure 4.2: Thermal circuit for the thermal conductivity experiment

Using an energy balance, the generated heat flux entering the plate must be equal to the heat that leaves the system through the left side plus the heat that leaves the system through the right side, as Eq. 4.1 shows.

$$q''_{gen} = q''_{left} + q''_{right} \quad (4.1)$$

Because the thermal circuit for  $q''_{left}$  and  $q''_{right}$  is a series circuit, these can be calculated as shown in Eq. 4.2 and Eq. 4.3.

$$q''_{left} = \frac{T_1 - T_2}{R''_{left}} = \frac{T_1 - T_2}{\frac{t}{k_p}} \quad (4.2)$$

$$q''_{right} = \frac{T_3 - T_4}{R''_{right}} = \frac{T_3 - T_4}{\frac{t}{k_p}} \quad (4.3)$$

Note that it has been assumed that the thermal conductivity and the plate thickness of the left and right Plexiglas plates are the same. Substituting in Eq. 4.2 and Eq. 4.3 into Eq. 4.1 and then rearranging to solve for  $k_p$  produces Eq. 4.4.

$$k_p = \frac{q''_{gen} t}{T_1 - T_2 + T_3 - T_4} \quad (4.4)$$

Substituting in the definition of power into Eq. 4.4 yields the data reduction equation, Eq. 4.5.

$$k_p = \frac{\frac{EI}{A_t} t}{T_1 - T_2 + T_3 - T_4} \quad (4.5)$$

### *Uncertainty Analysis*

Because the conduction term was benchmarked to theoretical results, uncertainties were not propagated through the convection coefficient measurements. Consequently

only uncertainties associated with the plate temperature measurements are propagated.

The thermocouples were calibrated to the average of the initial readings of the four thermocouples, as shown in Eq. 4.6.

$$T_{TC,cal} = T_{TC,S} - \left( T_{TC,C} - \frac{(T_{TC,C1} + T_{TC,C3} + T_{TC,C3} + T_{TC,C4})}{4} \right) \quad (4.6)$$

### *Roughness Experiments*

#### *Data Reduction*

*Heat transfer experiments.* To fully understand how convection heat transfer coefficients are obtained, the data reduction equation will be derived. Consider a general energy balance for the test plate shown in Figure 4.3. The gray strip on the bottom is the Plexiglas base plate, the gold strip is the Mylar heater, the black strip is the neoprene, and the gray rough surface on top is a roughness panel.

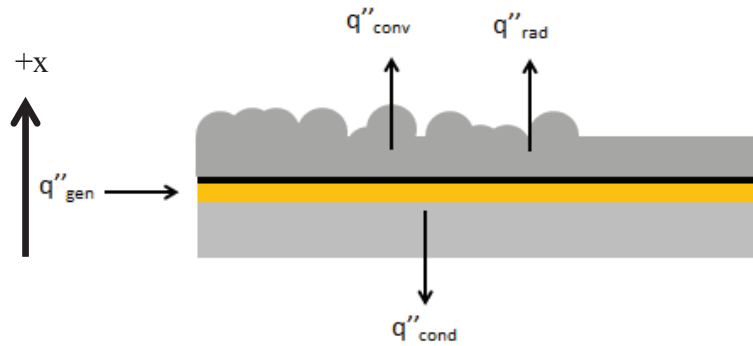


Figure 4.3: Visual 1-D energy balance for roughness test plate

If only the heat transfer modes shown in Figure 4.3 are considered, then the general energy balance is given by Eq. 4.7.

$$q''_{gen} = q''_{cond} + q''_{conv} + q''_{rad} \quad (4.7)$$

If all other terms are accounted for, then heat loss due to convection can be calculated, and therefore the convection coefficients can be calculated. A derivation of each of these heat transfer terms will be presented, focusing first on the conduction term. The derivation for the conduction through the bottom of the test plate begins with the heat diffusion equation shown in Eq.4.8.

$$\frac{\partial}{\partial x} \left( k_p \frac{\partial T}{\partial x} \right) + \frac{\partial}{\partial y} \left( k_p \frac{\partial T}{\partial y} \right) + \frac{\partial}{\partial z} \left( k_p \frac{\partial T}{\partial z} \right) + \dot{q} = \frac{1}{\alpha} \frac{\partial T}{\partial t} \quad (4.8)$$

The bottom of the test plate was assumed to act as a one-dimensional wall with constant thermal conductivity at steady state. Making these assumptions and simplifying, Eq. 4.8 can be written as Eq. 4.9

$$\frac{d^2 T}{dx^2} = 0 \quad (4.9)$$

This ordinary differential equation can be easily solved with the set of boundary conditions shown in Eq. 4.10 and 4.11, where  $T_{SS}$  is the temperature just below the Mylar (subsurface),  $T_{UP}$  is the temperature under the Plexiglas (under Plexiglas), and  $t_p$  is the thickness of the bottom of the test plate.

$$T(x = 0) = T_{SS} \quad (4.10)$$

$$T(x = t_p) = T_{UP} \quad (4.11)$$

With these boundary conditions, the solution to Eq. 4.8 is given by Eq. 4.12.

$$T(x) = \frac{T_{UP} - T_{SS}}{t_p} x + T_{SS} \quad (4.12)$$

The conductive heat flux is defined in Eq. 4.13.

$$q''_{cond} = -k_p \frac{dT}{dx} \quad (4.13)$$

Differentiating the obtained temperature profile in Eq. 4.12, and substituting into Eq. 4.13 yields the conductive heat flux term given in Eq. 4.14.

$$q''_{cond} = -\frac{k_p}{t_p}(T_{UP} - T_{SS}) \quad (4.14)$$

Regarding the radiation, the surroundings of the test plate are assumed to be black body. The test plate itself is assumed to have known emissivity. Therefore the heat loss due to radiation is given in Eq. 4.15.

$$q''_{rad} = \varepsilon\sigma(T_{IR}^4 - T_{sur}^4) \quad (4.15)$$

Because the heater is supplied with known current and voltage, heat flux generation is derived simply from the electrical definition of power. The result is shown in Eq. 4.16, where  $E$  is voltage,  $I$  is current, and  $A_m$  is the area of the Mylar heater.

$$q''_{gen} = \frac{EI}{A_m} \quad (4.16)$$

Now that the conduction, radiation, and generation terms have been obtained, the only term remaining is the convective term. The convection term comes from Newton's law of cooling and is written as Eq. 4.17.

$$q''_{conv} = h(T_{IR} - T_{\infty}) \quad (4.17)$$

Combining Eqs. 4.7, 4.14, 4.15, 4.16, and 4.17 the convection heat transfer coefficient can be solved for, yielding the premature data reduction equation. This equation was used to obtain the raw results later discussed in Chapter Five.

$$h = \frac{\frac{EI}{A_m} - \frac{k_p}{t_p}(T_{SS} - T_{UP}) - \varepsilon\sigma(T_{IR}^4 - T_{sur}^4)}{T_{IR} - T_{\infty}} \quad (4.18)$$

To arrive to this point, it has been assumed that the heat flux through the plate acts as one dimensional, meaning there is no lateral conduction through the test plate. It is

further assumed that the heat flux through the Plexiglas is uniform, and the temperature on the bottom of the Plexiglas is uniform.

Smooth roughness panel validation. Similar to Tecson [5], a smooth set of roughness panels was used to judge how accurately Eq. 4.18 compares to theoretical convective heat transfer coefficients for flat plate flow with constant heat flux boundary conditions. One set of roughness panels was completely smooth to produce laminar flow, and another set of roughness panels was smooth with a leading-edge trip strip to produce turbulent flow. The laminar roughness panels have a Reynolds number of 400,000 near the end of the test plate. Therefore, assuming a critical Reynolds number of 500,000 the flow should be laminar over the entire test plate.

Three figures will be given for each validation case: 1) a steady-state temperature map for each of the five test sections, 2) a convective heat transfer map for each of the five test sections, and 3) a  $\pm 0.5''$  span-wise average of the convective heat transfer coefficients along the entire length of the test plate. For the Matlab code used to generate these three figures, and all other figures like this throughout the work, see Appendix A. The laminar and turbulent theoretical correlations for constant heat fluxes are given in Eq. 4.19 and Eq. 4.20 respectively.

$$h_{lam} = 0.453 Re^{\frac{1}{2}} Pr^{\frac{1}{3}} k_f x^{-1} \left( 1 - \left( \frac{\zeta}{x} \right)^{\frac{3}{4}} \right)^{-\frac{1}{3}} \quad (4.19)$$

$$h_{turb} = 0.0308 Re^{\frac{4}{5}} Pr^{\frac{1}{3}} k_f x^{-1} \left( 1 - \left( \frac{\zeta}{x} \right)^{\frac{9}{10}} \right)^{-\frac{1}{9}} \quad (4.20)$$



Zeta in the theoretical equations refers to the unheated starting length of the test plate. This accounts for the length of the bullnose and the leading edge that the flow encounters until the location of the first Mylar heater. These equations were used to produce the theoretical convection coefficient lines shown in Figures 4.6 and 4.9.

It is important to note that the validation results shown in Figures 4.4-4.9 have been processed using Eq. 4.18, the premature data reduction equation. Figures 4.4 and 4.7 present the temperature profiles (K) for laminar and turbulent flow. Figures 4.5 and 4.8 present the convective heat transfer coefficient contour maps ( $W/m^2K$ ) for laminar and turbulent flow. Figure 4.6 and 4.9 are the  $\pm 0.5''$  span-wise convective heat transfer coefficient averages for laminar and turbulent flow.

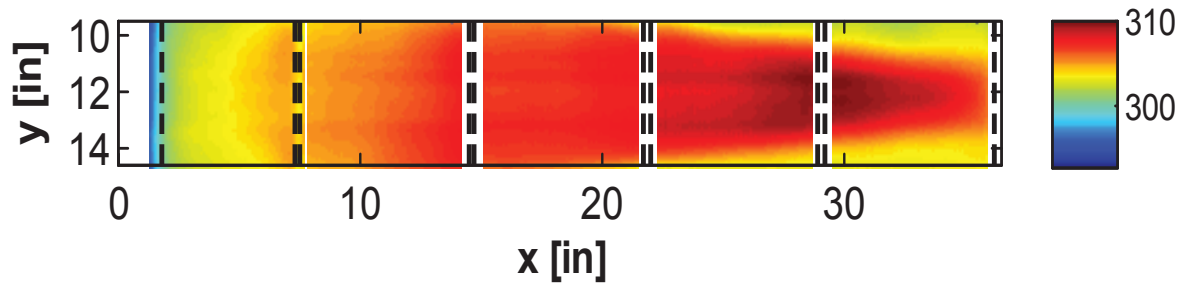


Figure 4.4: Smooth-laminar temperature profile (K)

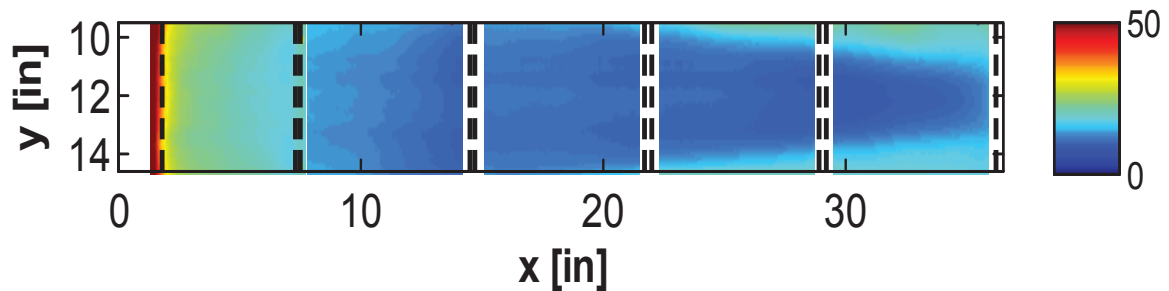


Figure 4.5: Smooth-laminar convective map ( $W/m^2K$ )

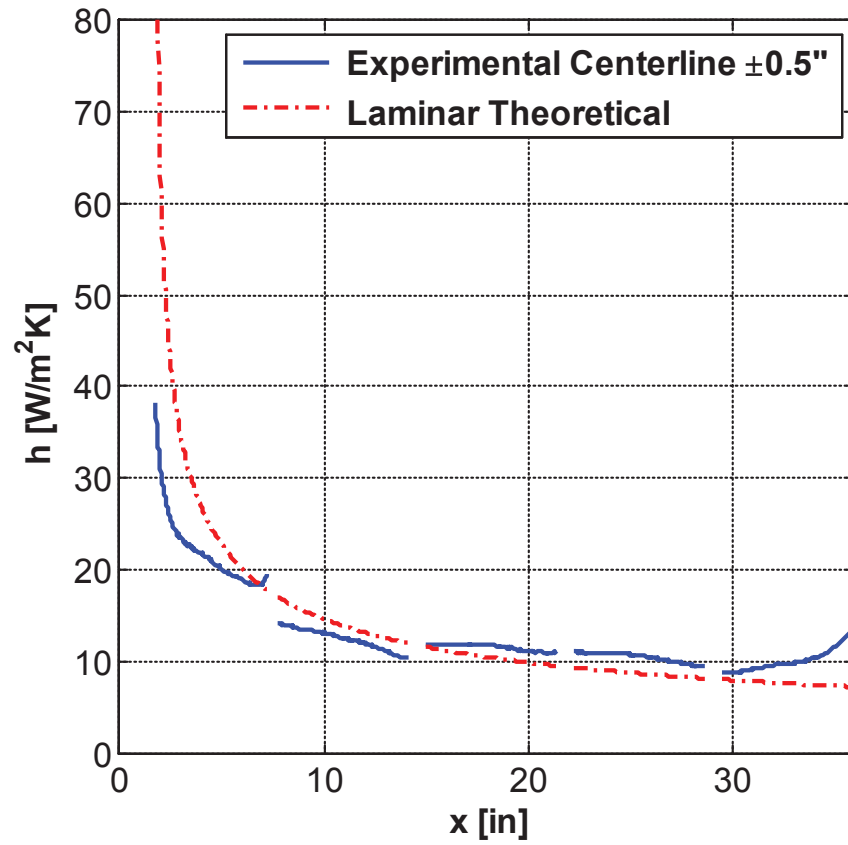


Figure 4.6: Smooth-laminar  $\pm 0.5''$  average centerline (raw results)

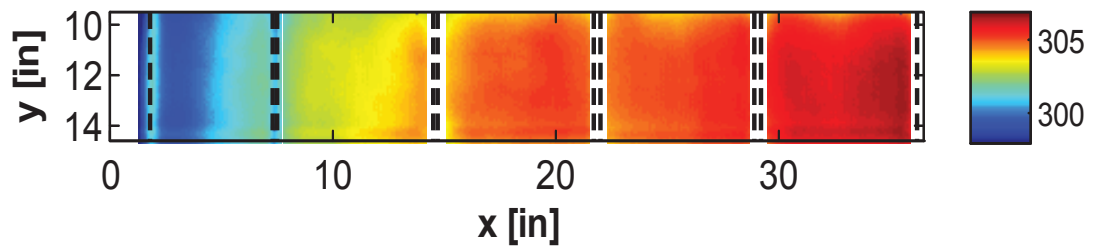


Figure 4.7: Smooth-turbulent temperature profile (K)

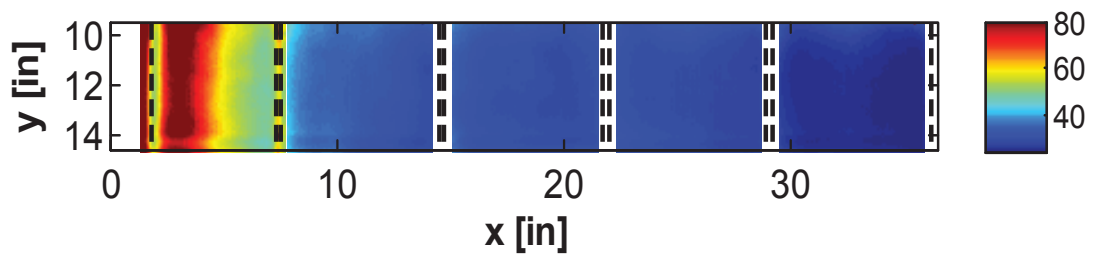


Figure 4.8: Smooth-turbulent convective map ( $\text{W/m}^2\text{K}$ )

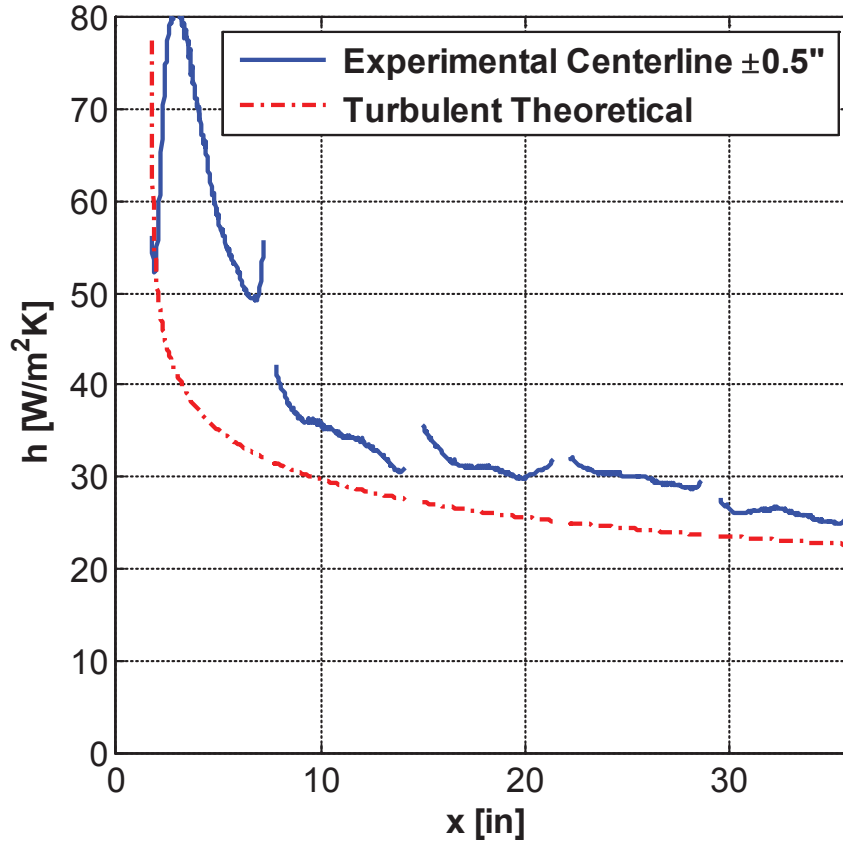


Figure 4.9: Smooth-turbulent  $\pm 0.5''$  average centerline (raw results)

The last step to obtain the finalized data reduction equation is to introduce conduction correction coefficients. Figures 4.4 and 4.7 contain slight deviations between the obtained results and the theoretical convection coefficients. The data is also not as smooth from section to section as would be expected, because smooth temperature profiles are present in Figures 4.4 and 4.7. It has been hypothesized that these deviations occur due to slight variations in thermal conductivity and thermocouple spacing at different sections along the plate. Because these are properties of the plate, a correction value,  $c_c$ , for each test panel was added to the conductive term to benchmark experimental results to theoretical predictions. Because the same coefficients could be used to benchmark both the laminar and turbulent validation cases, the theory that

thermocouple spacing and thermal conductivity were causing these deviations was reinforced. The finalized data reduction equation is given in Eq. 4.21.

$$h = \frac{EI - c_c \frac{k_p}{t} (T_{SS} - T_{UP}) - \varepsilon \sigma (T_{IR}^4 - T_{Sur}^4)}{T_{IR} - T_{\infty}} \quad (4.21)$$

The coefficients used to correct the conductive term are given in Table 4.1. Figures 4.6 and 4.9 have been plotted again using the finalized data reduction equation in Figures 4.10 and 4.11. Note that in both the laminar and turbulent validation cases, the plots are smoother and more closely match the theoretical convective values. It is important to note that the turbulent theoretical prediction, Eq. 4.20, assumes flow transition immediately upon contact with the trip strip. In reality it takes approximately four inches for the flow to transition to fully turbulent flow. For this reason the experimental results in Figure 4.11 are shifted to the right of the theoretical values.

Table 4.1: Conduction correction coefficient values	
Section Number	Conduction correction coefficient
Section 0, $c_0$	0.9
Section 1, $c_1$	0.9
Section 2, $c_2$	1.05
Section 3, $c_3$	1.1
Section 4, $c_4$	1.05

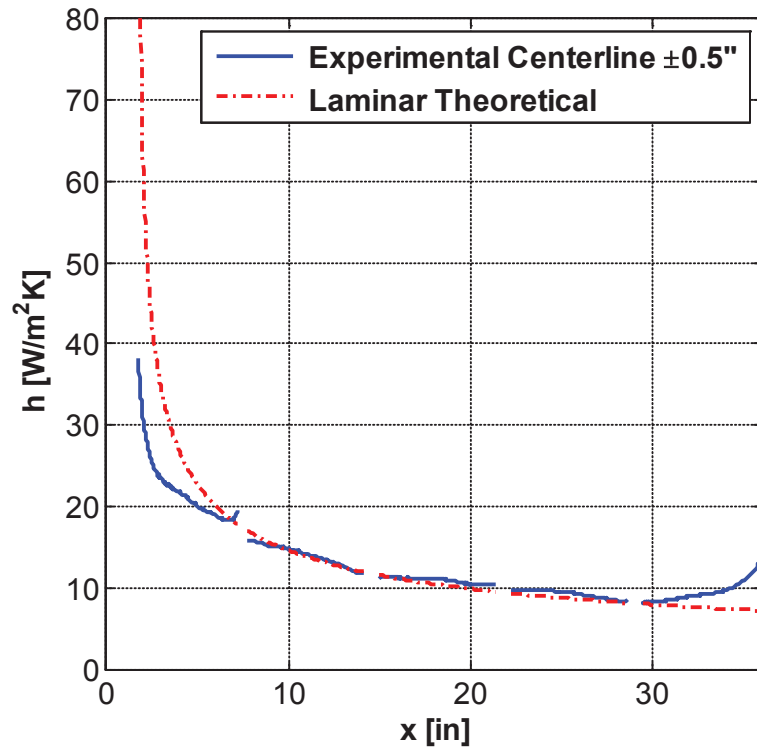


Figure 4.10: Smooth-laminar  $\pm 0.5''$  average centerline (finalized results)

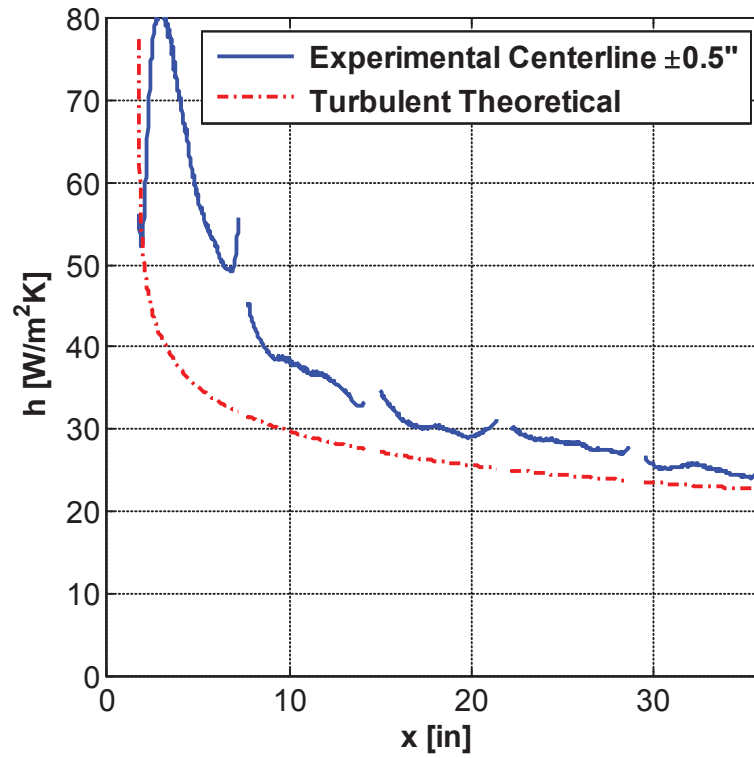


Figure 4.11: Smooth-turbulent  $\pm 0.5''$  average centerline (finalized results)

Air properties. Convection coefficients vary based on air properties. Because data for different roughness patterns was recorded on different days, air properties recorded for these experiments were different. Therefore, for direct comparison, non-dimensional Stanton numbers can be used. However, to convert heat transfer data to non-dimensional numbers requires a method of obtaining air property data.

The method for obtaining air properties is the same one used in Mart [35], as well as Tecson [5]. As explained in Chapter Three, an Omega z-series monitor was used to obtain temperature, pressure, and relative humidity at the inlet of the wind tunnel. Using the International Association for the Properties of Water and Steam guidelines [36], Sutherland's law [37], and Wilke's equation for gas mixtures [38], air density, dynamic viscosity, thermal conductivity, and the Prandtl number were calculated.

Thermocouple calibration. All thermocouples were calibrated to the averaged center 50x50 IR camera temperature reading, in the fashion shown in Eq. 4.22.

$$T_{TC,cal} = T_{TC,S} - (T_{TC,C} - T_{IR}) \quad (4.22)$$

Note that the thermocouples in each section were calibrated to the IR camera reading for that respective section. For example, the first three thermocouples are in section zero, and were therefore calibrated to the camera reading at section zero. The transmissivity experiment proved that the camera was accurate, and as a result it was decided to calibrate to the IR camera measurements. The IR measurements are not calibrated to the freestream temperature as they were in Tecson [5]; they are taken as the true temperature readings.

The surrounding temperature was taken to be the average of the freestream readings at each of the five sections, Eq. 4.23. The changes seen in the freestream temperature at each section were small, and it was assumed that the system did not have enough time to respond to these small changes.

$$T_{\infty} = \frac{(T_{FS0} + T_{FS1} + T_{FS2} + T_{FS3} + T_{FS4})}{5} \quad (4.23)$$

*Thermal boundary layer traces.* For consistency purposes, the thermal boundary layer traces were processed in a similar manner as Tecson [5]. The temperature measurements were nondimensionalized as shown in Eq. 4.24, where  $T_{Probe}$  is the temperature measured by the temperature probe,  $T_S$  is the predicted surface temperature, and  $T_{\infty}$  is the freestream temperature.

$$\theta = \frac{T_{Probe} - T_S}{T_{\infty} - T_S} \quad (4.24)$$

Because the camera was not used in the boundary layer traces, the surface temperatures had to be predicted using the convective heat transfer coefficients from the heat transfer experiments. It should be noted that because the camera was not present in these calculations, it could not be used in the calibration procedure. Instead, the last 20 measurements of the section zero boundary layer trace were averaged and used in the calibration procedure. These measurements were well outside the boundary layer and offered an accurate temperature measurement to calibrate the test plate thermocouples.

### *Uncertainty Analysis*

The uncertainty analysis was handled similarly to Tecson [5], with the key exception being the thermal conductivity term and the plate thickness term. Because the

conductive term was corrected to match theoretical results for the smooth plate, the uncertainty parameters in the conductive term (thermal conductivity and plate thickness) were not thought to propagate through the convection coefficient measurements. In chapter five, an averaged 50 x 50 pixel area directly above each of the eight thermocouple pairs is used to calculate eight convective heat transfer coefficients. The uncertainty analysis for those results will be explained here. The Mathcad file used to do this analysis is provided in Appendix B.

Fixed uncertainties were obtained from manufacturer data, and random uncertainties were obtained using the large sample method from Coleman and Steele [39]. Table 4.2 provides uncertainty calculations for each parameter in the data reduction equation. Random uncertainty is given by Eq. 4.25, where N is the sample size, S is the standard deviation, and t is the Student's t-value.

$$U_{rand} = \frac{(t_{st} S)}{\sqrt{N}} \quad (4.25)$$



Table 4.2: Uncertainty calculations for each parameter in data reduction

Variable	Total Uncertainty	Uncertainty Components
$E$	$\sqrt{U_{E\_fixed}^2 + \left(\frac{t_{st}S_E}{\sqrt{N}}\right)^2}$	$U_{E\_fixed} = 0.03\% E$ (sections 0-3) $U_{E\_fixed} = 0.25\% E$ (section 4)
$I$	$\sqrt{U_{I\_fixed}^2 + \left(\frac{t_{st}S_I}{\sqrt{N}}\right)^2}$	$U_{I\_fixed} = 0.1 \text{ A}$ (section 0) $U_{I\_fixed} = 0.05 \text{ A}$ (sections 1-3) $U_{I\_fixed} = 2.5\% I$ (section 4)
$A_t$	$\sqrt{(U_{d\_fixed}W_{ha})^2 + (U_{d\_fixed}L_{ha})^2}$	$U_{d\_fixed} = 1/32''$
$T_{IR}$	$\sqrt{\left(\frac{t_{st}S_{T_{IR}}}{\sqrt{N}}\right)^2 + B_T^2}$	$B_T = 1.4 \text{ K}$
$T_{SS}$	$\sqrt{\left(\frac{t_{st}S_{T_{SS}}}{\sqrt{N}}\right)_s^2 + \left(\frac{t_{st}S_{T_{SS}}}{\sqrt{N}}\right)_c^2 + \left(\frac{t_{st}S_{T_{IR}}}{\sqrt{N}}\right)_c^2 + B_T^2}$	$B_T = 1.4 \text{ K}$
$T_{UP}$	$\sqrt{\left(\frac{t_{st}S_{T_{UP}}}{\sqrt{N}}\right)_s^2 + \left(\frac{t_{st}S_{T_{UP}}}{\sqrt{N}}\right)_c^2 + \left(\frac{t_{st}S_{T_{IR}}}{\sqrt{N}}\right)_c^2 + B_T^2}$	$B_T = 1.4 \text{ K}$
$T_\infty$	$\sqrt{\left(\frac{t_{st}S_{T_\infty}}{\sqrt{N}}\right)_s^2 + \left(\frac{t_{st}S_{T_{IR}}}{\sqrt{N}}\right)_c^2 + B_T^2}$	$B_T = 1.4 \text{ K}$

## CHAPTER FIVE

### Results and Discussion

This chapter presents the results of the previously discussed experiments and discusses their implications. The results of the transmissivity experiment will be presented first, followed by the results of the thermal conductivity experiment, as these directly influence the results of the roughness experiments. Finally the results of the roughness experiments (heat transfer tests and thermal boundary layer traces) will be presented.

#### *Transmissivity Experiment Results*

After using the processing techniques presented in chapter four, the IR and thermocouple temperatures shown in Table 5.1 were acquired. These results have also been plotted in Figure 5.1.

Table 5.1: IR-Thermocouple Comparison for Transmissivity Experiment			
Reading Number	IR Temperature (°C)	Thermocouple Temperature (°C)	Temperature Difference (°C)
Reading 1	21.28	21.22	-0.06
Reading 2	23.69	23.63	-0.06
Reading 3	27.07	27.04	-0.03
Reading 4	31.35	31.49	0.06
Reading 5	35.82	35.93	0.09

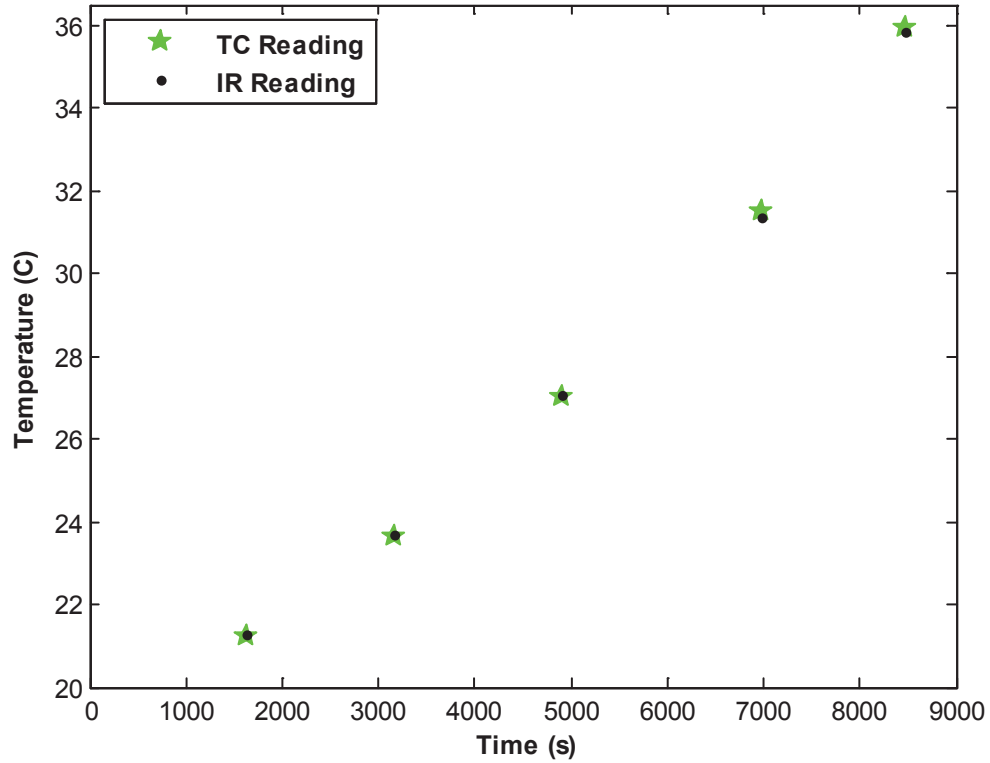


Figure 5.1: IR-Thermocouple Comparison

As Table 5.1 and Figure 5.1 show, the temperature values measured with the IR camera and the temperature values measured with the thermocouple are quite similar, with the largest percent difference of 0.11%, or 0.09°C. These results demonstrate that the transmissivity value of 0.82 used in Tecson [5] was not appropriate and that the factor most affecting Tecson's results was an incorrect evaluation of conduction losses through the Plexiglas base plate. These results also indicate that the IR window does not have a significant effect on the transmission of radiation over the operating temperatures used in the heat transfer experiments. Note that these results are for the IR window at section zero; therefore it was further assumed that results for the remaining four windows would be similar.

### *Thermal Conductivity Experiment Results*

The data obtained in the thermal conductivity experiment is presented in Table 5.2, where  $E$  is voltage,  $I$  is current,  $q$  is heat flux,  $T_1$ ,  $T_2$ ,  $T_3$ , and  $T_4$  are the thermocouple temperatures, and  $k$  is the thermal conductivity. Figure 5.2 serves as a legend to identify which thermocouples correspond to  $T_1$ ,  $T_2$ ,  $T_3$ , and  $T_4$ .  $T_1$  and  $T_2$  are on the conductive side of the Mylar film; hence these temperatures are slightly higher than  $T_3$  and  $T_4$ . Note that in an effort to obtain the thermal conductivity for the range of thermal conditions experienced in the heat transfer tests, three runs were performed at different heat fluxes.

Table 5.2: Data from Thermal Conductivity Experiment

Parameter	Run 1	Run 2	Run 3
$E$ (V)	1.9975	2.975	3.6792
$I$ (A)	0.769	1.113	1.412
$q$ (W/m <sup>2</sup> )	63.74	137.39	215.56
$T_1$ (°C)	24.70	29.02	32.25
$T_2$ (°C)	21.73	22.95	22.72
$T_3$ (°C)	24.52	28.52	31.60
$T_4$ (°C)	21.95	23.08	22.92
$k$ (W/mK)	0.2008	0.208	0.2064

As can be seen from Table 5.2, the thermal conductivity value was repeatable for a range of heat flux values. The thermal conductivities increase slightly as temperature rises, as would be expected. The manufacturer value, and the value used in Tecson [5] was 0.18 W/mK. The experimental value of 0.205 W/mK was slightly higher than this. As expected, the presence of the epoxy does change the effective thermal conductivity of the system.

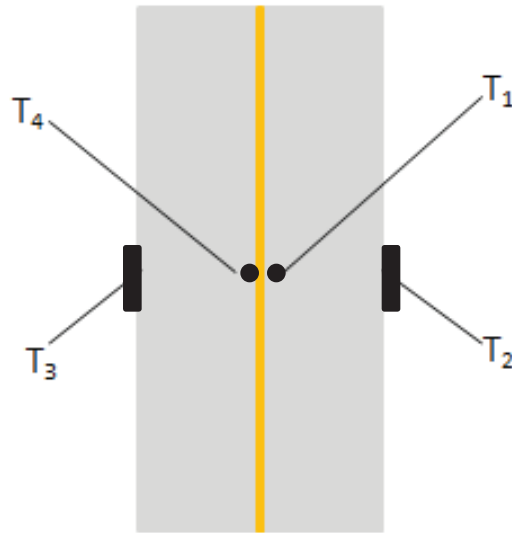


Figure 5.2: Legend for thermocouple temperatures in Table 5.1

### *Roughness Experiment Results*

*Heat transfer experiments.* This section provides the results for the heat transfer experiments on the roughness panels using the data reduction described in chapter four. In this set of experiments, four different heating boundary conditions were performed on each of the four roughness patterns: a constant case, an increasing case, a decreasing case, and an unheated starting length case. Therefore, sixteen different cases were run. Figures 5.3-5.6 show the convective heat transfer maps produced from the data reduction equation, and Figures 5.7-5.10 show the one inch lateral average along the center of the test plate. These figures are provided for all boundary conditions, where in all the presented figures the order is a) constant heat flux, b) decreasing heat flux, c) increasing heat flux, d) unheated starting length.

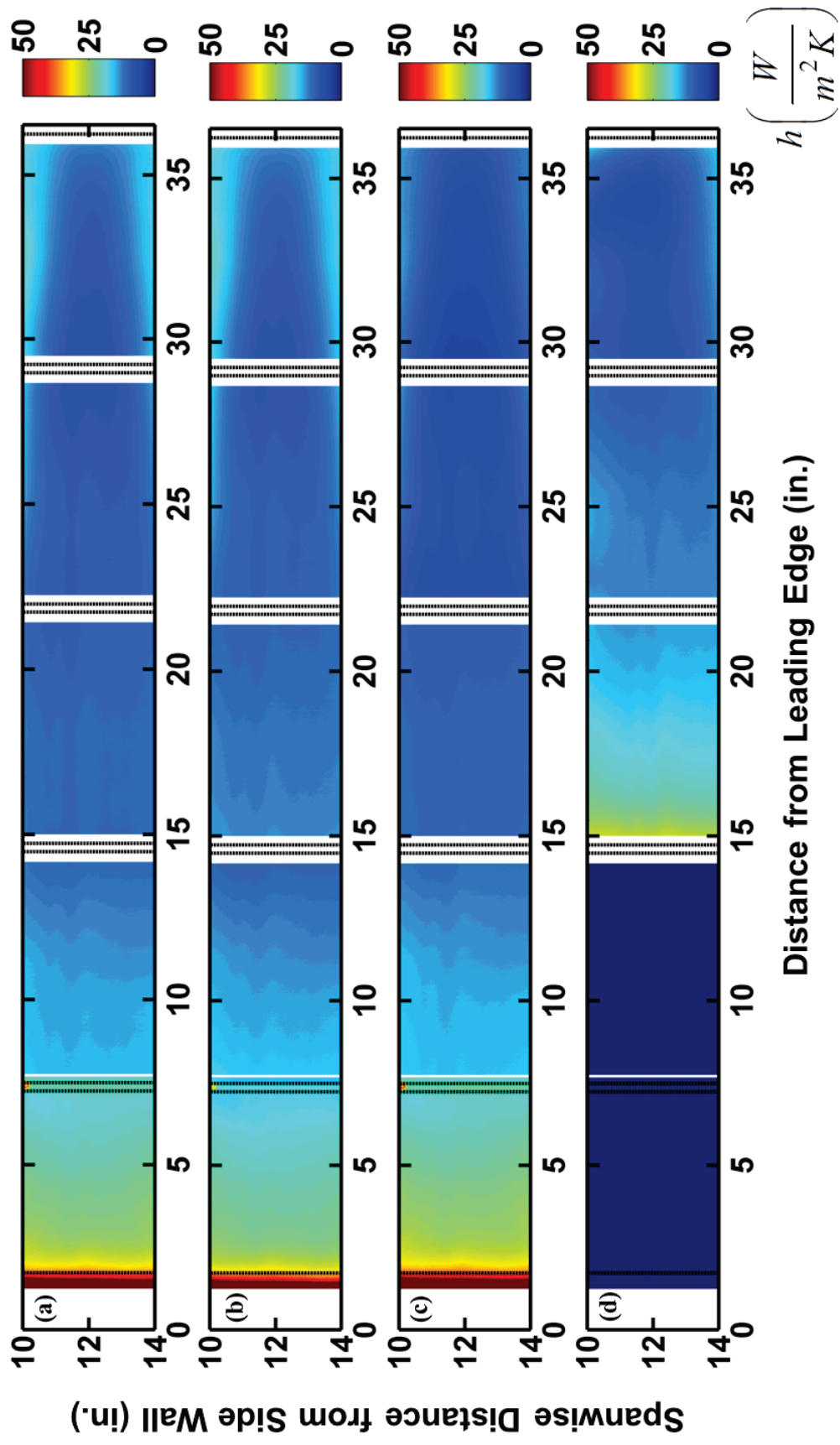


Figure 5.3: Convective heat transfer map for smooth-laminar with a) constant heat flux, b) decreasing heat flux, c) increasing heat flux, and d) unheated starting length

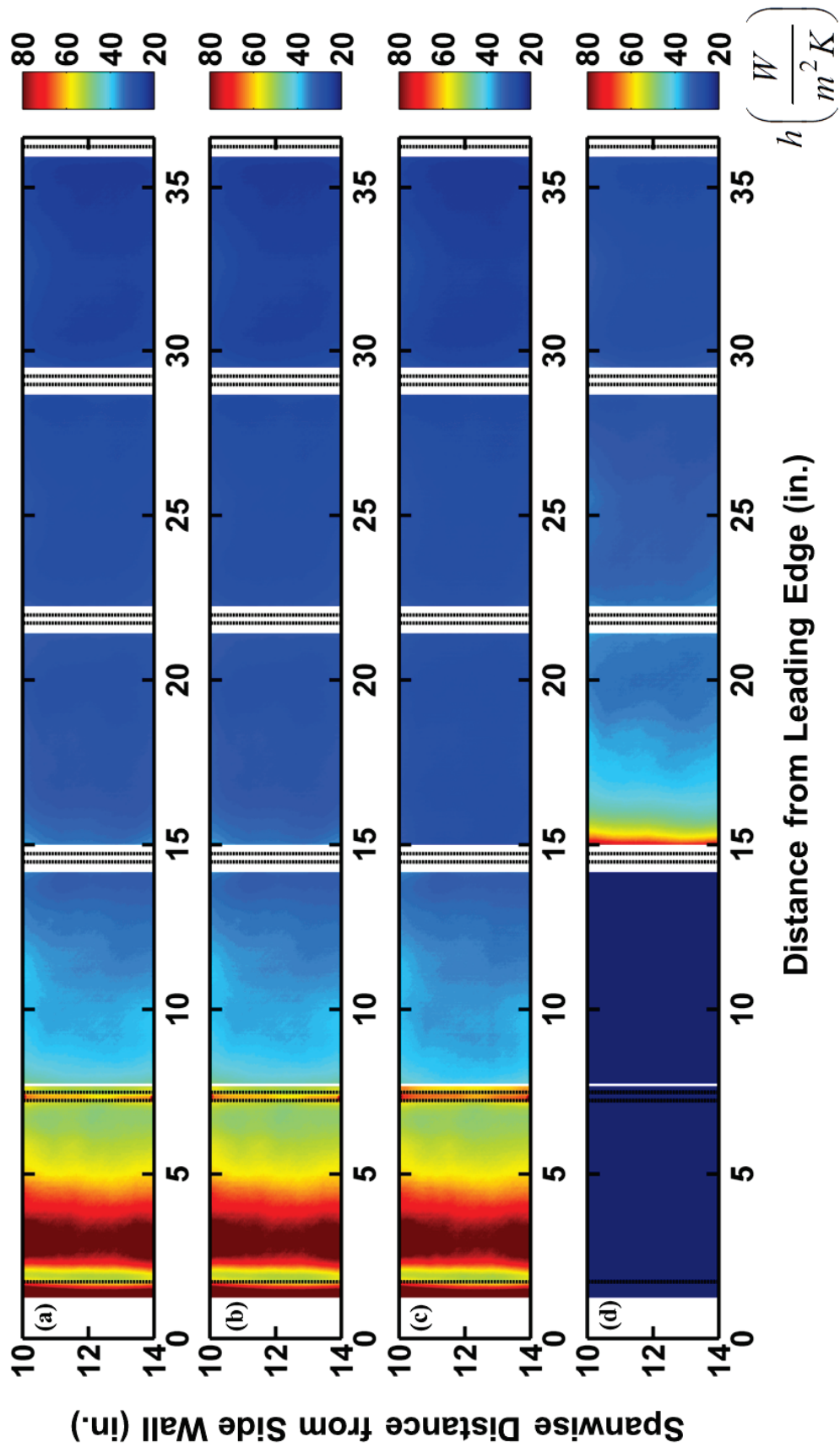


Figure 5.4: Convective heat transfer map for smooth-turbulent with a) constant heat flux, b) decreasing heat flux, c) increasing heat flux, and d) unheated starting length



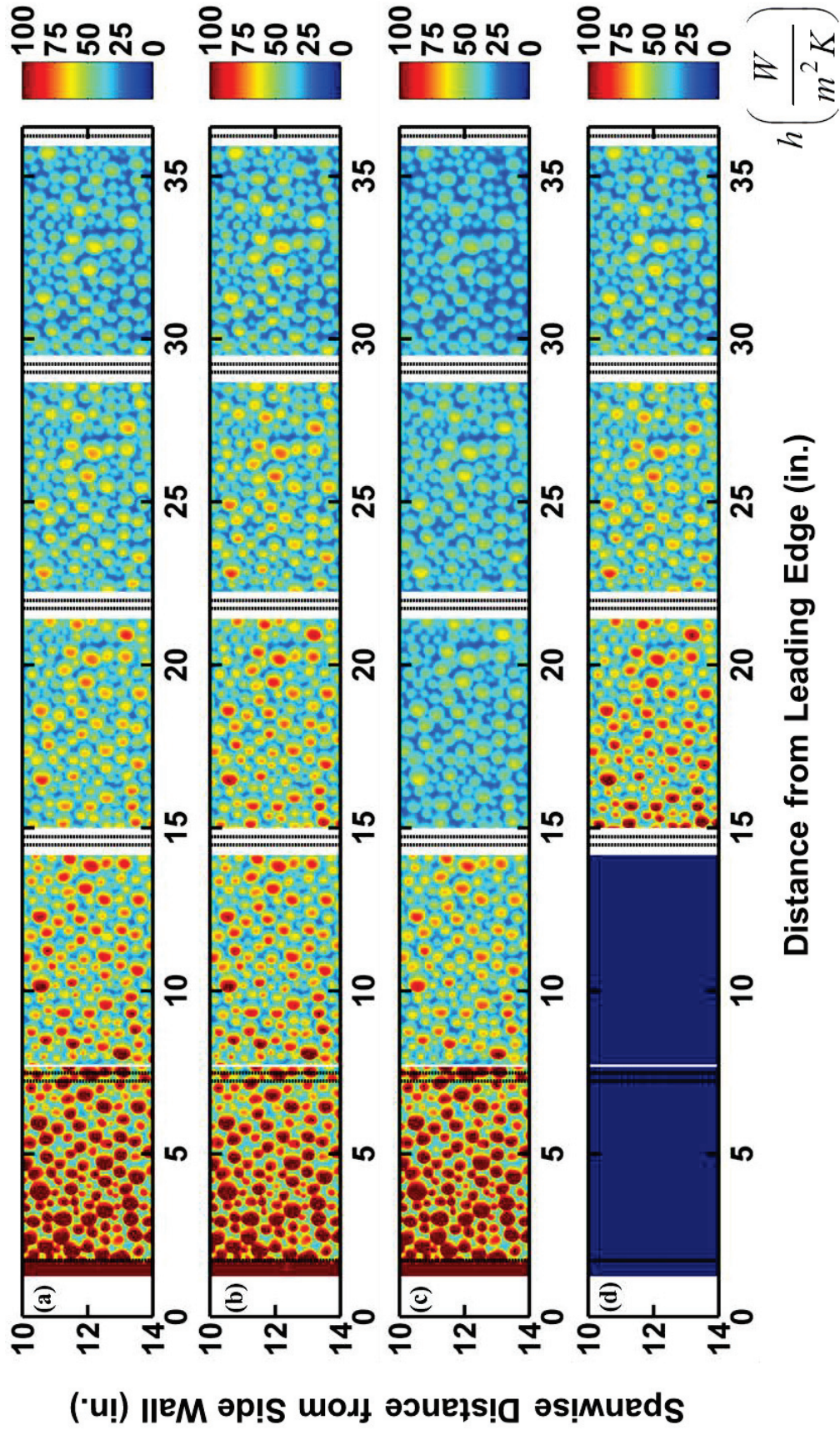


Figure 5.5: Convective heat transfer map for 052996 (Large Roughness) with a) constant heat flux, b) decreasing heat flux, c) increasing heat flux, and d) unheated starting length



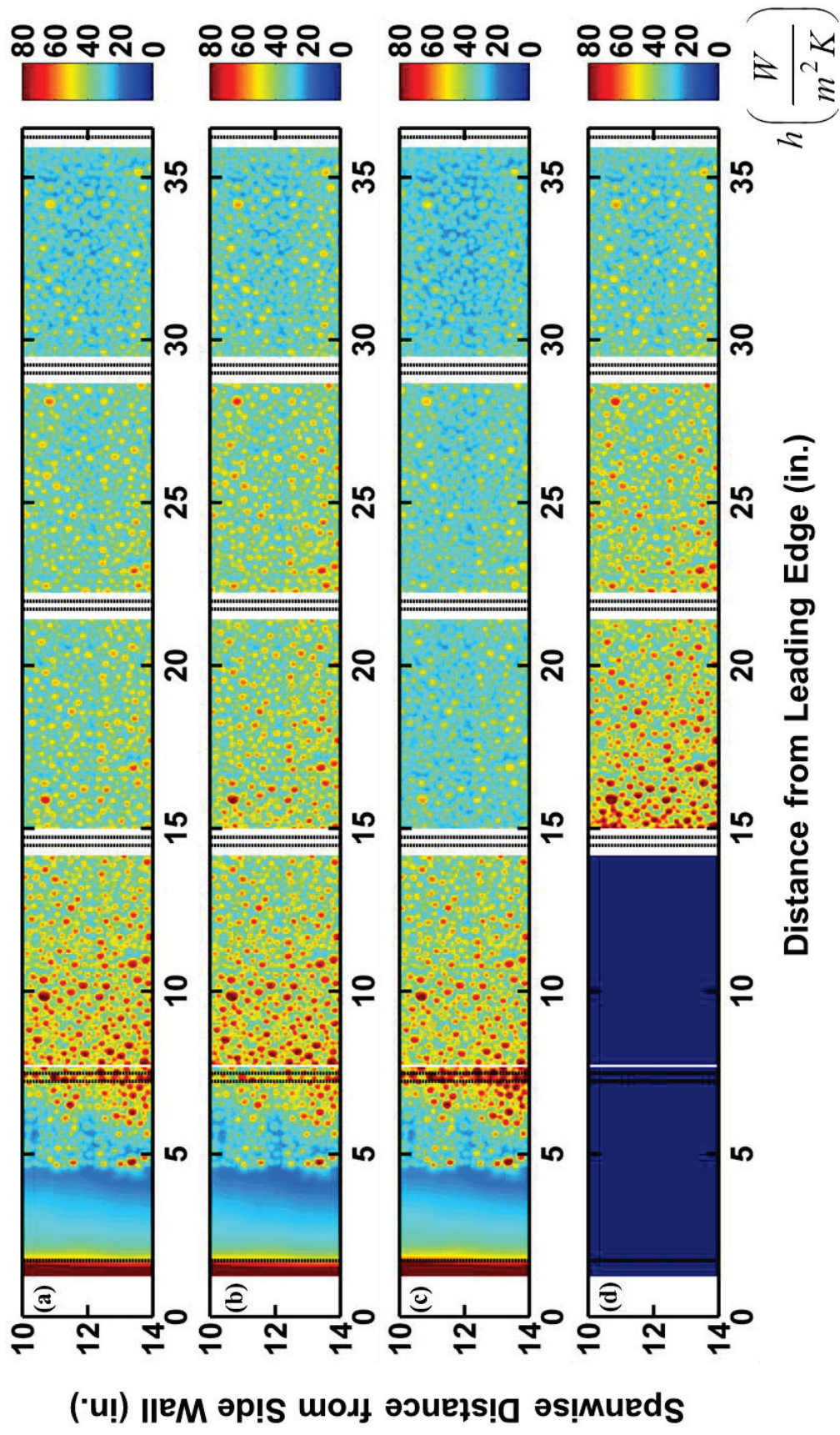


Figure 5.6: Convective heat transfer map for 053096 (Small Roughness) with a) constant heat flux, b) decreasing heat flux, c) increasing heat flux, and d) unheated starting length

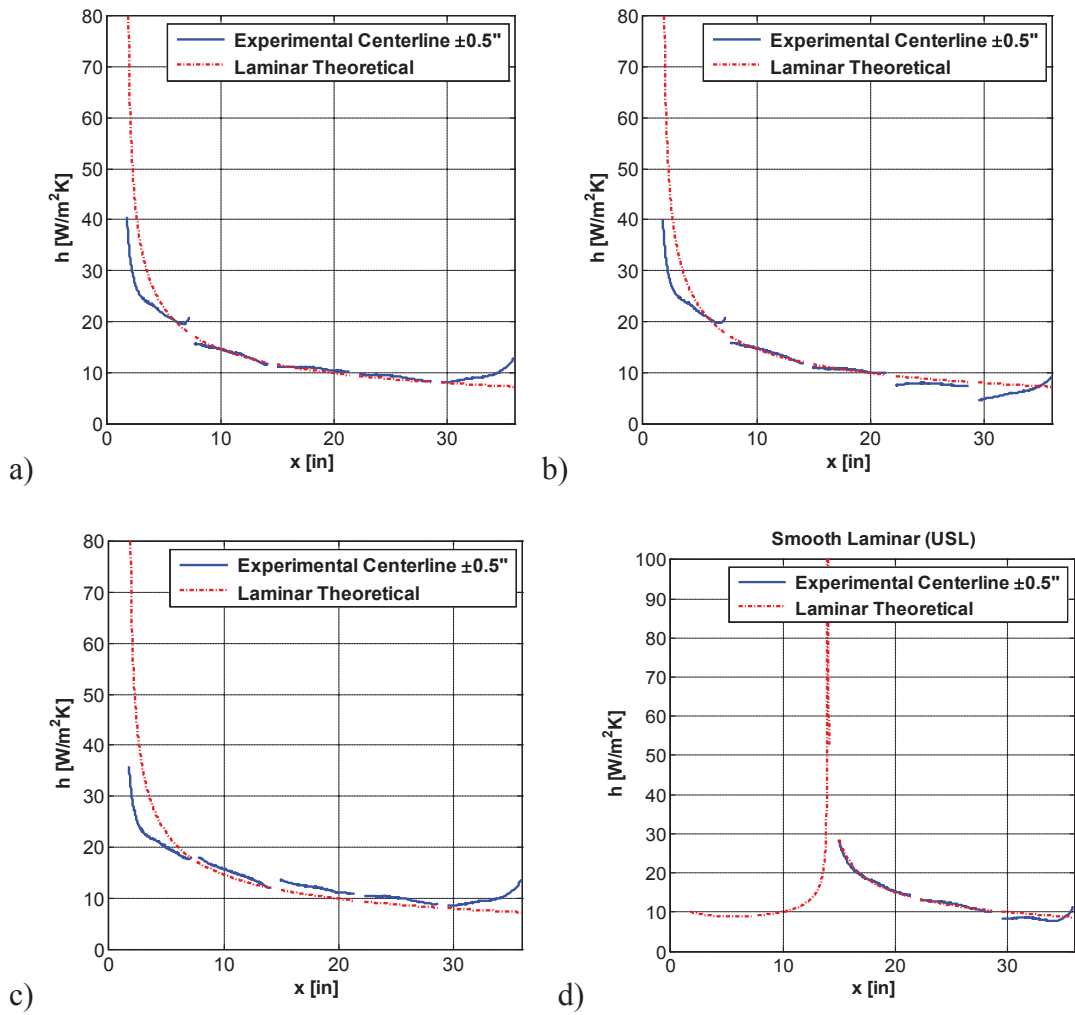


Figure 5.7: One inch lateral average along the test plate for smooth-laminar a) constant heat flux, b) decreasing heat flux, c) increasing heat flux, and d) unheated starting length

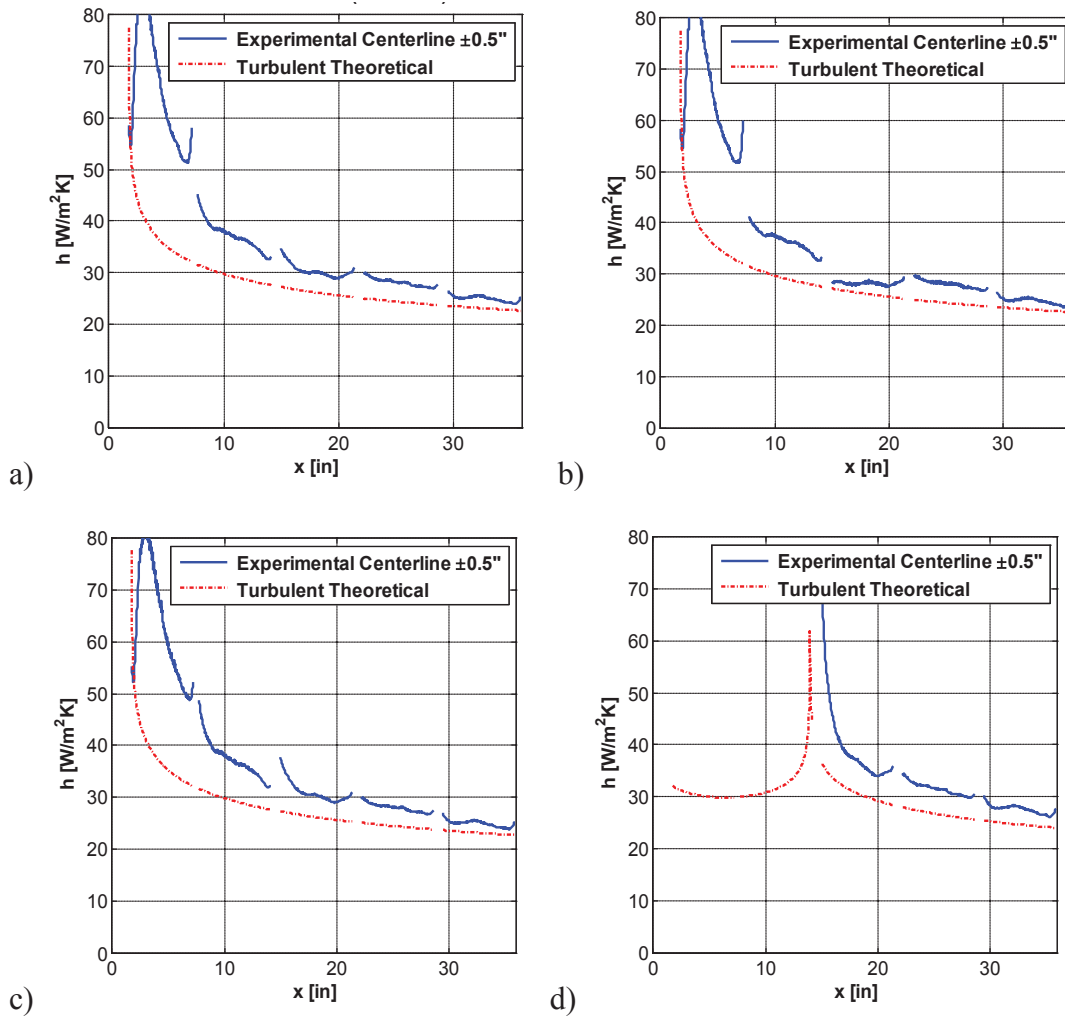


Figure 5.8: One inch lateral average along the test plate for smooth-turbulent a) constant heat flux, b) decreasing heat flux, c) increasing heat flux, and d) unheated starting length

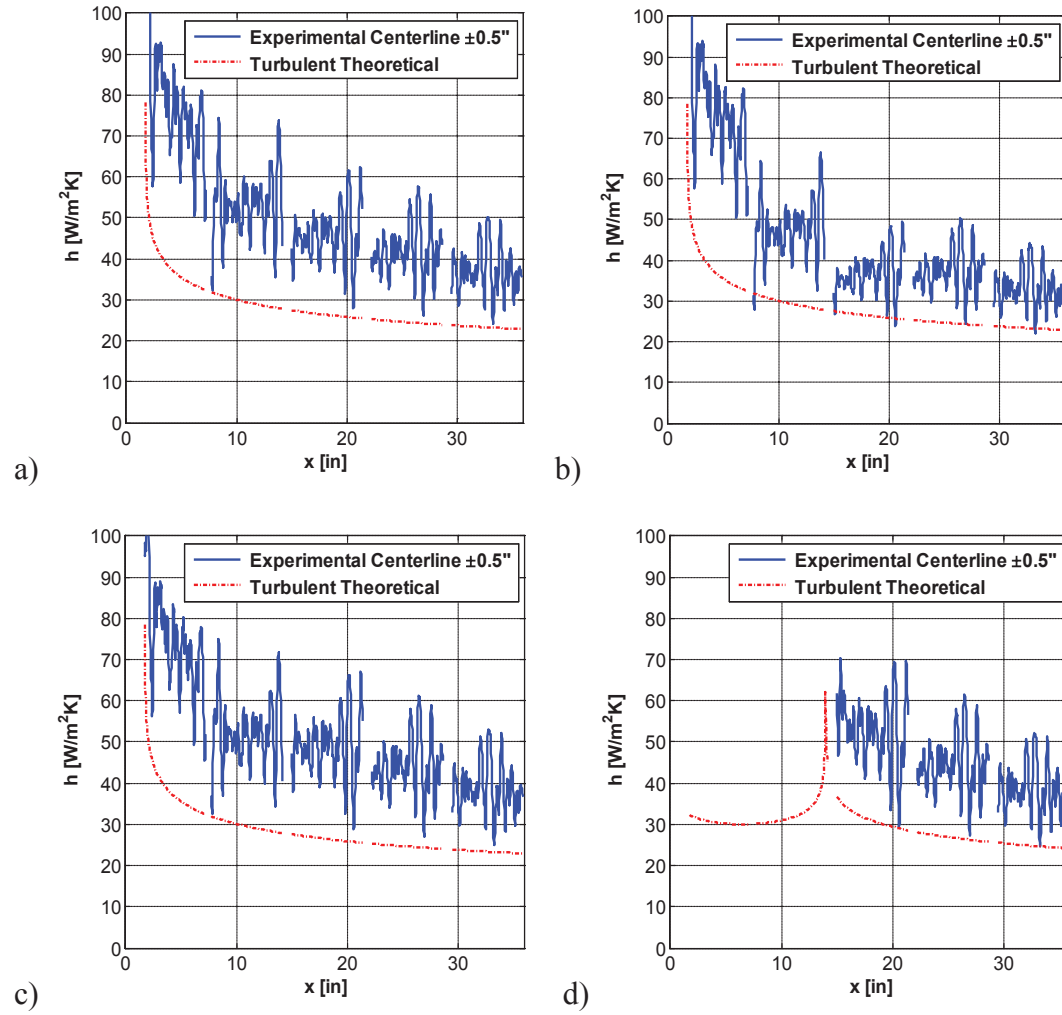


Figure 5.9: One inch lateral average along the test plate for 052996 (Large Roughness) a) constant heat flux, b) decreasing heat flux, c) increasing heat flux, and d) unheated starting length

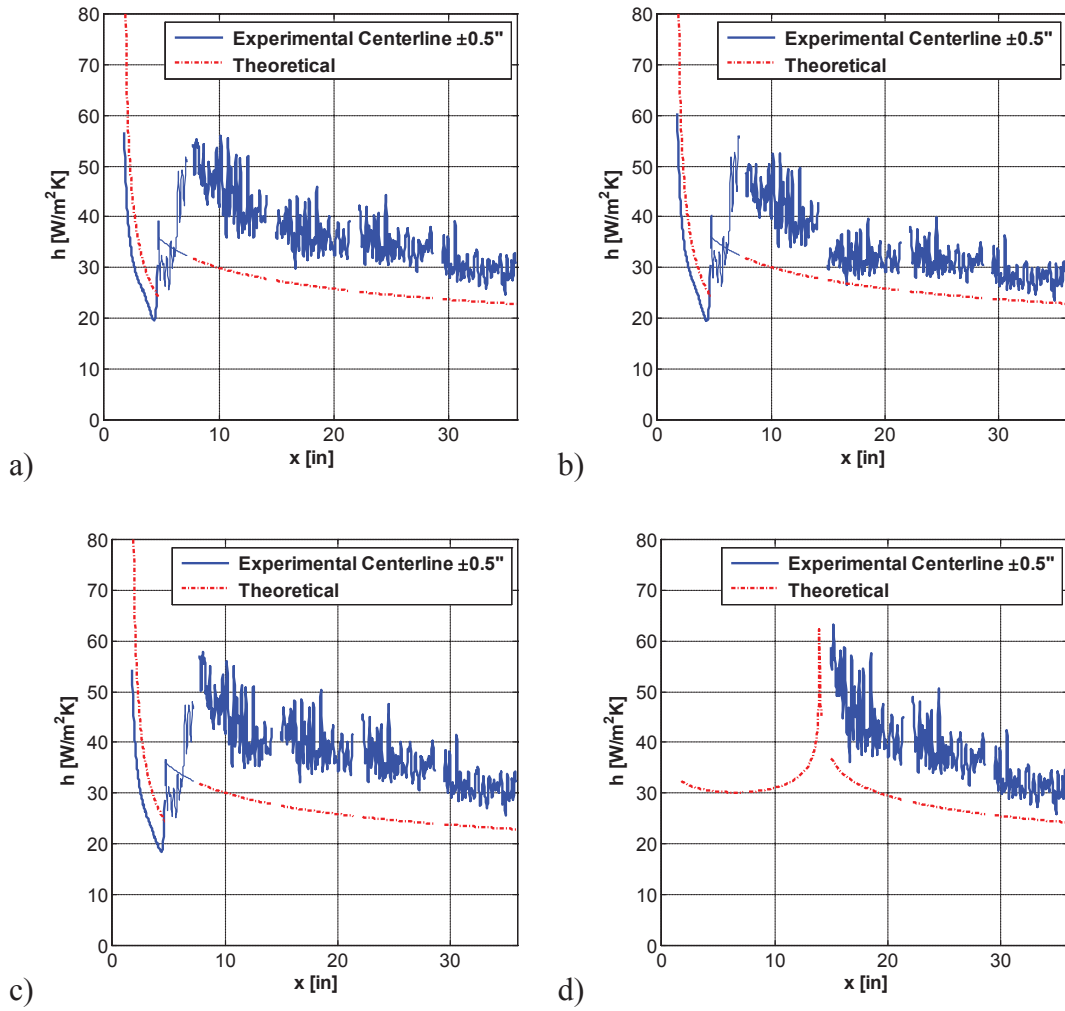


Figure 5.10: One inch lateral average along the test plate for 053096 (Small Roughness)  
a) constant heat flux, b) decreasing heat flux, c) increasing heat flux, and d) unheated starting length

The previous figures show that the overall heat transfer increases as the size of the roughness elements increases. From these Figures alone, it can be difficult to tell how variable heat flux boundary conditions affected convective heat transfer coefficients. Table 5.3 provides tabulated, Table 5.4 provides the corresponding tabulated Stanton numbers, Figures 5.12-5.15 plot the convective heat transfer coefficients for each roughness pattern, and Figures 5.16-5.19 plot the Stanton numbers as a function of Reynolds number. Reynolds number is defined by Eq. 5.1, where  $\mu$  is fluid viscosity,  $\rho$  is fluid density,  $V$  is freestream velocity, and  $x$  is the position along the test plate.

$$Re = \frac{\rho V x}{\mu}$$

The convective heat transfer coefficients were obtained by area averaging a 1'' by 1'' section at each of the thermocouple pairs along the plate. The nomenclature for these thermocouple pairs is provided in Figure 5.11. The Stanton numbers were obtained using the convective heat transfer coefficients and the Z-series air properties at the time of testing. For a complete set of test data for each case, see Tables. C.1-C.16 in Appendix C.

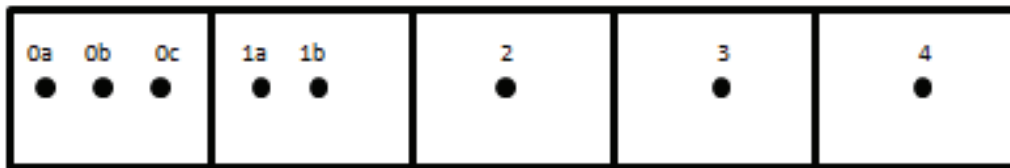


Figure 5.11: Thermocouple pair legend

Table 5.3: Convective heat transfer coefficients for each roughness pattern

Case	0a	0b	0c	1a	1b	2	3	4
Smooth-turbulent								
Constant	86.65 ± 5.16	65.99 ± 2.68	54.11 ± 1.14	40.48 ± 2.21	36.46 ± 2.07	30.15 ± 1.54	28.15 ± 1.87	25.29 ± 1.63
Decreasing	86.15 ± 5.07	65.76 ± 2.65	54.04 ± 1.15	39.59 ± 2.80	36.06 ± 2.70	28.52 ± 2.26	28.1 ± 2.94	25.08 ± 2.22
Increasing	83.85 ± 10.5	63.93 ± 6.85	52.89 ± 3.91	41.15 ± 2.94	36.3 ± 2.67	30.53 ± 1.56	28.05 ± 1.84	25.27 ± 1.53
USL						37.05 ± 2.00	31.56 ± 2.17	27.98 ± 1.17
Smooth-laminar								
Constant	26.67 ± 1.98	22.10 ± 1.87	19.70 ± 1.78	15.31 ± 0.5	13.93 ± 0.4	10.96 ± 0.83	9.27 ± 0.85	8.91 ± 0.83
Decreasing	27.03 ± 1.99	22.31 ± 1.88	19.89 ± 1.80	15.46 ± 0.5	14.1 ± 0.4	10.65 ± 0.81	7.88 ± 0.88	5.9 ± 0.91
Increasing	24.43 ± 2.01	20.50 ± 1.97	18.40 ± 1.95	16.71 ± 0.92	14.86 ± 0.75	12.06 ± 0.87	9.97 ± 0.87	9.38 ± 0.78
USL						13.46 ± 0.9	10.73 ± 0.9	8.81 ± 0.46
052996 (Large Roughness)								
Constant	81.23 ± 7.16	66.72 ± 4.06	62.32 ± 2.47	48.87 ± 2.95	48.09 ± 3.09	45 ± 3.05	40.77 ± 3.48	37.48 ± 2.93
Decreasing	81.69 ± 7.53	66.87 ± 4.32	62.63 ± 2.69	45.29 ± 3.38	44.87 ± 3.58	36.74 ± 3.7	37.02 ± 4.71	33.55 ± 3.67
Increasing	78.61 ± 12.9	64.88 ± 8.34	61.08 ± 6.38	50 ± 3.98	48.68 ± 3.97	47.81 ± 3.38	42.79 ± 3.78	39.02 ± 2.97
USL						50.13 ± 3.54	43.16 ± 3.73	38.75 ± 2.33
053096 (Small Roughness)								
Constant	27.78 ± 2.01	21.55 ± 1.88	31.40 ± 2.09	48.85 ± 2.17	44.34 ± 2.11	35.73 ± 1.91	33.57 ± 2.07	29.22 ± 1.75
Decreasing	28.21 ± 2.01	21.66 ± 1.88	32.17 ± 2.09	48.25 ± 2.71	43.46 ± 2.69	31.44 ± 2.39	30.8 ± 2.83	27.56 ± 2.18
Increasing	26.21 ± 2.04	20.53 ± 2.00	30.27 ± 1.93	50.9 ± 3.11	45.42 ± 2.9	38.49 ± 2.1	35.47 ± 2.22	30.51 ± 1.73
USL						42.66 ± 2.41	37.08 ± 2.31	30.92 ± 1.23



Table 5.4: Stanton numbers for each roughness pattern (all values have been multiplied by  $10^3$ )

Case	0a	0b	0c	1a	1b	2	3	4
Smooth-turbulent								
Constant	$11.10 \pm 0.66$	$8.45 \pm 0.34$	$6.93 \pm 0.14$	$5.18 \pm 0.28$	$4.67 \pm 0.26$	$3.86 \pm 0.20$	$3.60 \pm 0.24$	$3.24 \pm 0.21$
Decreasing	$11.04 \pm 0.65$	$8.43 \pm 0.34$	$6.92 \pm 0.15$	$5.07 \pm 0.36$	$4.62 \pm 0.35$	$3.65 \pm 0.29$	$3.60 \pm 0.38$	$3.21 \pm 0.28$
Increasing	$10.74 \pm 1.34$	$8.19 \pm 0.88$	$6.78 \pm 0.50$	$5.27 \pm 0.38$	$4.65 \pm 0.34$	$3.91 \pm 0.20$	$3.59 \pm 0.24$	$3.24 \pm 0.20$
USL						$4.75 \pm 0.26$	$4.04 \pm 0.28$	$3.59 \pm 0.15$
Smooth-laminar								
Constant	$3.51 \pm 0.26$	$2.91 \pm 0.252$	$2.59 \pm 0.232$	$2.03 \pm 0.071$	$1.84 \pm 0.051$	$1.45 \pm 0.11$	$1.23 \pm 0.11$	$1.18 \pm 0.11$
Decreasing	$3.56 \pm 0.26$	$2.94 \pm 0.252$	$2.62 \pm 0.242$	$2.05 \pm 0.071$	$1.87 \pm 0.051$	$1.41 \pm 0.11$	$1.05 \pm 0.12$	$0.78 \pm 0.12$
Increasing	$3.22 \pm 0.26$	$2.7 \pm 0.26$	$2.42 \pm 0.26$	$2.21 \pm 0.12$	$1.97 \pm 0.1$	$1.6 \pm 0.11$	$1.32 \pm 0.11$	$1.24 \pm 0.10$
USL						$1.78 \pm 0.12$	$1.42 \pm 0.12$	$1.17 \pm 0.06$
052996 (Large Roughness)								
Constant	$10.36 \pm 0.91$	$8.51 \pm 0.52$	$7.95 \pm 0.32$	$6.23 \pm 0.38$	$6.13 \pm 0.39$	$5.74 \pm 0.39$	$5.2 \pm 0.448$	$4.78 \pm 0.37$
Decreasing	$10.42 \pm 0.96$	$8.53 \pm 0.55$	$7.99 \pm 0.34$	$5.78 \pm 0.43$	$5.72 \pm 0.46$	$4.69 \pm 0.47$	$4.72 \pm 0.68$	$4.28 \pm 0.47$
Increasing	$10.02 \pm 1.64$	$8.27 \pm 1.06$	$7.79 \pm 0.81$	$6.38 \pm 0.52$	$6.21 \pm 0.51$	$6.10 \pm 0.43$	$5.46 \pm 0.48$	$4.98 \pm 0.38$
USL						$6.39 \pm 0.45$	$5.5 \pm 0.488$	$4.94 \pm 0.37$
053096 (Small Roughness)								
Constant	$3.58 \pm 0.26$	$2.77 \pm 0.24$	$4.04 \pm 0.27$	$6.29 \pm 0.28$	$5.71 \pm 0.27$	$4.6 \pm 0.25$	$4.32 \pm 0.27$	$3.76 \pm 0.23$
Decreasing	$3.63 \pm 0.26$	$2.79 \pm 0.24$	$4.14 \pm 0.27$	$6.21 \pm 0.35$	$5.59 \pm 0.35$	$4.05 \pm 0.31$	$3.96 \pm 0.36$	$3.55 \pm 0.28$
Increasing	$3.37 \pm 0.26$	$2.64 \pm 0.26$	$3.9 \pm 0.25$	$6.55 \pm 0.45$	$5.85 \pm 0.37$	$4.96 \pm 0.27$	$4.57 \pm 0.29$	$3.93 \pm 0.22$
USL						$5.49 \pm 0.31$	$4.77 \pm 0.38$	$3.98 \pm 0.16$



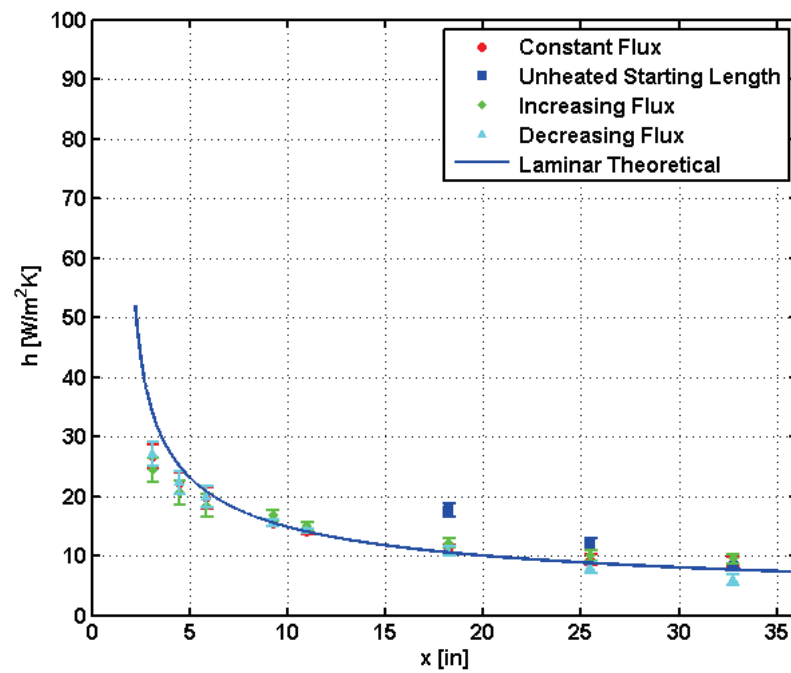


Figure 5.12: Smooth-laminar convective coefficients for varying heat flux boundary conditions

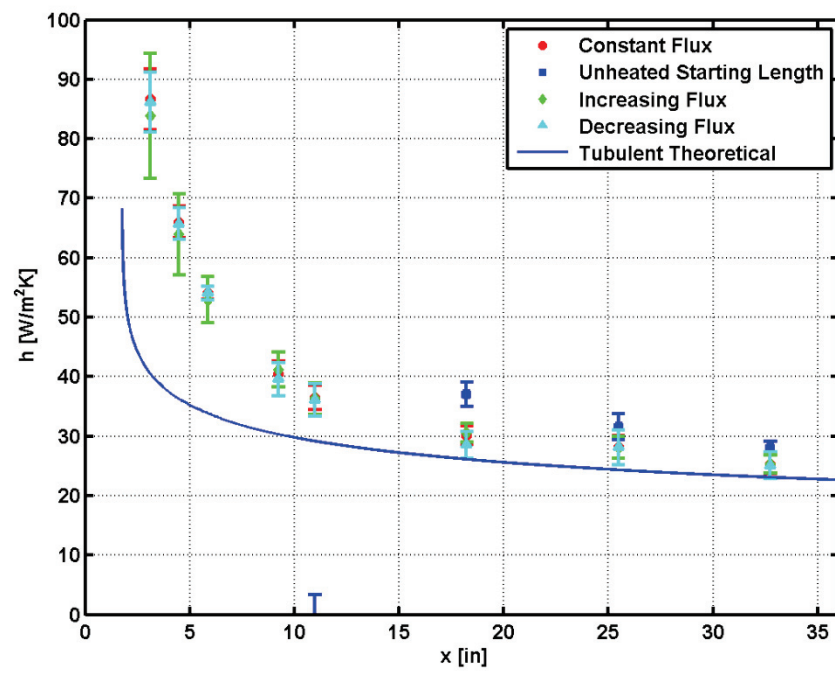


Figure 5.13: Smooth-turbulent convective coefficients for varying heat flux boundary conditions

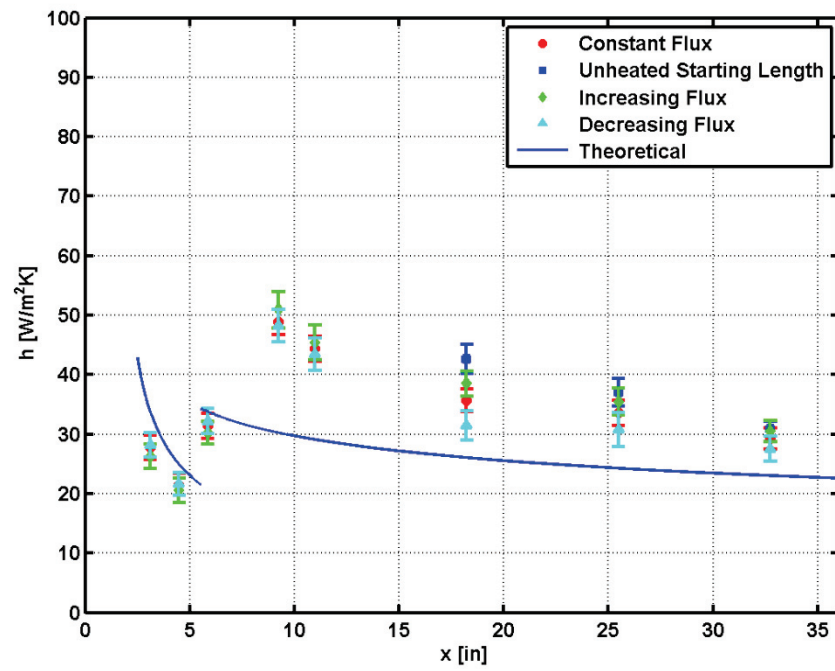


Figure 5.14: 053096 convective coefficients for varying heat flux boundary conditions

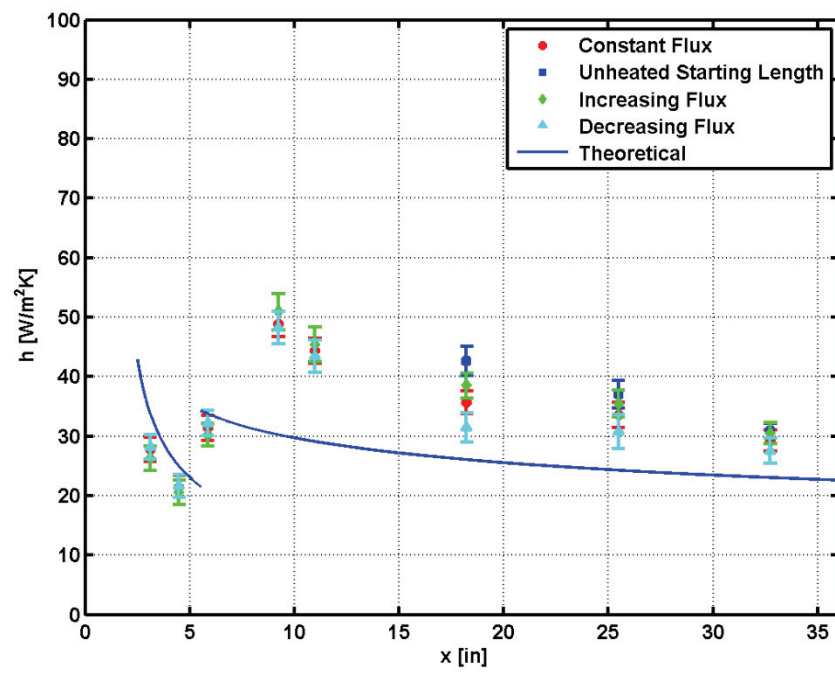


Figure 5.15: 052996 convective coefficients for varying heat flux boundary conditions

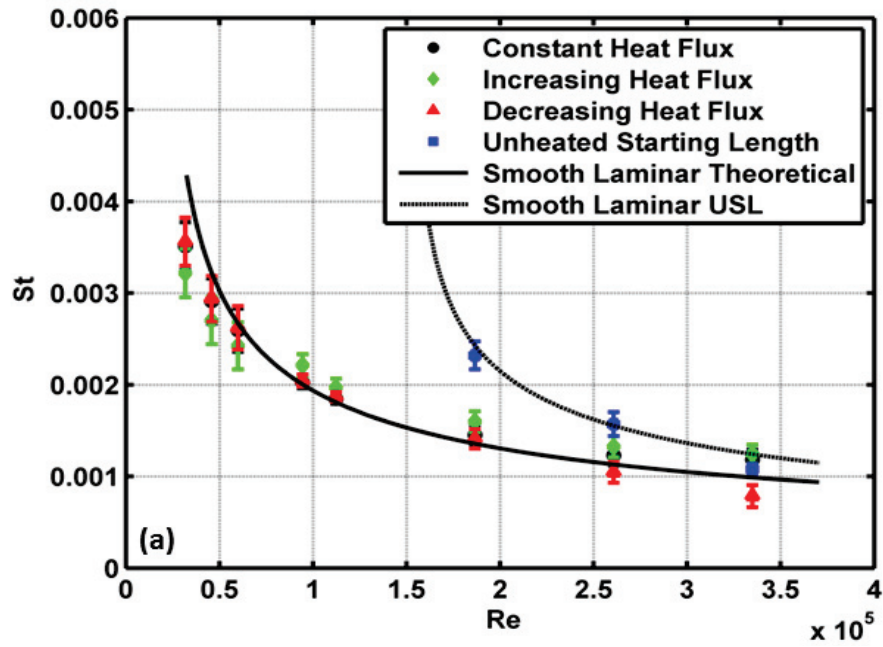


Figure 5.16: Smooth-laminar Stanton numbers for varying heat flux boundary conditions

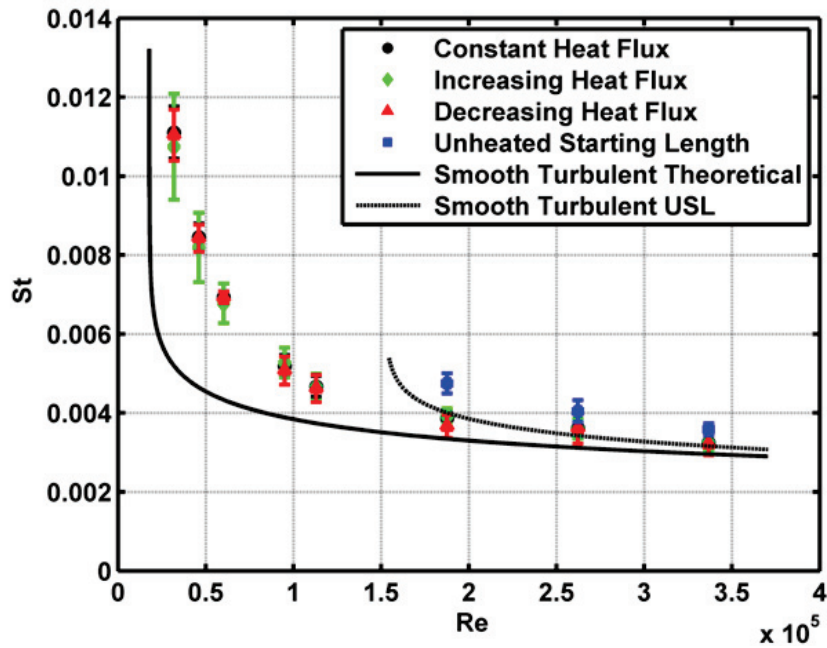


Figure 5.17: Smooth-turbulent Stanton numbers for varying heat flux boundary conditions

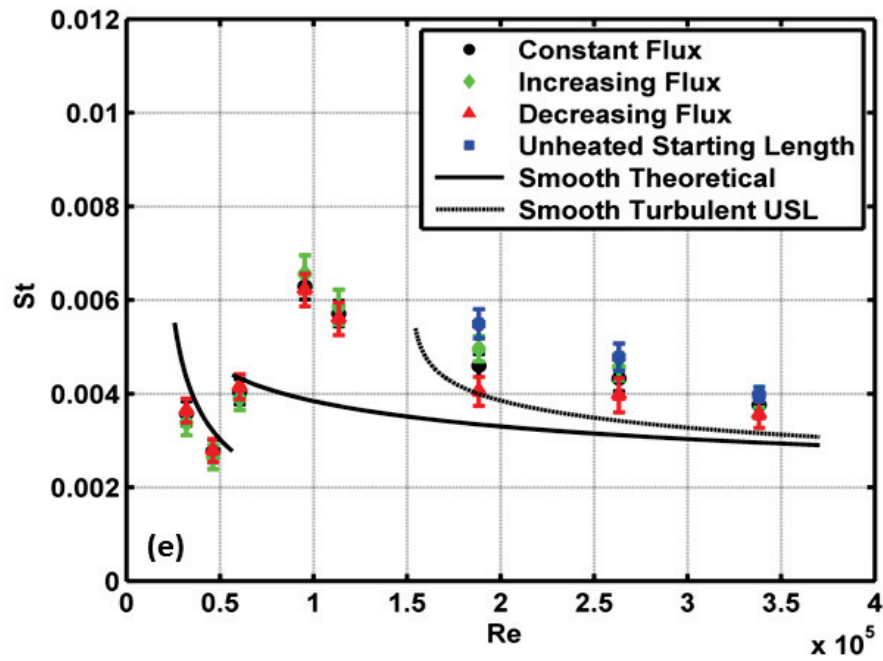


Figure 5.18: 053096 Stanton numbers for varying heat flux boundary conditions

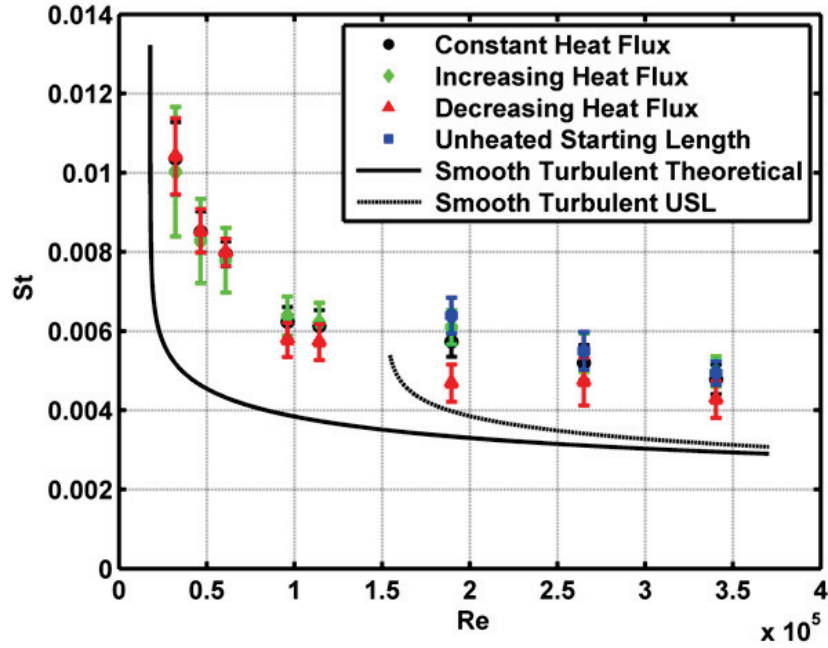


Figure 5.19: 052996 Stanton numbers for varying heat flux boundary conditions

As shown in Figures 5.12 and 5.13, the constant, decreasing, and increasing boundary conditions yield the same convective heat transfer for the smooth-turbulent and smooth-laminar roughness pattern. Little boundary condition effect can be distinguished on these roughness patterns. The unheated starting length does yield higher heat transfer, but this is due to the development difference of the viscous and thermal boundary layers.

For the 053096 roughness pattern, shown in Figure 5.14, the convection coefficients for each of the boundary conditions are more separated than in Figures 5.12 and 5.13. This is particularly true for the thermocouple pair in section two (data point group 6 from the left). When the error bars are not considered, the unheated starting length boundary condition has the highest convective heat transfer, followed by the increasing, constant, and decreasing heating schemes. However, statistically speaking only two claims can be made: 1) the decreasing case has lower heat transfer than the increasing and unheated starting length, and 2) the constant has lower heat transfer than the unheated starting length.

For the 052996 roughness pattern, shown in Figure 5.15, the convection coefficients for each of the boundary conditions are even more spread than in Figure 5.18. Again, the most distinguishability occurs in the thermocouple pair at section two. As with the 053096 roughness pattern, the unheated starting length has the highest heat transfer, followed by the increasing, constant and decreasing conditions when the error bars are not considered. But statistically, the unheated starting length, increasing, and constant schemes are the same value. It can however be said that the decreasing scheme is lower than the other schemes. In both roughness patterns, heat transfer from the

decreasing scheme is certainly lower than the heat transfer from the increasing scheme. Therefore, the heating scheme is a factor on convective heat transfer.

Note that in both roughness patterns, no boundary condition affect is apparent until section two, and the boundary condition affect slowly fades over sections three and four. In all four sets of boundary conditions sections two, three, and four were held at the same heat flux value. The only change in heat flux values were from section zero to section one, and from section one to section two. For this reason, the convection coefficient values for the variable boundary conditions move towards the values seen in the constant boundary condition over these sections. This would explain the reduced affect in those areas.

As a final note Figure 5.20 provides enhancement values for the constant flux and unheated starting length heating schemes on the rough surfaces. Enhancement is defined by Eq. 5.2, where  $h_{th}$  is the theoretical turbulent convective heat transfer coefficient for the respective heating scheme for a smooth flat plate, and  $\overline{h_o}$  is the obtained 50 x 50 pixel averaged convective heat transfer coefficient (from Figures 5.14 and 5.15).

$$Enhancement = \frac{\overline{h_o}}{h_{th}} \quad (5.2)$$

Note that because no theoretical predictions exist for increasing and decreasing heating schemes, enhancement ratios could not be provided for them.

There are two key results demonstrated by Figure 5.19. First, as shown in Tecson, enhancement for the 052996 surface is higher than the 053096 surface. Second, in both roughness patterns enhancement for the constant heat flux and unheated starting length heating schemes is statistically equal.

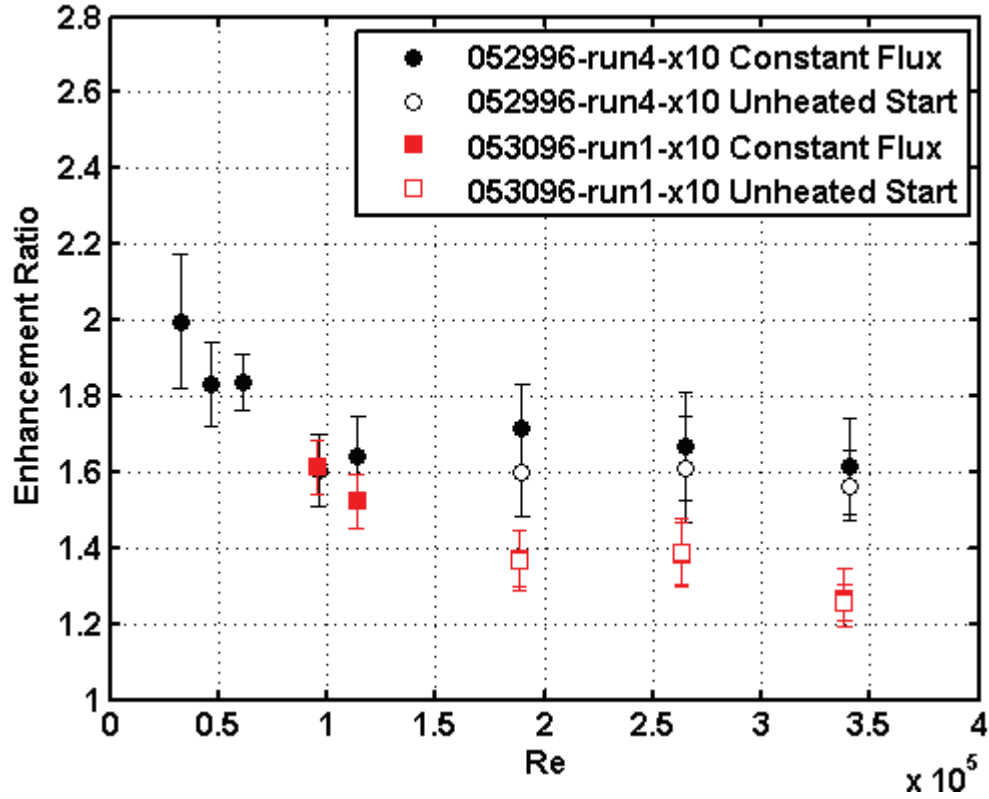


Figure 5.20: Enhancement ratio for the rough surfaces relative to the constant flux and unheated starting length smooth surface theoretical predictions

The latter result is unexpected. Because the unheated starting length boundary condition has sharper gradients in the thermal boundary layer, the fluid surrounding the roughness elements is colder. As a result, it was predicted that the unheated starting length case would have higher enhancement ratios than the constant heat flux boundary condition. They are however statistically equal, and therefore heat transfer enhancement appears to be insensitive to thermal boundary conditions.

This finding is very important in predicting heat transfer enhancements in ice accretion codes. This suggests that once enhancement is known for a roughness pattern, theoretical predictions can be developed for flat plates with variable thermal boundary

conditions. These predictions can then be used to back out convective heat transfer. Unfortunately, predicting enhancement ratios at specific locations is difficult.

*Thermal boundary layer traces.* For consistency to Tecson [5], thermal boundary layer traces were performed at the center of each test section for the decreasing, increasing, and unheated starting length cases. These traces were performed for the smooth-turbulent, 053096, and 052996 roughness patterns, but were not performed for the smooth-laminar case. Boundary layer traces for the constant heat flux case were assumed to be the same as Tecson, and were therefore not performed. The nondimensional thermal boundary layers (as defined in chapter four) have been provided in Figures 5.21-5.23, and the raw boundary layer traces can be found in Appendix D. These traces serve to characterize the thermal boundary layer along the plate.

Because convective heat transfer is effected most in section two for the rough surfaces, Figures 5.24 and 5.25 provide a comparison of the thermal boundary layer traces in section two for the 052996 and 053096 roughness patterns. As mentioned in chapter two, the slopes of the thermal boundary layer trace are related to convective heat transfer. In both Figures 5.24 and 5.25, the unheated starting length case has the biggest slope, followed by the increasing, constant, and decreasing case. This reinforces the heat transfer results from the previous section.



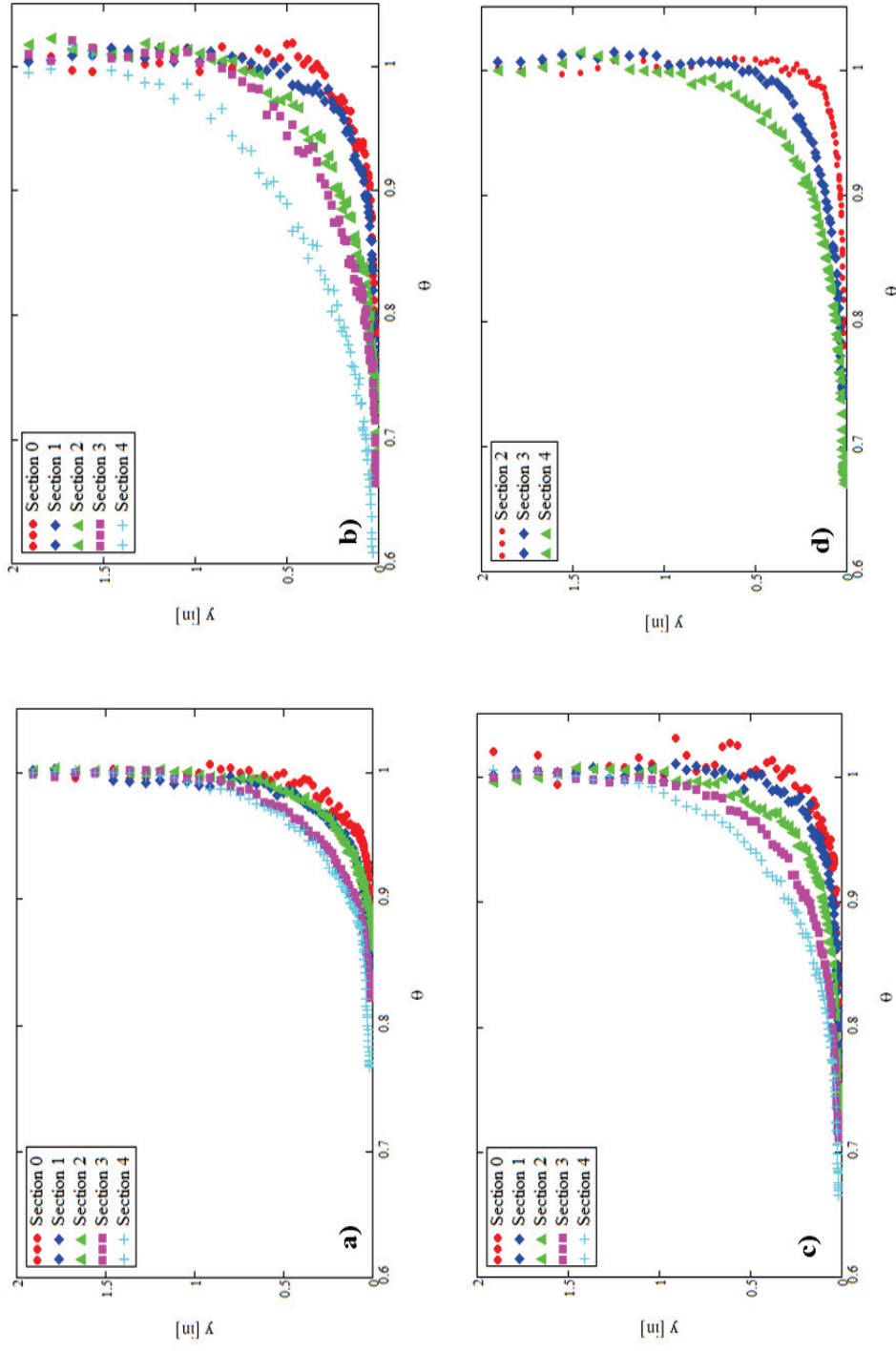


Figure 5.21: Nondimensional thermal boundary layer traces for the smooth-turbulent a) constant heat flux, b) decreasing heat flux, c) increasing heat flux, and d) unheated starting length

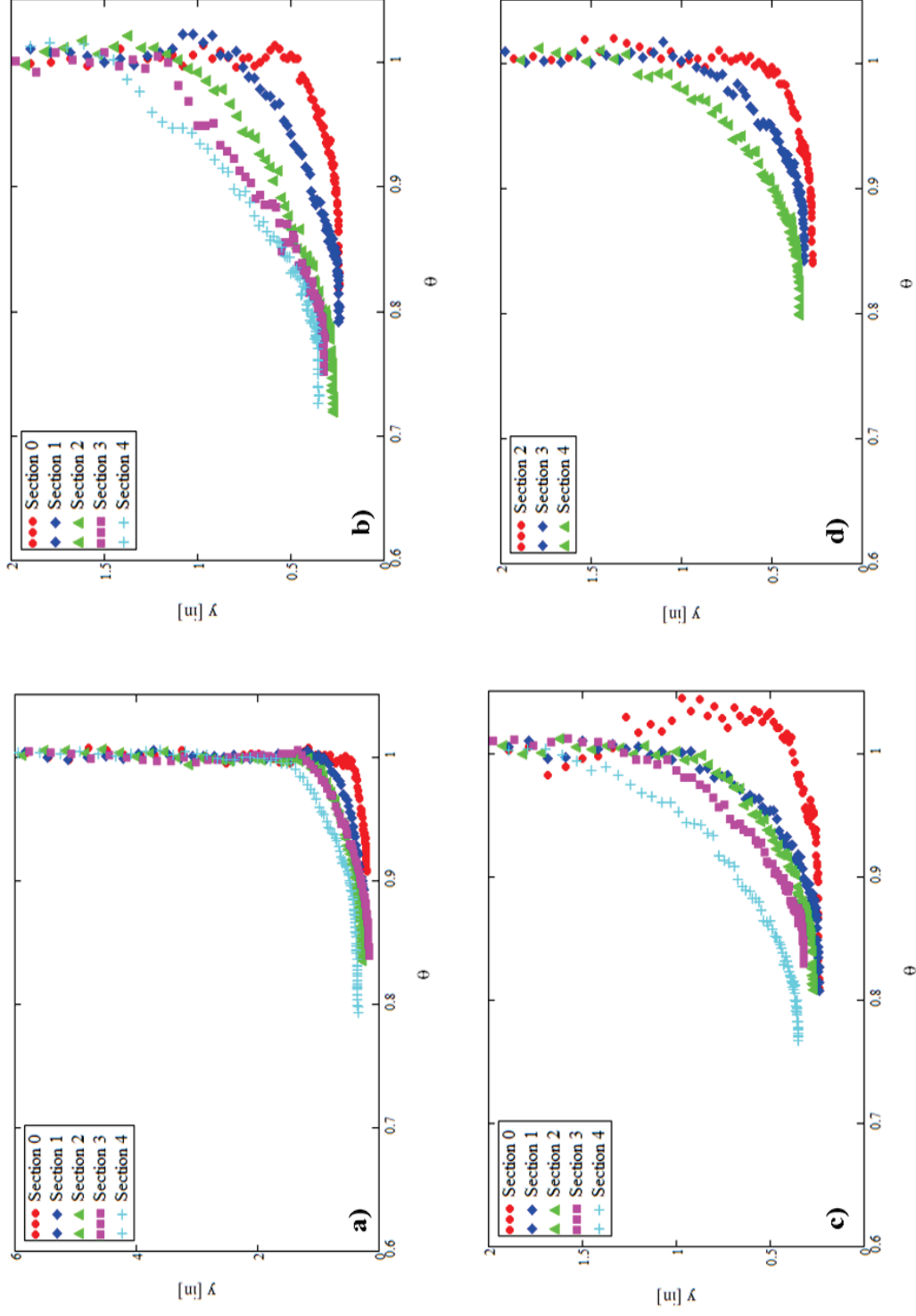


Figure 5.22: Nondimensional thermal boundary layer traces for the 052996 a) constant heat flux, b) decreasing heat flux, c) increasing heat flux, and d) unheated starting length

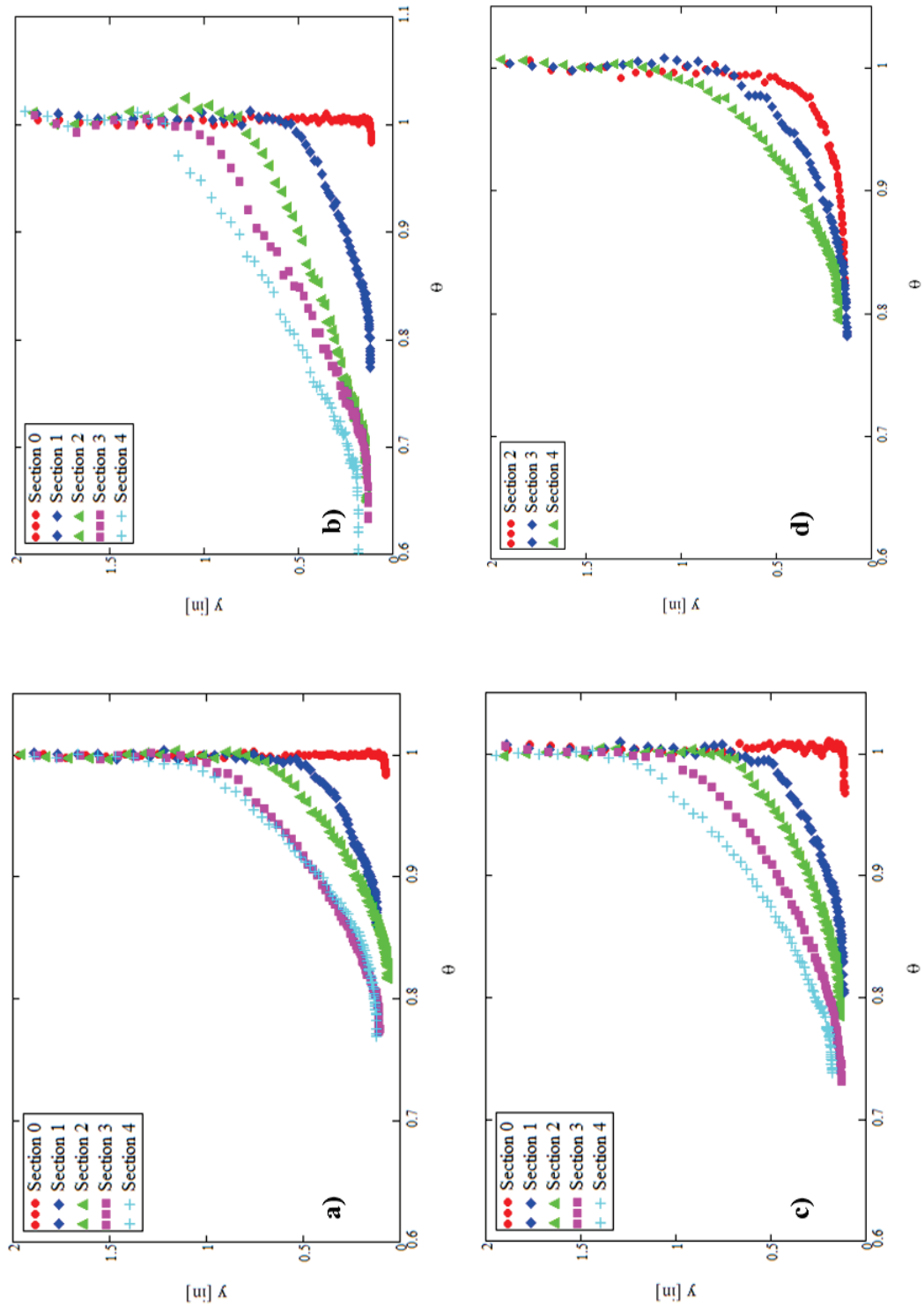


Figure 5.23: Nondimensional thermal boundary layer traces for the 053096 a) constant heat flux, b) decreasing heat flux, c) increasing heat flux, and d) unheated starting length

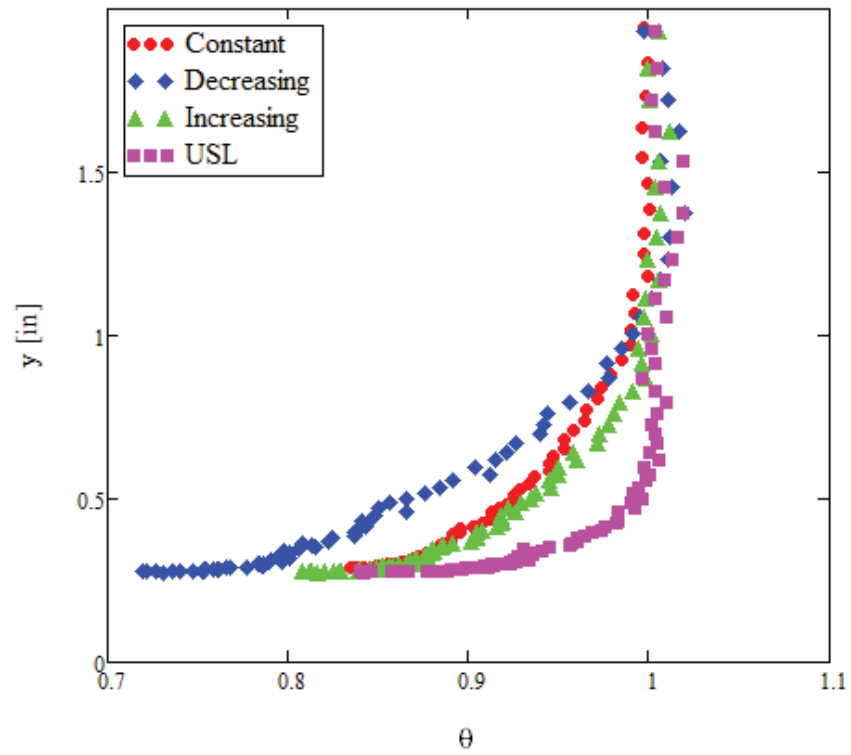


Figure 5.24: 052996 section two thermal boundary layer trace comparison

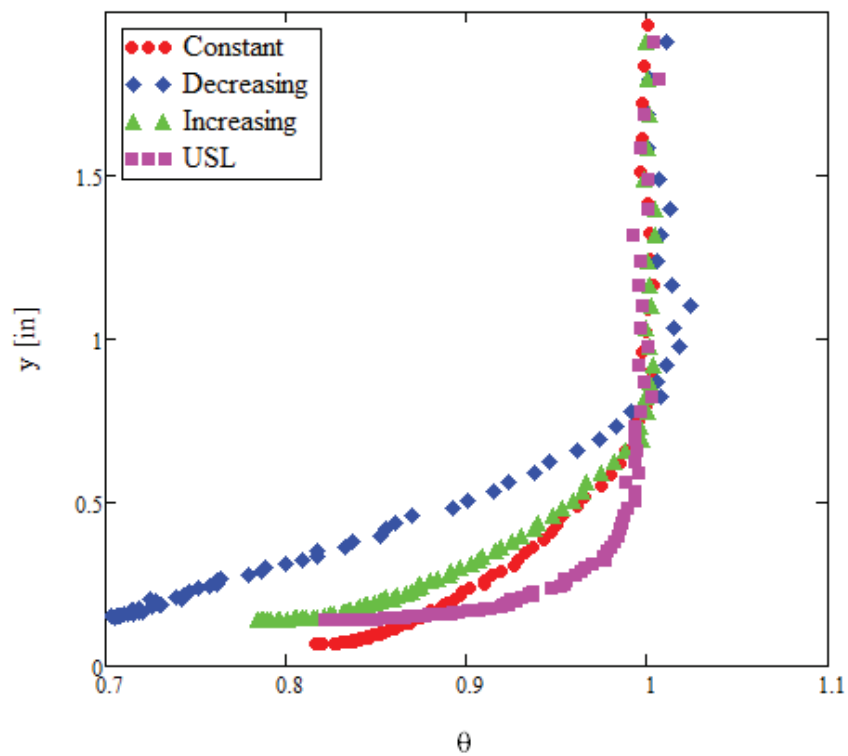


Figure 5.25: 053096 section two thermal boundary layer trace comparison

## CHAPTER SIX

### Conclusions

#### *Summary of Work*

This study investigated the effect of thermal boundary conditions on realistic ice roughness convective heat transfer, and improved upon the method used in Tecson [5]. The following changes were made to the methods used in Tecson [5].

- The IR window transmissivity was shown to be one through the transmissivity experiment.
- The thermal conductivity was more accurately measured through the thermal conductivity experiment.
- Conduction correction coefficients were introduced to benchmark raw heat transfer results to experimental results.

Variable heat flux boundary conditions were applied to the two rough surfaces created in Tecson [5], and the convective heat transfer was measured using an IR camera. The following key conclusions were drawn from the results.

- For rough surfaces, convective heat transfer is dependent on the heat flux boundary condition present. A difference was observed in the convective heat transfer between increasing and decreasing flux boundary conditions.
- As the size of the roughness elements increase, the effect of the heat flux boundary condition present increases.

- Thermal boundary conditions do not effect heat transfer enhancement relative to the smooth turbulent correlations.

### *Future Work*

Additional work will be performed using the equipment and results from this work. Because the flow field in this work is not an accelerating flow profile that would be seen on an airfoil, the convective heat transfer data obtained in this work cannot be directly applied to airfoils. An insert will be placed in the test section to create the accelerating profile seen over airfoils. This insert will map to the flow field witnessed on a NACA 0012 airfoil. However, in future studies, the insert could be modified so that convective heat transfer data could be obtained for any airfoil type.

The roughness patterns used in this work were for unswept wing ice accretion data. Similar techniques could be used to incorporate swept wing ice roughness data. Much of the procedure used in this work would be the same, but ice roughness data would be needed from the IRT, or another icing tunnel. Such a study would be useful for three-dimensional ice accretion codes.

This study only investigated heat transfer data for the roughness that occurs for initial ice accretions, but heat transfer data is also needed for a larger step in time. At larger steps in time rough horns begin to develop on top of the initial ice roughness, and there is currently not enough convective heat transfer data for these shapes. The process used in this work could be modified to rapid-prototype rough horns and investigate the heat transfer enhancement.

## APPENDICES

## APPENDIX A

### Sample Matlab Code

This Appendix provides the Matlab code used to create the temperature contour, convective heat transfer contour, and the one inch spanwise average plot. This particular code is for the smooth-turbulent unheated starting length case.

```
% Data Analysis for Smooth Plate Turbulent Test Case, Unheated Starting
% Length
% Steady state convective heat transfer test
% Written by: Logan Tecson
% Date: 12/3/12
% Edited by: Chris Walker
% Date: 4/4/2014

clear all
close all
clc

%% Constants %%%%%%%%%%%%%%%%%%%%%%%%%%%%%%%%%%%%%%%%%%%%%%%%%%%%%%%%%%%%%%%%%%%%%%%%%
% Pixel area [m^2] (0.02" x 0.02")
A_p = 2.58064e-7;
% Total heated area [m^2] (5.5in X 6.375in and 7in X 6.375in)
A_t = [0.02262092, 0.02879026, 0.02879026, 0.02879026, 0.02879026];
% Plexiglas thickness [m]
t_p = 0.018288;
% Plexiglas thermal conductivity [W/mK]
k_p = 0.205;
% Unheated started length [in]
zeta = 1.7285+7.25+5;
% Surface emissivity (flat black spray paint)
eps = 0.95;
% Stefan-Boltzman constant [W/m^2K^4]
sig = 0.0000000567;
% Conduction term correction coefficients
c_0 = 0.9;
c_1 = .9;
c_2 = 1.05;
c_3 = 1.1;
c_4 = 1.05;

%% Set up the imaging grid in real coordinates %%%%%%%%%
% Pixel to inch conversions were determined by using the screw holes
% visible in the IR images of heated section 0
IPP = 4/200; % [inch/pixel]
PPI = 200/4; % [pixel/inch]
```



```

x_ref = 305; % reference pixel (screw hole centerline)
x_span = 320; % pixel span in x-axis

% Heated section 0 x-direction grid [in]
x_0_start = 7.3535 - x_ref*IPP;
x_0_end = 7.3535 + (x_span - x_ref)*IPP;
x_0 = linspace(x_0_start, x_0_end, x_span);

% Heated section 1 x-direction grid [in]
x_1_start = 13.8535 - x_ref*IPP;
x_1_end = 13.8535 + (x_span - x_ref)*IPP;
x_1 = linspace(x_1_start, x_1_end, x_span);

% Heated section 2 x-direction grid [in]
x_2_start = 21.1035 - x_ref*IPP;
x_2_end = 21.1035 + (x_span - x_ref)*IPP;
x_2 = linspace(x_2_start, x_2_end, x_span);

% Heated section 3 x-direction grid [in]
x_3_start = 28.3535 - x_ref*IPP;
x_3_end = 28.3535 + (x_span - x_ref)*IPP;
x_3 = linspace(x_3_start, x_3_end, x_span);

% Heated section 4 x-direction grid [in]
x_4_start = 35.6035 - x_ref*IPP;
x_4_end = 35.6035 + (x_span - x_ref)*IPP;
x_4 = linspace(x_4_start, x_4_end, x_span);

y_ref = 24; % reference pixel (top screw hole centerline)
y_span = 256; % pixel span in y-axis

% Universal y-direction grid
y_start = 10 - y_ref*IPP;
y_end = 10 + (y_span - y_ref)*IPP;
y = linspace(y_start, y_end, y_span);

%% Import IR image data %%%%%%%%%%%%%%%%%%%%%%%%%%%%%%%%%%%%%%%%%%%%%%%%%%%%%%%%%%%%%%%%%%%%%%%%%%
% Images were previously analyzed and averaged using a separate MATLAB
% function. Temperatures are converted from C to K
% _Cal = calibration and _SS = steady state
% Heated section 0
Pos_0_Cal = dlmread('Pos_0_Cal.txt');
Pos_0_SS = dlmread('Pos_0_SS.txt');
Pos_0_Cal = Pos_0_Cal + 273.15;
Pos_0_SS = Pos_0_SS + 273.15;

% Heated section 1
Pos_1_Cal = dlmread('Pos_1_Cal.txt');
Pos_1_SS = dlmread('Pos_1_SS.txt');
Pos_1_Cal = Pos_1_Cal + 273.15;
Pos_1_SS = Pos_1_SS + 273.15;

% Heated section 2
Pos_2_Cal = dlmread('Pos_2_Cal.txt');

```

```

Pos_2_SS = dlmread('Pos_2_SS.txt');
Pos_2_Cal = Pos_2_Cal + 273.15;
Pos_2_SS = Pos_2_SS + 273.15;

% Heated section 3
Pos_3_Cal = dlmread('Pos_3_Cal.txt');
Pos_3_SS = dlmread('Pos_3_SS.txt');
Pos_3_Cal = Pos_3_Cal + 273.15;
Pos_3_SS = Pos_3_SS + 273.15;

% Heated section 4
Pos_4_Cal = dlmread('Pos_4_Cal.txt');
Pos_4_SS = dlmread('Pos_4_SS.txt');
Pos_4_Cal = Pos_4_Cal + 273.15;
Pos_4_SS = Pos_4_SS + 273.15;

%% Import the LABVIEW data %%%%%%%%%%%%%%%%%%%%%%%%%%%%%%%%%%%%%%%%%%%%%%%%%%%%%%%%%%%%%%%%%%%%%%%%%%
% Raw data from LABVIEW generated text file
rawdata = importdata('081613.txt');
% Indices where calibration images were taken for each heated section
Cal_ind = [76 85 91 96 101];
% Indices where steady state images were taken for each section
SS_ind = [1384 1388 1392 1396 1400];

% Break rawdata into the calibration and steady state data only and
% write to text file for use in Mathcad
avg_data = [rawdata(Cal_ind,:) ; rawdata(SS_ind,:)];

% Column indices with power data for each heated section
E_ind = [36, 37, 38, 39]; % voltage
I_ind = [40, 41, 42, 43]; % current

% Extract voltage for sections 0-3 at steady state [V]
for i = 1:4
    E(i) = avg_data(i+5, E_ind(i));
end
E(5) = 6.009; % Manually input voltage for section 4

% Extract current for sections 0-3 at steady state [A]
for i = 1:4
    I(i) = avg_data(i+5, I_ind(i))-rawdata(1,I_ind(i));
end
I(1) = I(1)*2; % Apply current transducer factor for section 0
I(5) = 2.679; % Manually input current for section 4

% Inlet air pressure
P = avg_data(:,53); % [Pa]

% Inlet air relative humidity
RH = avg_data(:,54); % [%]

%% Thermocouple values at calibration %%%%%%%%%%%%%%%%%%%%%%%%%%%%%%%%%%%%%%%%%%%%%%%%%%%%%%%%%%%%%%%%%%%%%%%%%%
% Convert the j type values back to raw voltages, and convert those
% voltages to k type values
for i = 1:10

```

```

    for j = 2:18
        avg_data(i,j) = Temp_Conversion_Final2(avg_data(i,j));
    end
end

% Subsurface and underplate TCs, converted to K
TC0_Cal = avg_data(1,2) + 273.15;    TC8_Cal = avg_data(1,10) + 273.15;
TC1_Cal = avg_data(1,3) + 273.15;    TC9_Cal = avg_data(1,11) + 273.15;
TC2_Cal = avg_data(1,4) + 273.15;    TC10_Cal = avg_data(1,12) + 273.15;
TC3_Cal = avg_data(2,5) + 273.15;    TC11_Cal = avg_data(2,13) + 273.15;
TC4_Cal = avg_data(2,6) + 273.15;    TC12_Cal = avg_data(2,14) + 273.15;
TC5_Cal = avg_data(3,7) + 273.15;    TC13_Cal = avg_data(3,15) + 273.15;
TC6_Cal = avg_data(4,8) + 273.15;    TC14_Cal = avg_data(4,16) + 273.15;
TC7_Cal = avg_data(5,9) + 273.15;    TC15_Cal = avg_data(5,17) + 273.15;

% Freestream TCs, converted to K
FS_0_Cal = avg_data(1,52) + 273.15;
FS_1_Cal = avg_data(2,52) + 273.15;
FS_2_Cal = avg_data(3,52) + 273.15;
FS_3_Cal = avg_data(4,52) + 273.15;
FS_4_Cal = avg_data(5,52) + 273.15;

% Average freestream temperature (for TC calibration)
FS_Cal_Avg = (FS_0_Cal + FS_1_Cal + FS_2_Cal + FS_3_Cal + FS_4_Cal)/5;

%% Thermocouple values at steady state %%%%%%%%%%%%%%%%%%%%%%%%%%%%%%%%%%%%%%%%%%%%%%%%%%%%%%%%%%%%%%%%%%%%%%%%%
% Subsurface and underplate TCs, converted to K
TC0_SS = avg_data(6,2) + 273.15;    TC8_SS = avg_data(6,10) + 273.15;
TC1_SS = avg_data(6,3) + 273.15;    TC9_SS = avg_data(6,11) + 273.15;
TC2_SS = avg_data(6,4) + 273.15;    TC10_SS = avg_data(6,12) + 273.15;
TC3_SS = avg_data(7,5) + 273.15;    TC11_SS = avg_data(7,13) + 273.15;
TC4_SS = avg_data(7,6) + 273.15;    TC12_SS = avg_data(7,14) + 273.15;
TC5_SS = avg_data(8,7) + 273.15;    TC13_SS = avg_data(8,15) + 273.15;
TC6_SS = avg_data(9,8) + 273.15;    TC14_SS = avg_data(9,16) + 273.15;
TC7_SS = avg_data(10,9) + 273.15;    TC15_SS = avg_data(10,17) + 273.15;

% Freestream TCs, converted to K
FS_0_SS = avg_data(6,52) + 273.15;
FS_1_SS = avg_data(7,52) + 273.15;
FS_2_SS = avg_data(8,52) + 273.15;
FS_3_SS = avg_data(9,52) + 273.15;
FS_4_SS = avg_data(10,52) + 273.15;

%Average of the center 50x50 pixels of each IR window for calibration
Pos_0_SS_calibration = mean(mean(Pos_0_Cal(103:153,135:185)));
Pos_1_SS_calibration = mean(mean(Pos_1_Cal(103:153,135:185)));
Pos_2_SS_calibration = mean(mean(Pos_2_Cal(103:153,135:185)));
Pos_3_SS_calibration = mean(mean(Pos_3_Cal(103:153,135:185)));
Pos_4_SS_calibration = mean(mean(Pos_4_Cal(103:153,135:185)));

%% Corrected thermocouple steady state values %%%%%%%%%%%%%%%%%%%%%%%%%%%%%%%%%%%%%%%%%%%%%%%%%%%%%%%%%%%%%%%%%%%%%%%%%
% Heated section 0 TCs
TC0_Cor = TC0_SS - (TC0_Cal - Pos_0_SS_calibration);
TC8_Cor = TC8_SS - (TC8_Cal - Pos_0_SS_calibration);
TC1_Cor = TC1_SS - (TC1_Cal - Pos_0_SS_calibration);

```

```

TC9_Cor = TC9_SS - (TC9_Cal - Pos_0_SS_calibration);
TC2_Cor = TC2_SS - (TC2_Cal - Pos_0_SS_calibration);
TC10_Cor = TC10_SS - (TC10_Cal - Pos_0_SS_calibration);
FS_0_Cor = FS_0_SS - (FS_0_Cal - Pos_0_SS_calibration);

% Heated section 1 TCs
TC3_Cor = TC3_SS - (TC3_Cal - Pos_1_SS_calibration);
TC11_Cor = TC11_SS - (TC11_Cal - Pos_1_SS_calibration);
TC4_Cor = TC4_SS - (TC4_Cal - Pos_1_SS_calibration);
TC12_Cor = TC12_SS - (TC12_Cal - Pos_1_SS_calibration);
FS_1_Cor = FS_1_SS - (FS_1_Cal - Pos_1_SS_calibration);

% Heated section 2 TCs
TC5_Cor = TC5_SS - (TC5_Cal - Pos_2_SS_calibration);
TC13_Cor = TC13_SS - (TC13_Cal - Pos_2_SS_calibration);
FS_2_Cor = FS_2_SS - (FS_2_Cal - Pos_2_SS_calibration);

% Heated section 3 TCs
TC6_Cor = TC6_SS - (TC6_Cal - Pos_3_SS_calibration);
TC14_Cor = TC14_SS - (TC14_Cal - Pos_3_SS_calibration);
FS_3_Cor = FS_3_SS - (FS_3_Cal - Pos_3_SS_calibration);

% Heated section 4 TCs
TC7_Cor = TC7_SS - (TC7_Cal - Pos_4_SS_calibration);
TC15_Cor = TC15_SS - (TC15_Cal - Pos_4_SS_calibration);
FS_4_Cor = FS_4_SS - (FS_4_Cal - Pos_4_SS_calibration);

%% No longer correct IR temperatures for transmissivity
%%%%%%%%%%%%%%%%%%%%%%%%%%%%%%%%%%%%%%%%%%%%%%%%%%%%%%%%%%%%%%%%%%%%%%%%
% Because temperatures are calibrated to the IR camera, these values
remain
% unchanged
Pos_0_Cor = Pos_0_SS;
Pos_1_Cor = Pos_1_SS;
Pos_2_Cor = Pos_2_SS;
Pos_3_Cor = Pos_3_SS;
Pos_4_Cor = Pos_4_SS;

%% Calculate air properties %%%%%%%%%%%%%%%%%%%%%%%%%%%%%%%%%%%%%%%%%%%%%%%%%%%%%%%%%%%%%%%%%%%%%%%%%
% Average freestream properties
T_inf = (FS_0_Cor + FS_1_Cor + FS_2_Cor + FS_3_Cor + FS_4_Cor)/5; % [K]
P_inf = mean(P(6:10)); % [Pa]
RH_inf = mean(RH(6:10)); % [%]
U_inf = avg_data(6,57); % [m/s]

% Use the freestream properties above in MathCAD to get air properties
rho_air = 1.1621; % density [kg/m^3]
mu_air = 1.9017*10^-5; % viscosity [kg/ms]
k_air = 0.0258; % thermal conductivity [(m*kg)/(K*s^3)]
Pr_air = 0.7468; % Prandtl number

%% Experimental local convective heat transfer coefficients %%%%%%%%%
%Use the average corrected freestream in the calculations
FS_avg = (FS_0_Cor+FS_1_Cor+FS_2_Cor+FS_3_Cor+FS_4_Cor)/5;

```

```

h_0 = -1+0*(E(1)*I(1)/A_t(1) - c_0*k_p/t_p*(1/3*(TC0_Cor-
TC8_Cor)+1/3*(TC1_Cor-TC9_Cor)+1/3*(TC2_Cor-TC10_Cor)) -
sig*eps*(Pos_0_Cor.^4 - FS_avg^4)).*(Pos_0_Cor - FS_avg).^(-1);
h_1 = -1+0*(E(2)*I(2)/A_t(2) - c_1*k_p/t_p*((0.25*(TC3_Cor-
TC11_Cor)+0.75*(TC4_Cor - TC12_Cor))) - sig*eps*(Pos_1_Cor.^4 -
FS_avg^4)).*(Pos_1_Cor - FS_avg).^(-1);
h_2 = (E(3)*I(3)/A_t(3) - c_2*k_p/t_p*(TC5_Cor - TC13_Cor) -
sig*eps*(Pos_2_Cor.^4 - FS_avg^4)).*(Pos_2_Cor - FS_avg).^(-1);
h_3 = (E(4)*I(4)/A_t(4) - c_3*k_p/t_p*(TC6_Cor - TC14_Cor) -
sig*eps*(Pos_3_Cor.^4 - FS_avg^4)).*(Pos_3_Cor - FS_avg).^(-1);
h_4 = (E(5)*I(5)/A_t(5) - c_4*k_p/t_p*(TC7_Cor - TC15_Cor) -
sig*eps*(Pos_4_Cor.^4 - FS_avg^4)).*(Pos_4_Cor - FS_avg).^(-1);

% Spanwise average values along the centerline +/- 0.5"
for i = 1:320
    h_0_avg(i) = sum(h_0(100:149,i))/50;
end

for i = 1:320
    h_1_avg(i) = sum(h_1(100:149,i))/50;
end

for i = 1:320
    h_2_avg(i) = sum(h_2(100:149,i))/50;
end

for i = 1:320
    h_3_avg(i) = sum(h_3(100:149,i))/50;
end

for i = 1:320
    h_4_avg(i) = sum(h_4(100:149,i))/50;
end

%% Theoretical heat transfer coefficients from turbulent correlation %%
h_lam_0 =
0.0308.*((U_inf*x_0*0.0254*rho_air)./mu_air).^(4/5).*(Pr_air)^(1/3).*k_
air.*(x_0*0.0254).^(-1).*(1-(zeta./x_0).^(9/10)).^(-1/9);
h_lam_1 =
0.0308.*((U_inf*x_1*0.0254*rho_air)./mu_air).^(4/5).*(Pr_air)^(1/3).*k_
air.*(x_1*0.0254).^(-1).*(1-(zeta./x_1).^(9/10)).^(-1/9);
h_lam_2 =
0.0308.*((U_inf*x_2*0.0254*rho_air)./mu_air).^(4/5).*(Pr_air)^(1/3).*k_
air.*(x_2*0.0254).^(-1).*(1-(zeta./x_2).^(9/10)).^(-1/9);
h_lam_3 =
0.0308.*((U_inf*x_3*0.0254*rho_air)./mu_air).^(4/5).*(Pr_air)^(1/3).*k_
air.*(x_3*0.0254).^(-1).*(1-(zeta./x_3).^(9/10)).^(-1/9);
h_lam_4 =
0.0308.*((U_inf*x_4*0.0254*rho_air)./mu_air).^(4/5).*(Pr_air)^(1/3).*k_
air.*(x_4*0.0254).^(-1).*(1-(zeta./x_4).^(9/10)).^(-1/9);

%% PLOTS
%%%%%%%%%%%%%%%%%%%%%%%%%%%%%%%%%%%%%%%%%%%%%%%%%%%%%%%%%%%%%%%%%%%%%%%% Side-by-side corrected steady state temperatures
%%%%%%%%%%%%%%%%%%%%%%%%%%%%%%%%%%%%%%%%%%%%%%%%%%%%%%%%%%%%%%%%%%%%%%%%
figure(1)

```

```

set(gca,'FontSize',12)
imagesc(x_0, y, (Pos_0_Cor)-FS_avg)
colorbar
axis image
hold on
plot([1.7285 1.7285], [9.52 14.64], 'k--', 'LineWidth', 2)
plot([7.2285 7.2285], [9.52 14.64], 'k--', 'LineWidth', 2)

imagesc(x_1, y, (Pos_1_Cor)-FS_avg)
colorbar
axis image
plot([7.4785 7.4785], [9.52 14.64], 'k--', 'LineWidth', 2)
plot([14.4785 14.4785], [9.52 14.64], 'k--', 'LineWidth', 2)

imagesc(x_2, y, (Pos_2_Cor)-FS_avg)
colorbar
axis image
plot([14.7285 14.7285], [9.52 14.64], 'k--', 'LineWidth', 2)
plot([21.7285 21.7285], [9.52 14.64], 'k--', 'LineWidth', 2)

imagesc(x_3, y, (Pos_3_Cor)-FS_avg)
colorbar
axis image
plot([21.9785 21.9785], [9.52 14.64], 'k--', 'LineWidth', 2)
plot([28.9785 28.9785], [9.52 14.64], 'k--', 'LineWidth', 2)

imagesc(x_4, y, (Pos_4_Cor)-FS_avg)
colorbar
axis image
plot([29.2285 29.2285], [9.52 14.64], 'k--', 'LineWidth', 2)
plot([36.2285 36.2285], [9.52 14.64], 'k--', 'LineWidth', 2)

caxis([0, 15])
axis([0 36.5 10 14])
xlabel('\bf x [in]')
ylabel('\bf y [in]')
title('\bf Steady State Temperature [K]: Smooth Turbulent (USL)')
hold off

%%%%%%%%%%%%%%%%%%%%%%%%%%%%%%%%%%%%%%%%%%%%%%%%%%%%%%%%%%%%%%%%%%%%%%%% Side-by-side heat trasfer coefficients
%%%%%%%%%%%%%%%%%%%%%%%%%%%%%%%%%%%%%%%%%%%%%%%%%%%%%%%%%%%%%%%%%%%%%%%%
figure(2)
set(gca,'FontSize',12)
imagesc(x_0, y, (h_0))
colorbar
axis image
hold on
plot([1.7285 1.7285], [9.52 14.64], 'k--', 'LineWidth', 2)
plot([7.2285 7.2285], [9.52 14.64], 'k--', 'LineWidth', 2)

imagesc(x_1, y, (h_1))
colorbar
axis image
plot([7.4785 7.4785], [9.52 14.64], 'k--', 'LineWidth', 2)
plot([14.4785 14.4785], [9.52 14.64], 'k--', 'LineWidth', 2)

```

```

imagesc(x_2, y, (h_2))
colorbar
axis image
plot([14.7285 14.7285], [9.52 14.64], 'k--', 'LineWidth', 2)
plot([21.7285 21.7285], [9.52 14.64], 'k--', 'LineWidth', 2)

imagesc(x_3, y, (h_3))
colorbar
axis image
plot([21.9785 21.9785], [9.52 14.64], 'k--', 'LineWidth', 2)
plot([28.9785 28.9785], [9.52 14.64], 'k--', 'LineWidth', 2)

imagesc(x_4, y, (h_4))
colorbar
axis image
plot([29.2285 29.2285], [9.52 14.64], 'k--', 'LineWidth', 2)
plot([36.2285 36.2285], [9.52 14.64], 'k--', 'LineWidth', 2)

caxis([20, 80])
axis([0 36.5 10.00 14.00])
xlabel('\bf x [in]')
ylabel('\bf y [in]')
title('\bf h [W/m^2K]: Smooth Turbulent (USL)')
hold off

%%%%%%%%%%%%%%%%%%%%%%%%%%%%%%%%%%%%%%%%%%%%%%%%%%%%%%%%%%%%%%%%%%%%%%%% Centerline heat trasfer coefficients vs. theoretical
%%%%%%%%%%%%%%%%%%%%%%%%%%%%%%%%%%%%%%%%%%%%%%%%%%%%%%%%%%%%%%%%%%%%%%%%
figure(3)
set(gca, 'FontSize', 12)
plot(x_0(25:298), (h_0_avg(25:298)), 'b-', 'LineWidth', 2)
grid on
hold on
plot(x_0(25:298), h_lam_0(25:298), 'r-.', 'LineWidth', 2)

plot(x_1, (h_1_avg), 'b-', 'LineWidth', 2)
plot(x_1, (h_lam_1), 'r-.', 'LineWidth', 2)

plot(x_2, (h_2_avg), 'b-', 'LineWidth', 2)
plot(x_2, (h_lam_2), 'r-.', 'LineWidth', 2)

plot(x_3, (h_3_avg), 'b-', 'LineWidth', 2)
plot(x_3, (h_lam_3), 'r-.', 'LineWidth', 2)

plot(x_4, (h_4_avg), 'b-', 'LineWidth', 2)
plot(x_4, (h_lam_4), 'r-.', 'LineWidth', 2)
xlabel('\bf x [in]')
ylabel('\bf h [W/m^2K]')
title('\bf Smooth Turbulent (USL)')
legend('\bf Experimental Centerline \pm 0.5"', '\bf Turbulent Theoretical')
axis([0 36 0 100])
axis square

hold off

```

## APPENDIX B

This appendix provides the Mathcad code used to generate the 50 x 50 pixel averaged piont plots. This Mathcad code also contains the uncertainty analysis for the convective heat transfer coefficients.

### Read in data and assign variable names

#### Steady-state data file from MATLAB

SS\_Data :=  
Stead\_State\_Data.txt

#### Heated area power measurements

Voltage

$$E := \begin{pmatrix} \text{SS\_Data}_{5,35} \\ \text{SS\_Data}_{5,35} \\ \text{SS\_Data}_{5,35} \\ \text{SS\_Data}_{6,36} \\ \text{SS\_Data}_{6,36} \\ \text{SS\_Data}_{7,37} \\ \text{SS\_Data}_{8,38} \\ 5.948 \end{pmatrix} V = \begin{pmatrix} 5.794 \\ 5.794 \\ 5.794 \\ 5.888 \\ 5.888 \\ 5.803 \\ 5.87 \\ 5.948 \end{pmatrix} V$$

Current

$$I := \begin{pmatrix} 2 \cdot (\text{SS\_Data}_{5,39} - \text{SS\_Data}_{0,39}) \\ 2 \cdot (\text{SS\_Data}_{5,39} - \text{SS\_Data}_{0,39}) \\ 2 \cdot (\text{SS\_Data}_{5,39} - \text{SS\_Data}_{0,39}) \\ \text{SS\_Data}_{6,40} - \text{SS\_Data}_{1,40} \\ \text{SS\_Data}_{6,40} - \text{SS\_Data}_{1,40} \\ \text{SS\_Data}_{7,41} - \text{SS\_Data}_{2,41} \\ \text{SS\_Data}_{8,42} - \text{SS\_Data}_{3,42} \\ 2.653 \end{pmatrix} A = \begin{pmatrix} 2.103 \\ 2.103 \\ 2.103 \\ 2.666 \\ 2.666 \\ 2.646 \\ 2.634 \\ 2.653 \end{pmatrix} A$$

#### Heated area measurements

Heated area width and length

$$W_{ha} := \begin{pmatrix} 6.375 \\ 6.375 \\ 6.375 \\ 6.375 \\ 6.375 \\ 6.375 \\ 6.375 \\ 6.375 \end{pmatrix} \text{in} \quad L_{ha} := \begin{pmatrix} 5.5 \\ 5.5 \\ 7 \\ 7 \\ 7 \\ 7 \\ 7 \\ 7 \end{pmatrix} \text{in}$$

$$A_t := \overrightarrow{(W_{ha} \cdot L_{ha})} = \begin{pmatrix} 35.063 \\ 35.063 \\ 35.063 \\ 44.625 \\ 44.625 \\ 44.625 \\ 44.625 \\ 44.625 \end{pmatrix} \cdot \text{in}^2$$



### Plexiglas properties

Thickness

Thermal conductivity

$$t_p := \begin{pmatrix} 0.72 \\ 0.72 \\ 0.72 \\ 0.72 \\ 0.72 \\ 0.72 \\ 0.72 \\ 0.72 \\ 0.72 \end{pmatrix} \text{ in}$$

$$k_p := 0.205 \frac{\text{W}}{\text{m} \cdot \text{K}}$$

$$c_c := \begin{pmatrix} 0.9 \\ 0.9 \\ 0.9 \\ 0.9 \\ 0.9 \\ 1.05 \\ 1.1 \\ 1.05 \end{pmatrix}$$

### Radiation constants

Surface emissivity

Stefan-Boltzman constant

$$\varepsilon_s := 0.95$$

$$\sigma := 5.67 \times 10^{-8} \frac{\text{W}}{\text{m}^2 \cdot \text{K}^4}$$

### Uncertainty constants

Student's t value

Correlated uncertainty

$$t := 2$$

$$B_T := 1.4\text{K}$$

### Section 0 IR temperature maps and 50 pixel by 50 pixel center point submatrix

SS\_0\_raw :=

Pos\_0\_SS.txt

Cal\_0\_raw :=

Pos\_0\_Cal.txt

$$SS_{0a} := \text{submatrix}(SS_{0\_raw}, 102, 151, 65, 114) ^\circ\text{C}$$

$$Cal_{0a} := \text{submatrix}(Cal_{0\_raw}, 102, 151, 65, 114) ^\circ\text{C}$$

$$SS_{0b} := \text{submatrix}(SS_{0\_raw}, 102, 151, 134, 183) ^\circ\text{C}$$

$$Cal_{0b} := \text{submatrix}(Cal_{0\_raw}, 102, 151, 134, 183) ^\circ\text{C}$$

$$SS_{0c} := \text{submatrix}(SS_{0\_raw}, 102, 151, 203, 252) ^\circ\text{C}$$

$$Cal_{0c} := \text{submatrix}(Cal_{0\_raw}, 102, 151, 203, 252) ^\circ\text{C}$$

### Section 1 IR temperature maps and 50 pixel by 50 pixel center point submatrix

SS\_1\_raw :=

Pos\_1\_SS.txt

Cal\_1\_raw :=

Pos\_1\_Cal.txt

$$SS_{1a} := \text{submatrix}(SS_{1\_raw}, 102, 151, 47, 96) ^\circ\text{C}$$

$$Cal_{1a} := \text{submatrix}(Cal_{1\_raw}, 102, 151, 47, 96) ^\circ\text{C}$$

$$SS_{1b} := \text{submatrix}(SS_{1\_raw}, 102, 151, 134, 183) ^\circ\text{C}$$

$$Cal_{1b} := \text{submatrix}(Cal_{1\_raw}, 102, 151, 134, 183) ^\circ\text{C}$$

## Section 2 IR temperature maps and 50 pixel by 50 pixel center point submatrix

SS\_2\_raw :=

Pos\_2\_SS.txt

Cal\_2\_raw :=

Pos\_2\_Cal.txt

SS\_2 := submatrix(SS\_2\_raw, 102, 151, 134, 183) °C

Cal\_2 := submatrix(Cal\_2\_raw, 102, 151, 134, 183) °C

## Section 3 IR temperature maps and 50 pixel by 50 pixel center point submatrix

SS\_3\_raw :=

Pos\_3\_SS.txt

Cal\_3\_raw :=

Pos\_3\_Cal.txt

SS\_3 := submatrix(SS\_3\_raw, 102, 151, 134, 183) °C

Cal\_3 := submatrix(Cal\_3\_raw, 102, 151, 134, 183) °C

## Section 4 IR temperature maps and 50 pixel by 50 pixel center point submatrix

SS\_4\_raw :=

Pos\_4\_SS.txt

Cal\_4\_raw :=

Pos\_4\_Cal.txt

SS\_4 := submatrix(SS\_4\_raw, 102, 151, 134, 183) °C

Cal\_4 := submatrix(Cal\_4\_raw, 102, 151, 134, 183) °C

## Subsurface, under plate, and freestream thermocouple measurements

calibration    steady state

$$T_{SS\_raw} := \begin{pmatrix} SS\_Data_{0,1} & SS\_Data_{5,1} \\ SS\_Data_{0,2} & SS\_Data_{5,2} \\ SS\_Data_{0,3} & SS\_Data_{5,3} \\ SS\_Data_{1,4} & SS\_Data_{6,4} \\ SS\_Data_{1,5} & SS\_Data_{6,5} \\ SS\_Data_{2,6} & SS\_Data_{7,6} \\ SS\_Data_{3,7} & SS\_Data_{8,7} \\ SS\_Data_{4,8} & SS\_Data_{9,8} \end{pmatrix} ^\circ C$$

calibration    steady state

$$T_{UP\_raw} := \begin{pmatrix} SS\_Data_{0,9} & SS\_Data_{5,9} \\ SS\_Data_{0,10} & SS\_Data_{5,10} \\ SS\_Data_{0,11} & SS\_Data_{5,11} \\ SS\_Data_{1,12} & SS\_Data_{6,12} \\ SS\_Data_{1,13} & SS\_Data_{6,13} \\ SS\_Data_{2,14} & SS\_Data_{7,14} \\ SS\_Data_{3,15} & SS\_Data_{8,15} \\ SS\_Data_{4,16} & SS\_Data_{9,16} \end{pmatrix} ^\circ C$$

calibration    steady state

$$T_{\text{inf\_raw}} := \begin{pmatrix} \text{SS\_Data}_{0,17} & \text{SS\_Data}_{5,17} \\ \text{SS\_Data}_{0,17} & \text{SS\_Data}_{5,17} \\ \text{SS\_Data}_{0,17} & \text{SS\_Data}_{5,17} \\ \text{SS\_Data}_{1,17} & \text{SS\_Data}_{6,17} \\ \text{SS\_Data}_{1,17} & \text{SS\_Data}_{6,17} \\ \text{SS\_Data}_{2,17} & \text{SS\_Data}_{7,17} \\ \text{SS\_Data}_{3,17} & \text{SS\_Data}_{8,17} \\ \text{SS\_Data}_{4,17} & \text{SS\_Data}_{9,17} \end{pmatrix} ^{\circ}\text{C}$$

### **Calculate the corrected temperature values**

#### **Freestream average temperature at calibration**

$$T_{0\text{cal}} := \text{mean}(\text{mean}(\text{Cal\_0b})) = 294.834 \text{ K}$$

$$T_{1\text{cal}} := \text{mean}(\text{mean}(\text{Cal\_1b})) = 294.805 \text{ K}$$

$$T_{2\text{cal}} := \text{mean}(\text{mean}(\text{Cal\_2})) = 294.792 \text{ K}$$

$$T_{3\text{cal}} := \text{mean}(\text{mean}(\text{Cal\_3})) = 294.723 \text{ K}$$

$$T_{4\text{cal}} := \text{mean}(\text{mean}(\text{Cal\_4})) = 294.683 \text{ K}$$

#### **Create a calibration matrix**

$$T_{\text{cal}} := \begin{pmatrix} T_{0\text{cal}} \\ T_{0\text{cal}} \\ T_{0\text{cal}} \\ T_{1\text{cal}} \\ T_{1\text{cal}} \\ T_{2\text{cal}} \\ T_{3\text{cal}} \\ T_{4\text{cal}} \end{pmatrix}$$

**Corrected steady state temperatures for subsurface, under plate, and freestream thermocouples**

$$T_{SS} := T_{SS\_raw}^{\langle 1 \rangle} - \left( T_{SS\_raw}^{\langle 0 \rangle} - T_{cal} \right) = \begin{pmatrix} 311.743 \\ 311.561 \\ 312.578 \\ 315.715 \\ 317.752 \\ 313.976 \\ 315.743 \\ 318.342 \end{pmatrix} K \quad \text{Subsurface temperature}$$

$$T_{UP} := T_{UP\_raw}^{\langle 1 \rangle} - \left( T_{UP\_raw}^{\langle 0 \rangle} - T_{cal} \right) = \begin{pmatrix} 298.646 \\ 296.278 \\ 297.159 \\ 298.341 \\ 298.579 \\ 299.124 \\ 300.091 \\ 300.82 \end{pmatrix} K \quad \text{Under the plate temperature}$$

$$T_{\infty} := T_{inf\_raw}^{\langle 1 \rangle} - \left( T_{inf\_raw}^{\langle 0 \rangle} - T_{cal} \right) = \begin{pmatrix} 295.668 \\ 295.668 \\ 295.668 \\ 295.394 \\ 295.394 \\ 295.318 \\ 295.329 \\ 293.947 \end{pmatrix} K \quad \text{Freestream temperature}$$

**Corrected IR temperature measurement, averaged in the 50x50 pixel center area**

$$T_{avg} := \begin{pmatrix} \overrightarrow{\text{mean(SS\_0a)}} \\ \overrightarrow{\text{mean(SS\_0b)}} \\ \overrightarrow{\text{mean(SS\_0c)}} \\ \overrightarrow{\text{mean(SS\_1a)}} \\ \overrightarrow{\text{mean(SS\_1b)}} \\ \overrightarrow{\text{mean(SS\_2)}} \\ \overrightarrow{\text{mean(SS\_3)}} \\ \overrightarrow{\text{mean(SS\_4)}} \end{pmatrix} = \begin{pmatrix} 299.528 \\ 300.484 \\ 301.522 \\ 303.114 \\ 303.441 \\ 305.073 \\ 305.227 \\ 306.076 \end{pmatrix} K \quad \text{Area averaged IR temperature}$$

### IR temperture standard deviation

$$S_{T_{avg}} := \begin{bmatrix} \text{stdev}(SS\_0a) \\ \text{stdev}(SS\_0b) \\ \text{stdev}(SS\_0c) \\ \text{stdev}(SS\_1a) \\ \text{stdev}(SS\_1b) \\ \text{stdev}(SS\_2) \\ \text{stdev}(SS\_3) \\ \text{stdev}(SS\_4) \end{bmatrix} = \begin{pmatrix} 0.076 \\ 0.281 \\ 0.175 \\ 0.073 \\ 0.079 \\ 0.061 \\ 0.033 \\ 0.079 \end{pmatrix} \text{ K}$$

$$T_{inf\_avg} := \begin{bmatrix} \frac{(T_{\infty 1} + T_{\infty 4} + T_{\infty 5} + T_{\infty 7} + T_{\infty 6})}{5} \\ \frac{(T_{\infty 1} + T_{\infty 4} + T_{\infty 5} + T_{\infty 7} + T_{\infty 6})}{5} \\ \frac{(T_{\infty 1} + T_{\infty 4} + T_{\infty 5} + T_{\infty 7} + T_{\infty 6})}{5} \\ \frac{(T_{\infty 1} + T_{\infty 4} + T_{\infty 5} + T_{\infty 7} + T_{\infty 6})}{5} \\ \frac{(T_{\infty 1} + T_{\infty 4} + T_{\infty 5} + T_{\infty 7} + T_{\infty 6})}{5} \\ \frac{(T_{\infty 1} + T_{\infty 4} + T_{\infty 5} + T_{\infty 7} + T_{\infty 6})}{5} \\ \frac{(T_{\infty 1} + T_{\infty 4} + T_{\infty 5} + T_{\infty 7} + T_{\infty 6})}{5} \\ \frac{(T_{\infty 1} + T_{\infty 4} + T_{\infty 5} + T_{\infty 7} + T_{\infty 6})}{5} \end{bmatrix}$$

### Calculated average convective heat transfer coefficients

$$h_{avg}(E, I, A_t, k_p, t_p, T_{SS}, T_{UP}, \varepsilon, \sigma, T_{inf\_avg}, T_{avg}, c_c) := \frac{\left[ \frac{E \cdot I}{A_t} - \frac{c_c \cdot k_p}{t_p} \cdot (T_{SS} - T_{UP}) - \varepsilon \cdot \sigma \cdot (T_{avg}^4 - T_{inf\_avg}^4) \right]}{(T_{avg} - T_{inf\_avg})}$$

$$h := h_{\text{avg}}(E, I, A_t, k_p, t_p, T_{\text{SS}}, T_{\text{UP}}, \varepsilon, \sigma, T_{\text{inf\_avg}}, T_{\text{avg}}, c_c) = \begin{pmatrix} 86.793 \\ 66.129 \\ 54.225 \\ 40.591 \\ 36.575 \\ 30.234 \\ 28.245 \\ 25.381 \end{pmatrix} \cdot \frac{\text{W}}{\text{m}^2 \cdot \text{K}}$$

Calculated convective heat transfer coefficients

### Uncertainty components for voltage

#### Random and fixed uncertainties

$$U_{E\_rand} := \begin{pmatrix} \text{SS\_Data}_{5,43} \\ \text{SS\_Data}_{5,43} \\ \text{SS\_Data}_{5,43} \\ \text{SS\_Data}_{6,44} \\ \text{SS\_Data}_{6,44} \\ \text{SS\_Data}_{7,45} \\ \text{SS\_Data}_{8,46} \\ 0 \end{pmatrix} \cdot \begin{pmatrix} 9.65 \times 10^{-5} \\ 9.65 \times 10^{-5} \\ 9.65 \times 10^{-5} \\ 1.462 \times 10^{-4} \\ 1.462 \times 10^{-4} \\ 1.858 \times 10^{-4} \\ 1.422 \times 10^{-4} \\ 0 \end{pmatrix} \cdot \text{V}$$

$$U_{E\_fixed} := \begin{pmatrix} 0.03\% \cdot E_0 \\ 0.03\% \cdot E_1 \\ 0.03\% \cdot E_2 \\ 0.03\% \cdot E_3 \\ 0.03\% \cdot E_4 \\ 0.03\% \cdot E_5 \\ 0.03\% \cdot E_6 \\ 0.25\% \cdot E_7 \end{pmatrix} = \begin{pmatrix} 1.738 \times 10^{-3} \\ 1.738 \times 10^{-3} \\ 1.738 \times 10^{-3} \\ 1.767 \times 10^{-3} \\ 1.767 \times 10^{-3} \\ 1.741 \times 10^{-3} \\ 1.761 \times 10^{-3} \\ 0.015 \end{pmatrix} \cdot \text{V}$$

#### Total uncertainty

$$U_E := \sqrt{U_{E\_rand}^2 + U_{E\_fixed}^2} = \begin{pmatrix} 1.741 \times 10^{-3} \\ 1.741 \times 10^{-3} \\ 1.741 \times 10^{-3} \\ 1.773 \times 10^{-3} \\ 1.773 \times 10^{-3} \\ 1.751 \times 10^{-3} \\ 1.767 \times 10^{-3} \\ 0.015 \end{pmatrix} \cdot \text{V}$$

## Uncertainty components for current

### Random and fixed uncertainties

$$U_{I\_rand} := \begin{pmatrix} SS\_Data_{5,47} \\ SS\_Data_{5,47} \\ SS\_Data_{5,47} \\ SS\_Data_{6,48} \\ SS\_Data_{6,48} \\ SS\_Data_{6,48} \\ SS\_Data_{7,49} \\ SS\_Data_{8,50} \\ 0 \end{pmatrix} A = \begin{pmatrix} 2.924 \times 10^{-4} \\ 2.924 \times 10^{-4} \\ 2.924 \times 10^{-4} \\ 4.324 \times 10^{-4} \\ 4.324 \times 10^{-4} \\ 4.324 \times 10^{-4} \\ 5.619 \times 10^{-4} \\ 6.615 \times 10^{-4} \\ 0 \end{pmatrix} A$$

$$U_{I\_fixed} := \begin{pmatrix} 0.1A \\ 0.1A \\ 0.1A \\ 0.05A \\ 0.05A \\ 0.05A \\ 0.05A \\ 2.5\% \cdot I_4 \end{pmatrix} = \begin{pmatrix} 0.1 \\ 0.1 \\ 0.1 \\ 0.05 \\ 0.05 \\ 0.05 \\ 0.05 \\ 0.067 \end{pmatrix} A$$

### Total uncertainty

$$U_I := \sqrt{U_{I\_rand}^2 + U_{I\_fixed}^2} = \begin{pmatrix} 0.1000004 \\ 0.1000004 \\ 0.1000004 \\ 0.0500019 \\ 0.0500019 \\ 0.0500032 \\ 0.0500044 \\ 0.0666604 \end{pmatrix} A$$

## Uncertainty components for heated area and Plexiglas thickness

### Fixed uncertainty for all distance measurements

$$U_{dist\_fixed} := \frac{1}{32} \text{ in}$$

$$U_{At} := \sqrt{(U_{dist\_fixed} \cdot W_{ha})^2 + (U_{dist\_fixed} \cdot L_{ha})^2} = \begin{pmatrix} 0.263 \\ 0.263 \\ 0.263 \\ 0.296 \\ 0.296 \\ 0.296 \\ 0.296 \\ 0.296 \end{pmatrix} \cdot \text{in}^2$$

## Total uncertainty in thickness

$$U_{tp} := \begin{pmatrix} U_{\text{dist\_fixed}} \\ U_{\text{dist\_fixed}} \\ U_{\text{dist\_fixed}} \\ U_{\text{dist\_fixed}} \\ U_{\text{dist\_fixed}} \\ U_{\text{dist\_fixed}} \\ U_{\text{dist\_fixed}} \\ U_{\text{dist\_fixed}} \end{pmatrix} = \begin{pmatrix} 0.031 \\ 0.031 \\ 0.031 \\ 0.031 \\ 0.031 \\ 0.031 \\ 0.031 \\ 0.031 \end{pmatrix} \cdot \text{in}$$

## Uncertainty for thermocouple temperatures

### Random uncertainties

calibration    steady state

$$U_{TSS\_raw} := \begin{pmatrix} SS\_Data_{5,18} & SS\_Data_{5,18} \\ SS\_Data_{0,19} & SS\_Data_{5,19} \\ SS\_Data_{5,20} & SS\_Data_{5,20} \\ SS\_Data_{1,21} & SS\_Data_{6,21} \\ SS\_Data_{1,22} & SS\_Data_{6,22} \\ SS\_Data_{2,23} & SS\_Data_{7,23} \\ SS\_Data_{3,24} & SS\_Data_{8,24} \\ SS\_Data_{4,25} & SS\_Data_{9,25} \end{pmatrix} \Delta^{\circ}\text{C} = \begin{pmatrix} 5.282 \times 10^{-3} & 5.282 \times 10^{-3} \\ 2.567 \times 10^{-3} & 3.495 \times 10^{-3} \\ 5.158 \times 10^{-3} & 5.158 \times 10^{-3} \\ 2.383 \times 10^{-3} & 3.347 \times 10^{-3} \\ 5.375 \times 10^{-3} & 3.229 \times 10^{-3} \\ 3.459 \times 10^{-3} & 3.681 \times 10^{-3} \\ 4.01 \times 10^{-3} & 4.815 \times 10^{-3} \\ 3.418 \times 10^{-3} & 3.085 \times 10^{-3} \end{pmatrix} \text{K}$$

calibration    steady state

$$U_{TUP\_raw} := \begin{pmatrix} SS\_Data_{0,26} & SS\_Data_{5,26} \\ SS\_Data_{0,27} & SS\_Data_{5,27} \\ SS\_Data_{0,28} & SS\_Data_{5,28} \\ SS\_Data_{1,29} & SS\_Data_{6,29} \\ SS\_Data_{1,30} & SS\_Data_{6,30} \\ SS\_Data_{2,31} & SS\_Data_{7,31} \\ SS\_Data_{3,32} & SS\_Data_{8,32} \\ SS\_Data_{4,33} & SS\_Data_{9,33} \end{pmatrix} \Delta^{\circ}\text{C} = \begin{pmatrix} 2.29 \times 10^{-3} & 4.507 \times 10^{-3} \\ 4.369 \times 10^{-3} & 8.878 \times 10^{-3} \\ 3.843 \times 10^{-3} & 7.081 \times 10^{-3} \\ 3.346 \times 10^{-3} & 4.423 \times 10^{-3} \\ 3.291 \times 10^{-3} & 3.62 \times 10^{-3} \\ 3.401 \times 10^{-3} & 2.108 \times 10^{-3} \\ 5.263 \times 10^{-3} & 4.145 \times 10^{-3} \\ 3.64 \times 10^{-3} & 3.797 \times 10^{-3} \end{pmatrix} \text{K}$$



$$\begin{array}{c} \text{calibration} \quad \text{steady state} \\ U_{\text{Tinf\_raw}} := \begin{pmatrix} \text{SS\_Data}_{0,34} & \text{SS\_Data}_{5,34} \\ \text{SS\_Data}_{0,34} & \text{SS\_Data}_{5,34} \\ \text{SS\_Data}_{0,34} & \text{SS\_Data}_{5,34} \\ \text{SS\_Data}_{1,34} & \text{SS\_Data}_{6,34} \\ \text{SS\_Data}_{1,34} & \text{SS\_Data}_{6,34} \\ \text{SS\_Data}_{2,34} & \text{SS\_Data}_{7,34} \\ \text{SS\_Data}_{3,34} & \text{SS\_Data}_{8,34} \\ \text{SS\_Data}_{4,34} & \text{SS\_Data}_{9,34} \end{pmatrix} \Delta^{\circ}\text{C} = \begin{pmatrix} 4.748 \times 10^{-3} & 5.955 \times 10^{-3} \\ 4.748 \times 10^{-3} & 5.955 \times 10^{-3} \\ 4.748 \times 10^{-3} & 5.955 \times 10^{-3} \\ 4.288 \times 10^{-3} & 6.494 \times 10^{-3} \\ 4.288 \times 10^{-3} & 6.494 \times 10^{-3} \\ 5.559 \times 10^{-3} & 4.735 \times 10^{-3} \\ 4.441 \times 10^{-3} & 4.527 \times 10^{-3} \\ 0.048 & 8.75 \times 10^{-3} \end{pmatrix} \text{K} \end{array}$$

### Uncertainty for IR camera temperatures

#### Random uncertainty

$$U_{\text{Tavg\_rand}} := \frac{t \cdot S_{\text{Tavg}}}{\sqrt{2500}} = \begin{pmatrix} 3.041 \times 10^{-3} \\ 0.011 \\ 6.998 \times 10^{-3} \\ 2.905 \times 10^{-3} \\ 3.145 \times 10^{-3} \\ 2.441 \times 10^{-3} \\ 1.325 \times 10^{-3} \\ 3.17 \times 10^{-3} \end{pmatrix} \text{K}$$

#### Total uncertainty

$$U_{\text{Tavg}} := \sqrt{U_{\text{Tavg\_rand}}^2 + B_{\text{T}}^2} = \begin{pmatrix} 1.4000033 \\ 1.4000452 \\ 1.4000175 \\ 1.4000003 \\ 1.4000035 \\ 1.4000021 \\ 1.4000006 \\ 1.4000036 \end{pmatrix} \text{K}$$

### Total uncertainty in subsurface TC measurements

$$U_{TSS} := \sqrt{\left( U_{TSS\_raw}^{\langle 0 \rangle} \right)^2 + \left( U_{TSS\_raw}^{\langle 1 \rangle} \right)^2 + \left( U_{Tavg\_rand} \right)^2 + B_T^2} = \begin{pmatrix} 1.4000232 \\ 1.4000519 \\ 1.4000365 \\ 1.400009 \\ 1.4000176 \\ 1.4000112 \\ 1.4000147 \\ 1.4000112 \end{pmatrix}^K$$

### Total uncertainty in under the plate TC measurements

$$U_{TUP} := \sqrt{\left( U_{TUP\_raw}^{\langle 0 \rangle} \right)^2 + \left( U_{TUP\_raw}^{\langle 1 \rangle} \right)^2 + \left( U_{Tavg\_rand} \right)^2 + B_T^2} = \begin{pmatrix} 1.4000124 \\ 1.4000802 \\ 1.4000407 \\ 1.400014 \\ 1.4000121 \\ 1.4000078 \\ 1.4000167 \\ 1.4000135 \end{pmatrix}^K$$

### Total uncertainty in freestream TC measurements

$$U_{T\infty} := \sqrt{\left( U_{Tinf\_raw}^{\langle 0 \rangle} \right)^2 + \left( U_{Tavg\_rand} \right)^2 + \left( B_T \right)^2} = \begin{pmatrix} 1.4000114 \\ 1.4000533 \\ 1.4000255 \\ 1.4000096 \\ 1.4000101 \\ 1.4000132 \\ 1.4000077 \\ 1.4008145 \end{pmatrix}^K$$

$$U_{T.inf\_avg} := \sqrt{\sqrt{\sqrt{\sqrt{\sqrt{\sqrt{\sqrt{\sqrt{\frac{(U_{T\infty 1})^2}{5} + \frac{(U_{T\infty 4})^2}{5} + \frac{(U_{T\infty 5})^2}{5} + \frac{(U_{T\infty 6})^2}{5} + \frac{(U_{T\infty 7})^2}{5}}}{\frac{(U_{T\infty 1})^2}{5} + \frac{(U_{T\infty 4})^2}{5} + \frac{(U_{T\infty 5})^2}{5} + \frac{(U_{T\infty 6})^2}{5} + \frac{(U_{T\infty 7})^2}{5}}}{\frac{(U_{T\infty 1})^2}{5} + \frac{(U_{T\infty 4})^2}{5} + \frac{(U_{T\infty 5})^2}{5} + \frac{(U_{T\infty 6})^2}{5} + \frac{(U_{T\infty 7})^2}{5}}}{\frac{(U_{T\infty 1})^2}{5} + \frac{(U_{T\infty 4})^2}{5} + \frac{(U_{T\infty 5})^2}{5} + \frac{(U_{T\infty 6})^2}{5} + \frac{(U_{T\infty 7})^2}{5}}}{\frac{(U_{T\infty 1})^2}{5} + \frac{(U_{T\infty 4})^2}{5} + \frac{(U_{T\infty 5})^2}{5} + \frac{(U_{T\infty 6})^2}{5} + \frac{(U_{T\infty 7})^2}{5}}}{\frac{(U_{T\infty 1})^2}{5} + \frac{(U_{T\infty 4})^2}{5} + \frac{(U_{T\infty 5})^2}{5} + \frac{(U_{T\infty 6})^2}{5} + \frac{(U_{T\infty 7})^2}{5}}}$$

$$U_{kp} := 0.033 \frac{W}{m \cdot K}$$

## **Overall uncertainty in average convective heat transfer coefficients**

### **Partial derivatives of $h$ with respect to each variable**

$$\theta_E(E, I, A_t, k_p, t_p, T_{SS}, T_{UP}, \varepsilon, \sigma, T_{inf\_avg}, T_{avg}, c_c) := \frac{d}{dE} h_{avg}(E, I, A_t, k_p, t_p, T_{SS}, T_{UP}, \varepsilon, \sigma, T_{inf\_avg}, T_{avg}, c_c)$$

$$\theta_I(E, I, A_t, k_p, t_p, T_{SS}, T_{UP}, \varepsilon, \sigma, T_{inf\_avg}, T_{avg}, c_c) := \frac{d}{dI} h_{avg}(E, I, A_t, k_p, t_p, T_{SS}, T_{UP}, \varepsilon, \sigma, T_{inf\_avg}, T_{avg}, c_c)$$

$$\theta_{A_t}(E, I, A_t, k_p, t_p, T_{SS}, T_{UP}, \varepsilon, \sigma, T_{inf\_avg}, T_{avg}, c_c) := \frac{d}{dA_t} h_{avg}(E, I, A_t, k_p, t_p, T_{SS}, T_{UP}, \varepsilon, \sigma, T_{inf\_avg}, T_{avg}, c_c)$$

$$\theta_{tp}(E, I, A_t, k_p, t_p, T_{SS}, T_{UP}, \varepsilon, \sigma, T_{inf\_avg}, T_{avg}, c_c) := \frac{d}{dt_p} h_{avg}(E, I, A_t, k_p, t_p, T_{SS}, T_{UP}, \varepsilon, \sigma, T_{inf\_avg}, T_{avg}, c_c)$$

$$\theta_{TSS}(E, I, A_t, k_p, t_p, T_{SS}, T_{UP}, \varepsilon, \sigma, T_{inf\_avg}, T_{avg}, c_c) := \frac{d}{dT_{SS}} h_{avg}(E, I, A_t, k_p, t_p, T_{SS}, T_{UP}, \varepsilon, \sigma, T_{inf\_avg}, T_{avg}, c_c)$$

$$\theta_{TUP}(E, I, A_t, k_p, t_p, T_{SS}, T_{UP}, \varepsilon, \sigma, T_{inf\_avg}, T_{avg}, c_c) := \frac{d}{dT_{UP}} h_{avg}(E, I, A_t, k_p, t_p, T_{SS}, T_{UP}, \varepsilon, \sigma, T_{inf\_avg}, T_{avg}, c_c)$$

$$\theta_{T\infty}(E, I, A_t, k_p, t_p, T_{SS}, T_{UP}, \varepsilon, \sigma, T_{inf\_avg}, T_{avg}, c_c) := \frac{d}{dT_{inf\_avg}} h_{avg}(E, I, A_t, k_p, t_p, T_{SS}, T_{UP}, \varepsilon, \sigma, T_{inf\_avg}, T_{avg}, c_c)$$

$$\theta_{Tavg}(E, I, A_t, k_p, t_p, T_{SS}, T_{UP}, \varepsilon, \sigma, T_{inf\_avg}, T_{avg}, c_c) := \frac{d}{dT_{avg}} h_{avg}(E, I, A_t, k_p, t_p, T_{SS}, T_{UP}, \varepsilon, \sigma, T_{inf\_avg}, T_{avg}, c_c)$$

$$\theta_{kp}(E, I, A_t, k_p, t_p, T_{SS}, T_{UP}, \varepsilon, \sigma, T_{inf\_avg}, T_{avg}, c_c) := \frac{d}{dk_p} h_{avg}(E, I, A_t, k_p, t_p, T_{SS}, T_{UP}, \varepsilon, \sigma, T_{inf\_avg}, T_{avg}, c_c)$$

### Calculated uncertainty components

$$\Psi_E := \left[ \left( U_E \cdot \theta_E(E, I, A_t, k_p, t_p, T_{SS}, T_{UP}, \varepsilon, \sigma, T_{inf\_avg}, T_{avg}, c_c) \right) \right]^2 = \begin{pmatrix} 1.355 \times 10^{-3} \\ 9.141 \times 10^{-4} \\ 6.414 \times 10^{-4} \\ 4.229 \times 10^{-4} \\ 3.903 \times 10^{-4} \\ 2.619 \times 10^{-4} \\ 2.563 \times 10^{-4} \\ 0.016 \end{pmatrix} \cdot \left( \frac{W}{m^2 K} \right)^2$$

$$\Psi_I := \left[ \left( U_I \cdot \theta_I(E, I, A_t, k_p, t_p, T_{SS}, T_{UP}, \varepsilon, \sigma, T_{inf\_avg}, T_{avg}, c_c) \right) \right]^2 = \begin{pmatrix} 33.931 \\ 22.892 \\ 16.062 \\ 1.641 \\ 1.515 \\ 1.028 \\ 1.02 \\ 1.583 \end{pmatrix} \cdot \left( \frac{w}{m^2 K} \right)^2$$

$$\Psi_{At} := \left[ \left( U_{At} \cdot \theta_{At}(E, I, A_t, k_p, t_p, T_{SS}, T_{UP}, \varepsilon, \sigma, T_{inf\_avg}, T_{avg}, c_c) \right) \right]^2 = \begin{pmatrix} 0.845 \\ 0.57 \\ 0.4 \\ 0.205 \\ 0.189 \\ 0.126 \\ 0.124 \\ 0.11 \end{pmatrix} \cdot \left( \frac{w}{m^2 K} \right)^2$$

$$\Psi_{tp} := \left[ \left( U_{tp} \cdot \theta_{tp}(E, I, A_t, k_p, t_p, T_{SS}, T_{UP}, \varepsilon, \sigma, T_{inf\_avg}, T_{avg}, c_c) \right) \right]^2 = \begin{pmatrix} 1.701 \\ 1.563 \\ 1.116 \\ 0.908 \\ 1.021 \\ 0.582 \\ 0.688 \\ 0.669 \end{pmatrix} \cdot \left( \frac{w}{m^2 K} \right)^2$$

$$\Psi_{TSS} := \left[ \left( U_{TSS} \cdot \theta_{TSS}(E, I, A_t, k_p, t_p, T_{SS}, T_{UP}, \varepsilon, \sigma, T_{inf\_avg}, T_{avg}, c_c) \right) \right]^2 = \begin{pmatrix} 10.319 \\ 6.962 \\ 4.885 \\ 3.13 \\ 2.889 \\ 2.747 \\ 2.924 \\ 2.267 \end{pmatrix} \cdot \left( \frac{w}{m^2 K} \right)^2$$

$$\Psi_{TUP} := \left[ \overline{\left( U_{TUP} \cdot \theta_{TUP}(E, I, A_t, k_p, t_p, T_{SS}, T_{UP}, \varepsilon, \sigma, T_{inf\_avg}, T_{avg}, c_c) \right)} \right]^2 = \begin{pmatrix} 10.319 \\ 6.962 \\ 4.885 \\ 3.13 \\ 2.889 \\ 2.747 \\ 2.924 \\ 2.267 \end{pmatrix} \cdot \left( \frac{w}{m^2 K} \right)^2$$

$$\Psi_{T\infty} := \left[ \overline{\left[ \frac{\frac{E \cdot I}{A_t} - \sigma \cdot \varepsilon \cdot (T_{avg}^4 - T_{inf\_avg}^4) + \frac{k_p \cdot (T_{UP} - T_{SS})}{t_p}}{(T_{avg} - T_{inf\_avg})^2} + \frac{4 \cdot \sigma \cdot \varepsilon \cdot T_{inf\_avg}^3}{T_{avg} - T_{inf\_avg}} \right] \cdot U_{T\_inf\_avg}} \right]^2 = \begin{pmatrix} 803.119 \\ 320.719 \\ 156.286 \\ 58.724 \\ 44.363 \\ 26.587 \\ 24.273 \\ 16.568 \end{pmatrix} \cdot \left( \frac{w}{m^2 K} \right)^2$$

$$\Psi_{Tavg} := \left[ \overline{\left( U_{Tavg} \cdot \theta_{Tavg}(E, I, A_t, k_p, t_p, T_{SS}, T_{UP}, \varepsilon, \sigma, T_{inf\_avg}, T_{avg}, c_c) \right)} \right]^2 = \begin{pmatrix} 869.008 \\ 354.349 \\ 173.529 \\ 66.766 \\ 51.503 \\ 26.206 \\ 22.721 \\ 16.296 \end{pmatrix} \cdot \left( \frac{w}{m^2 K} \right)^2$$

$$\Psi_{kp} := \left[ \overrightarrow{\left( U_{kp} \cdot \theta_{kp}(E, I, A_t, k_p, t_p, T_{SS}, T_{UP}, \epsilon, \sigma, T_{inf\_avg}, T_{avg}, c_c) \right)} \right]^2 = \begin{pmatrix} 23.401 \\ 21.497 \\ 15.353 \\ 12.493 \\ 14.041 \\ 8.012 \\ 9.471 \\ 9.201 \end{pmatrix} \cdot \left( \frac{w}{m^2 K} \right)^2$$

### Correlated uncertainty contributions

$$\Psi_{CU1} := \left[ \frac{\overrightarrow{2\theta_{TSS}(E, I, A_t, k_p, t_p, T_{SS}, T_{UP}, \epsilon, \sigma, T_{inf\_avg}, T_{avg}, c_c)}}{\left( \theta_{TUP}(E, I, A_t, k_p, t_p, T_{SS}, T_{UP}, \epsilon, \sigma, T_{inf\_avg}, T_{avg}, c_c) \cdot B_T \right)^2} - 1 \right] = \begin{pmatrix} -20.637 \\ -13.923 \\ -9.769 \\ -6.261 \\ -5.778 \\ -5.495 \\ -5.848 \\ -4.533 \end{pmatrix} \cdot \left( \frac{w}{m^2 K} \right)^2$$

$$\Psi_{CU2} := \left[ \frac{\overrightarrow{2\theta_{TSS}(E, I, A_t, k_p, t_p, T_{SS}, T_{UP}, \epsilon, \sigma, T_{inf\_avg}, T_{avg}, c_c)}}{\left( \theta_{T\infty}(E, I, A_t, k_p, t_p, T_{SS}, T_{UP}, \epsilon, \sigma, T_{inf\_avg}, T_{avg}, c_c) \cdot B_T \right)^2} - 1 \right] = \begin{pmatrix} -188.874 \\ -98.907 \\ -57.871 \\ -28.627 \\ -24.121 \\ -16.7 \\ -16.023 \\ -11.909 \end{pmatrix} \cdot \left( \frac{w}{m^2 K} \right)^2$$

$$\overrightarrow{\left( \theta_{TSS}(E, I, A_t, k_p, t_p, T_{SS}, T_{UP}, \epsilon, \sigma, T_{inf\_avg}, T_{avg}, c_c) \right)} = \begin{pmatrix} -2.294 \\ -1.885 \\ -1.579 \\ -1.264 \\ -1.214 \\ -1.184 \\ -1.221 \\ -1.075 \end{pmatrix} \frac{kg}{K^2 \cdot s}$$

$$\Psi_{CU3} := \left[ \frac{2\theta_{TSS}(E, I, A_t, k_p, t_p, T_{SS}, T_{UP}, \varepsilon, \sigma, T_{inf\_avg}, T_{avg}, c_c)}{\left(\theta_{Tavg}(E, I, A_t, k_p, t_p, T_{SS}, T_{UP}, \varepsilon, \sigma, T_{inf\_avg}, T_{avg}, c_c) \cdot B_T\right)^2} - 1 \right] = \begin{pmatrix} 189.388 \\ 99.33 \\ 58.227 \\ 28.914 \\ 24.396 \\ 16.97 \\ 16.302 \\ 12.155 \end{pmatrix} \cdot \left(\frac{w}{m^2 K}\right)^2$$

$$\Psi_{CU4} := \left[ \frac{2\theta_{TUP}(E, I, A_t, k_p, t_p, T_{SS}, T_{UP}, \varepsilon, \sigma, T_{inf\_avg}, T_{avg}, c_c)}{\left(\theta_{T\infty}(E, I, A_t, k_p, t_p, T_{SS}, T_{UP}, \varepsilon, \sigma, T_{inf\_avg}, T_{avg}, c_c) \cdot B_T\right)^2} - 1 \right] = \begin{pmatrix} 188.874 \\ 98.907 \\ 57.871 \\ 28.627 \\ 24.121 \\ 16.7 \\ 16.023 \\ 11.909 \end{pmatrix} \cdot \left(\frac{w}{m^2 K}\right)^2$$

$$\Psi_{CU5} := \left[ \frac{2\theta_{TUP}(E, I, A_t, k_p, t_p, T_{SS}, T_{UP}, \varepsilon, \sigma, T_{inf\_avg}, T_{avg}, c_c)}{\left(\theta_{Tavg}(E, I, A_t, k_p, t_p, T_{SS}, T_{UP}, \varepsilon, \sigma, T_{inf\_avg}, T_{avg}, c_c) \cdot B_T\right)^2} - 1 \right] = \begin{pmatrix} -189.388 \\ -99.33 \\ -58.227 \\ -28.914 \\ -24.396 \\ -16.97 \\ -16.302 \\ -12.155 \end{pmatrix} \cdot \left(\frac{w}{m^2 K}\right)^2$$

$$\Psi_{CU6} := \left[ \frac{2\theta_{T\infty}(E, I, A_t, k_p, t_p, T_{SS}, T_{UP}, \varepsilon, \sigma, T_{inf\_avg}, T_{avg}, c_c)}{\left(\theta_{Tavg}(E, I, A_t, k_p, t_p, T_{SS}, T_{UP}, \varepsilon, \sigma, T_{inf\_avg}, T_{avg}, c_c) \cdot B_T\right)^2} - 1 \right] = \begin{pmatrix} -1.733 \times 10^3 \\ -705.631 \\ -344.927 \\ -132.208 \\ -101.841 \\ -51.578 \\ -44.665 \\ -31.932 \end{pmatrix} \cdot \left(\frac{w}{m^2 K}\right)^2$$

**Overall uncertainty in h**

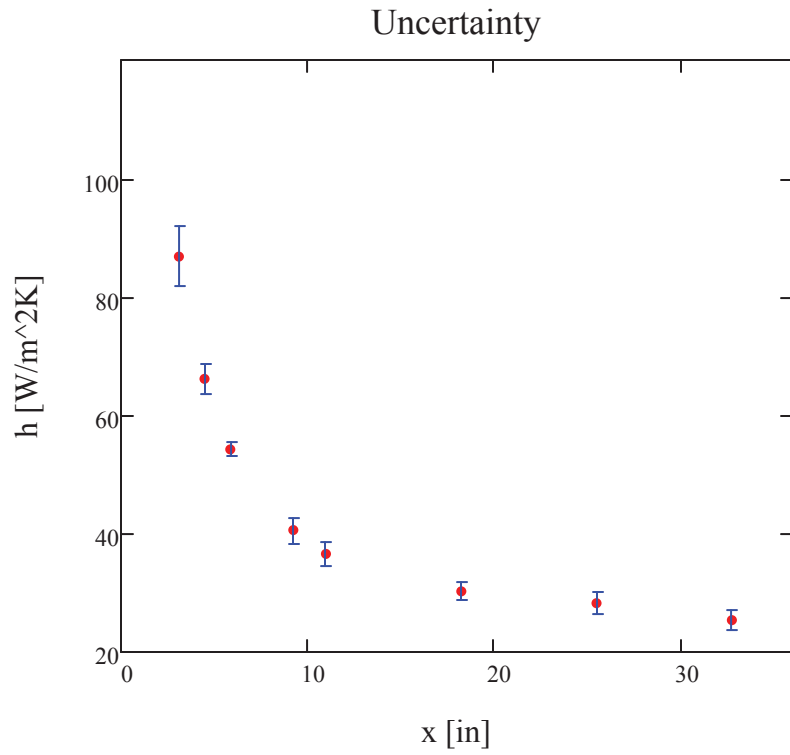


$$U_{\text{havg}} := \left[ \sqrt{\left( \Psi_E + \Psi_I + \Psi_{At} + \Psi_{TSS} + \Psi_{TUP} + \Psi_{T\infty} + \Psi_{Tavg} \dots \right. \right. \\ \left. \left. + \Psi_{CU1} + \Psi_{CU2} + \Psi_{CU3} + \Psi_{CU4} + \Psi_{CU5} + \Psi_{CU6} \right)^2} \right]^{\frac{1}{2}} = \begin{pmatrix} 5.13667 \\ 2.66433 \\ 1.16243 \\ 2.20701 \\ 2.06671 \\ 1.53952 \\ 1.86391 \\ 1.62524 \end{pmatrix} \cdot \frac{W}{m^2 K}$$

Percent uncertainty

$$\frac{U_{\text{havg}}}{h} = \begin{pmatrix} 5.918 \\ 4.029 \\ 2.144 \\ 5.437 \\ 5.651 \\ 5.092 \\ 6.599 \\ 6.403 \end{pmatrix} \% \quad h_{\text{low}} := h - U_{\text{havg}} = \begin{pmatrix} 81.656 \\ 63.465 \\ 53.062 \\ 38.384 \\ 34.509 \\ 28.694 \\ 26.381 \\ 23.756 \end{pmatrix} \cdot \frac{W}{m^2 K} \quad h_{\text{high}} := h + U_{\text{havg}} = \begin{pmatrix} 91.929 \\ 68.794 \\ 55.387 \\ 42.798 \\ 38.642 \\ 31.774 \\ 30.109 \\ 27.006 \end{pmatrix} \cdot \frac{W}{m^2 K}$$

$$x := \begin{pmatrix} 3.1035 \text{ in} \\ 4.4785 \text{ in} \\ 5.8535 \text{ in} \\ 9.2285 \text{ in} \\ 10.9785 \text{ in} \\ 18.2285 \text{ in} \\ 25.4785 \text{ in} \\ 32.7285 \text{ in} \end{pmatrix} \quad h = \begin{pmatrix} 86.793 \\ 66.129 \\ 54.225 \\ 40.591 \\ 36.575 \\ 30.234 \\ 28.245 \\ 25.381 \end{pmatrix} \frac{\text{kg}}{\text{K} \cdot \text{s}^3}$$



$$A_{\text{pix}} := 0.02\text{in} \cdot 0.02\text{in} = 4 \times 10^{-4} \cdot \text{in}^2$$

$$Q_{\text{CONV}} := \overrightarrow{[h \cdot A_{\text{pix}} \cdot (T_{\text{avg}} - T_{\infty})]} = \begin{pmatrix} 8.646 \times 10^{-5} \\ 8.219 \times 10^{-5} \\ 8.192 \times 10^{-5} \\ 8.087 \times 10^{-5} \\ 7.595 \times 10^{-5} \\ 7.611 \times 10^{-5} \\ 7.215 \times 10^{-5} \\ 7.944 \times 10^{-5} \end{pmatrix} \cdot W$$

$$Q_{\text{FLUX}} := \overrightarrow{\left(\frac{E \cdot I}{A_t} \cdot A_{\text{pix}}\right)} = \begin{pmatrix} 1.39 \times 10^{-4} \\ 1.39 \times 10^{-4} \\ 1.39 \times 10^{-4} \\ 1.407 \times 10^{-4} \\ 1.407 \times 10^{-4} \\ 1.376 \times 10^{-4} \\ 1.386 \times 10^{-4} \\ 1.414 \times 10^{-4} \end{pmatrix} \cdot W$$

$$Q_{\text{HL}} := \overrightarrow{\left[ \frac{k_p}{t_p} \cdot A_{\text{pix}} \cdot (T_{\text{SS}} - T_{\text{UP}}) \right]} = \begin{pmatrix} 3.789 \times 10^{-5} \\ 4.421 \times 10^{-5} \\ 4.46 \times 10^{-5} \\ 5.026 \times 10^{-5} \\ 5.546 \times 10^{-5} \\ 4.296 \times 10^{-5} \\ 4.528 \times 10^{-5} \\ 5.069 \times 10^{-5} \end{pmatrix} \text{ W} \quad Q_{\text{RAD}} := \overrightarrow{\left[ \sigma \cdot \varepsilon \cdot A_{\text{pix}} \cdot \left( T_{\text{avg}}^4 - T_{\infty}^4 \right) \right]} = \begin{pmatrix} 5.657 \times 10^{-6} \\ 7.093 \times 10^{-6} \\ 8.666 \times 10^{-6} \\ 1.151 \times 10^{-5} \\ 1.201 \times 10^{-5} \\ 1.468 \times 10^{-5} \\ 1.49 \times 10^{-5} \\ 1.822 \times 10^{-5} \end{pmatrix} \cdot \text{W}$$

$$\frac{Q_{\text{HL}}}{Q_{\text{FLUX}}} = \begin{pmatrix} 27.255 \\ 31.805 \\ 32.088 \\ 35.711 \\ 39.409 \\ 31.219 \\ 32.673 \\ 35.835 \end{pmatrix} \cdot \% \quad \frac{Q_{\text{CONV}}}{Q_{\text{FLUX}}} = \begin{pmatrix} 62.197 \\ 59.129 \\ 58.929 \\ 57.46 \\ 53.966 \\ 55.304 \\ 52.062 \\ 56.164 \end{pmatrix} \cdot \% \quad \frac{Q_{\text{RAD}}}{Q_{\text{FLUX}}} = \begin{pmatrix} 4.07 \\ 5.103 \\ 6.234 \\ 8.175 \\ 8.535 \\ 10.665 \\ 10.755 \\ 12.88 \end{pmatrix} \cdot \%$$

$$\text{mean} \left( \frac{Q_{\text{HL}}}{Q_{\text{FLUX}}} \right) = 33.249 \cdot \%$$

$$\text{mean} \left( \frac{Q_{\text{CONV}}}{Q_{\text{FLUX}}} \right) = 56.901 \cdot \%$$

$$\text{mean} \left( \frac{Q_{\text{RAD}}}{Q_{\text{FLUX}}} \right) = 8.302 \cdot \%$$

## APPENDIX C

### Test Data Tables

This appendix provides all test data for each set of heat transfer boundary conditions. For consistency a similar format to Tecson [1] was used. Figure C.1 provides a legend to identify the thermocouple for each set of data obtained, the test data is given in Tables C.2-C.17, and Table C.1 provides a legend for the parameters in the test data.

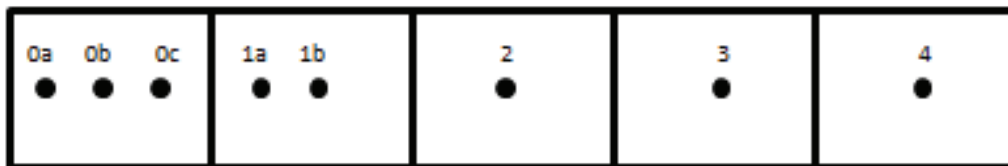


Figure C.1: Thermocouple legend

Table C.1: Parameter descriptions	
Parameter	Description
$x$	thermocouple distance from leading edge of test plate
$A_t$	area of Mylar heater
$\varepsilon$	emissivity
$\sigma$	Stefan-Boltzmann constant
$t$	Plexiglas thickness
$c_c$	conduction correction coefficient
$E$	voltage
$I$	current
$k$	system thermal conductivity
$T_{SS}$	thermocouple reading below Mylar
$T_{UP}$	thermocouple reading below Plexiglas
$T_\infty$	average freestream temperature
$T_{IR}$	one square inch IR temperature average above thermocouple set
$h$	convective heat transfer coefficient

Table C.2: Smooth-turbulent test data, constant heat flux

Parameter	0a	0b	0c	1a	1b	2	3	4
x (in)	3.10	4.48	5.85	9.23	10.98	18.23	25.48	32.73
A <sub>t</sub> (in <sup>2</sup> )	35.06	35.06	35.06	44.62	44.62	44.62	44.62	44.62
$\varepsilon$	0.95	0.95	0.95	0.95	0.95	0.95	0.95	0.95
$\sigma$ (W/m <sup>2</sup> K <sup>4</sup> )	5.67e-8	5.67e-8	5.67e-8	5.67e-8	5.67e-8	5.67e-8	5.67e-8	5.67e-8
t (in)	0.72	0.72	0.72	0.72	0.72	0.72	0.72	0.72
c <sub>c</sub>	0.90	0.90	0.90	0.90	0.90	1.05	1.10	1.05
E (V)	5.79	5.79	5.79	5.89	5.89	5.80	5.87	5.95
I (A)	2.10	2.10	2.10	2.67	2.67	2.65	2.63	2.65
k (W/mK)	0.205	0.205	0.205	0.205	0.205	0.205	0.205	0.205
T <sub>SS</sub> (K)	311.74	311.56	312.58	315.72	317.75	313.98	315.74	318.34
T <sub>UP</sub> (K)	298.65	296.28	297.16	298.34	298.58	299.12	300.09	300.82
T <sub>∞</sub> (K)	295.13	295.13	295.13	295.13	295.13	295.13	295.13	295.13
T <sub>IR</sub> (K)	299.53	300.48	301.52	303.11	303.44	305.07	305.23	306.08
h	86.79 ± 5.14	65.13 ± 2.66	54.23 ± 1.16	40.59 ± 2.21	36.58 ± 2.07	30.23 ± 1.54	28.25 ± 1.86	25.38 ± 1.63

Table C.3: Smooth-turbulent test data, decreasing heat flux

Parameter	0a	0b	0c	1a	1b	2	3	4
$x$ (in)	3.10	4.48	5.85	9.23	10.98	18.23	25.48	32.73
$A_t$ (in <sup>2</sup> )	35.06	35.06	35.06	44.62	44.62	44.62	44.62	44.62
$\varepsilon$	0.95	0.95	0.95	0.95	0.95	0.95	0.95	0.95
$\sigma$ (W/m <sup>2</sup> K <sup>4</sup> )	5.67e-8	5.67e-8	5.67e-8	5.67e-8	5.67e-8	5.67e-8	5.67e-8	5.67e-8
$t$ (in)	0.72	0.72	0.72	0.72	0.72	0.72	0.72	0.72
$c_c$	0.90	0.90	0.90	0.90	0.90	1.05	1.10	1.05
$E$ (V)	5.80	5.80	5.80	5.26	5.26	4.41	4.56	4.57
$I$ (A)	2.10	2.10	2.10	2.40	2.40	2.04	2.05	2.06
$k$ (W/mK)	0.205	0.205	0.205	0.205	0.205	0.205	0.205	0.205
$T_{ss}$ (K)	311.73	311.5	312.49	311.87	313.49	306.53	307.63	308.93
$T_{UP}$ (K)	298.60	296.17	297.03	297.65	297.77	297.37	297.90	298.25
$T_\infty$ (K)	294.97	294.97	294.97	294.97	294.97	294.97	294.97	294.97
$T_{IR}$ (K)	299.40	300.34	301.37	301.48	301.66	300.93	301.01	301.48
$h$	$86.30 \pm 5.05$	$65.90 \pm 2.63$	$54.16 \pm 1.17$	$39.69 \pm 2.80$	$36.18 \pm 2.69$	$28.61 \pm 2.26$	$28.20 \pm 2.93$	$25.17 \pm 2.22$

Table C.4: Smooth-turbulent test data, increasing heat flux

Parameter	0a	0b	0c	1a	1b	2	3	4
$x$ (in)	3.10	4.48	5.85	9.23	10.98	18.23	25.48	32.73
$A_t$ (in <sup>2</sup> )	35.06	35.06	35.06	44.62	44.62	44.62	44.62	44.62
$\varepsilon$	0.95	0.95	0.95	0.95	0.95	0.95	0.95	0.95
$\sigma$ (W/m <sup>2</sup> K <sup>4</sup> )	5.67e-8	5.67e-8	5.67e-8	5.67e-8	5.67e-8	5.67e-8	5.67e-8	5.67e-8
$t$ (in)	0.72	0.72	0.72	0.72	0.72	0.72	0.72	0.72
$c_c$	0.90	0.90	0.90	0.90	0.90	1.05	1.10	1.05
$E$ (V)	4.44	4.44	4.44	5.32	5.32	5.80	5.88	5.95
$I$ (A)	1.63	1.63	1.63	2.42	2.42	2.65	2.63	2.65
$k$ (W/mK)	0.205	0.205	0.205	0.205	0.205	0.205	0.205	0.205
$T_{ss}$ (K)	304.71	304.67	305.17	311.61	313.42	313.38	315.29	317.95
$T_{UP}$ (K)	296.67	295.22	295.77	297.16	297.38	298.58	299.68	300.43
$T_\infty$ (K)	294.57	294.57	294.57	294.57	294.57	294.57	294.57	294.57
$T_{IR}$ (K)	297.23	297.79	298.40	300.99	301.35	304.43	304.74	305.53
$h$	84.00 $\pm$ 10.5	64.07 $\pm$ 6.85	53.01 $\pm$ 3.91	41.27 $\pm$ 2.94	36.42 $\pm$ 2.67	30.62 $\pm$ 1.56	28.14 $\pm$ 1.84	25.37 $\pm$ 1.53



Table C.5: Smooth-turbulent test data, unheated starting length

Parameter	0a	0b	0c	1a	1b	2	3	4
x (in)	3.10	4.48	5.85	9.23	10.98	18.23	25.48	32.73
A <sub>t</sub> (in <sup>2</sup> )	35.06	35.06	35.06	44.62	44.62	44.62	44.62	44.62
$\varepsilon$	0.95	0.95	0.95	0.95	0.95	0.95	0.95	0.95
$\sigma$ (W/m <sup>2</sup> K <sup>4</sup> )	5.67e-8	5.67e-8	5.67e-8	5.67e-8	5.67e-8	5.67e-8	5.67e-8	5.67e-8
t (in)	0.72	0.72	0.72	0.72	0.72	0.72	0.72	0.72
c <sub>c</sub>	0.90	0.90	0.90	0.90	0.90	1.05	1.10	1.05
E (V)						5.8	5.89	6.01
I (A)						2.64	2.63	2.68
k (W/mK)	0.205	0.205	0.205	0.205	0.205	0.205	0.205	0.205
T <sub>SS</sub> (K)						312.43	314.85	317.99
T <sub>UP</sub> (K)						297.77	299.21	300.18
T <sub>∞</sub> (K)						294.96	294.96	294.96
T <sub>IR</sub> (K)						303.34	304.19	305.27
h						37.15 ± 2.00	31.66 ± 2.17	28.08 ± 1.17

Table C.6: Smooth-laminar test data, constant heat flux

Parameter	0a	0b	0c	1a	1b	2	3	4
x (in)	3.10	4.48	5.85	9.23	10.98	18.23	25.48	32.73
A <sub>t</sub> (in <sup>2</sup> )	35.06	35.06	35.06	44.62	44.62	44.62	44.62	44.62
$\varepsilon$	0.95	0.95	0.95	0.95	0.95	0.95	0.95	0.95
$\sigma$ (W/m <sup>2</sup> K <sup>4</sup> )	5.67e-8	5.67e-8	5.67e-8	5.67e-8	5.67e-8	5.67e-8	5.67e-8	5.67e-8
t (in)	0.72	0.72	0.72	0.72	0.72	0.72	0.72	0.72
c <sub>c</sub>	0.90	0.90	0.90	0.90	0.90	1.05	1.10	1.05
E (V)	5.29	5.29	5.29	5.31	5.31	5.28	5.39	5.38
I (A)	1.92	1.92	1.92	2.41	2.41	2.30	2.40	2.37
k (W/mK)	0.205	0.205	0.205	0.205	0.205	0.205	0.205	0.205
T <sub>SS</sub> (K)	310.84	312.26	312.92	315.85	316.74	314.41	317.02	317.79
T <sub>UP</sub> (K)	297.46	296.8	297.05	297.48	297.80	298.65	299.82	300.16
T <sub>∞</sub> (K)	293.24	293.24	293.24	293.24	293.24	293.24	293.24	293.24
T <sub>IR</sub> (K)	302.93	303.75	304.57	305.46	306.02	307.19	308.77	309.11
h	26.67 ± 1.98	22.10 ± 1.87	19.70 ± 1.78	15.31 ± 0.5	13.93 ± 0.4	10.96 ± 0.83	9.27 ± 0.85	8.91 ± 0.83

Table C.7: Smooth-laminar test data, decreasing heat flux

Parameter	0a	0b	0c	1a	1b	2	3	4
x (in)	3.10	4.48	5.85	9.23	10.98	18.23	25.48	32.73
A <sub>t</sub> (in <sup>2</sup> )	35.06	35.06	35.06	44.62	44.62	44.62	44.62	44.62
$\varepsilon$	0.95	0.95	0.95	0.95	0.95	0.95	0.95	0.95
$\sigma$ (W/m <sup>2</sup> K <sup>4</sup> )	5.67e-8	5.67e-8	5.67e-8	5.67e-8	5.67e-8	5.67e-8	5.67e-8	5.67e-8
t (in)	0.72	0.72	0.72	0.72	0.72	0.72	0.72	0.72
c <sub>c</sub>	0.90	0.90	0.90	0.90	0.90	1.05	1.10	1.05
E (V)	5.29	5.29	5.29	5.31	5.31	5.27	4.83	4.05
I (A)	1.92	1.92	1.92	2.41	2.41	2.37	2.16	1.80
k (W/mK)	0.205	0.205	0.205	0.205	0.205	0.205	0.205	0.205
T <sub>SS</sub> (K)	311.41	313.00	313.65	316.15	316.93	315.86	313.64	309.13
T <sub>UP</sub> (K)	297.88	297.16	297.45	297.95	298.22	299.31	299.44	298.53
T <sub>∞</sub> (K)	293.63	293.63	293.63	293.63	293.63	293.63	293.63	293.63
T <sub>IR</sub> (K)	303.18	303.95	304.76	305.85	306.42	308.05	307.20	304.59
h	27.03 ± 1.99	22.31 ± 1.88	19.89 ± 1.80	15.46 ± 0.5	14.10 ± 0.4	10.65 ± 0.81	7.88 ± 0.88	5.90 ± 0.91

Table C.8: Smooth-laminar test data, increasing heat flux

Parameter	0a	0b	0c	1a	1b	2	3	4
x (in)	3.10	4.48	5.85	9.23	10.98	18.23	25.48	32.73
A <sub>t</sub> (in <sup>2</sup> )	35.06	35.06	35.06	44.62	44.62	44.62	44.62	44.62
$\varepsilon$	0.95	0.95	0.95	0.95	0.95	0.95	0.95	0.95
$\sigma$ (W/m <sup>2</sup> K <sup>4</sup> )	5.67e-8	5.67e-8	5.67e-8	5.67e-8	5.67e-8	5.67e-8	5.67e-8	5.67e-8
t (in)	0.72	0.72	0.72	0.72	0.72	0.72	0.72	0.72
c <sub>c</sub>	0.90	0.90	0.90	0.90	0.90	1.05	1.10	1.05
E (V)	3.97	3.97	3.97	4.72	4.72	5.27	5.45	5.39
I (A)	1.46	1.46	1.46	2.16	2.16	2.37	2.43	2.38
k (W/mK)	0.205	0.205	0.205	0.205	0.205	0.205	0.205	0.205
T <sub>SS</sub> (K)	303.19	304.25	304.63	310.65	311.21	314.35	316.89	317.34
T <sub>UP</sub> (K)	295.20	295.18	295.38	296.23	296.42	298.24	299.48	299.85
T <sub>∞</sub> (K)	293.05	293.05	293.05	293.05	293.05	293.05	293.05	293.05
T <sub>IR</sub> (K)	298.89	299.36	299.83	302.32	302.96	306.65	308.45	308.72
h	24.43 ± 1.99	20.51 ± 1.88	18.40 ± 1.80	16.79 ± 0.92	14.94 ± 0.75	12.13 ± 0.87	10.04 ± 0.87	9.44 ± 0.78

Table C.9: Smooth-laminar test data, unheated started length

Parameter	0a	0b	0c	1a	1b	2	3	4
x (in)	3.10	4.48	5.85	9.23	10.98	18.23	25.48	32.73
A <sub>t</sub> (in <sup>2</sup> )	35.06	35.06	35.06	44.62	44.62	44.62	44.62	44.62
$\varepsilon$	0.95	0.95	0.95	0.95	0.95	0.95	0.95	0.95
$\sigma$ (W/m <sup>2</sup> K <sup>4</sup> )	5.67e-8	5.67e-8	5.67e-8	5.67e-8	5.67e-8	5.67e-8	5.67e-8	5.67e-8
t (in)	0.72	0.72	0.72	0.72	0.72	0.72	0.72	0.72
c <sub>c</sub>	0.90	0.90	0.90	0.90	0.90	1.05	1.10	1.05
E (V)						5.27	5.45	5.35
I (A)						2.36	2.43	2.35
k (W/mK)	0.205	0.205	0.205	0.205	0.205	0.205	0.205	0.205
T <sub>SS</sub> (K)						312.53	316.22	317.86
T <sub>UP</sub> (K)						297.51	299.26	299.90
T <sub>∞</sub> (K)						293.43	293.43	293.43
T <sub>IR</sub> (K)						306.66	308.46	308.71
h						17.62 ± 1.17	11.93 ± 0.99	8.20 ± 0.42

Table C.10: 052996 (Large Roughness) test data, constant heat flux

Parameter	0a	0b	0c	1a	1b	2	3	4
x (in)	3.10	4.48	5.85	9.23	10.98	18.23	25.48	32.73
A <sub>t</sub> (in <sup>2</sup> )	35.06	35.06	35.06	44.62	44.62	44.62	44.62	44.62
$\varepsilon$	0.95	0.95	0.95	0.95	0.95	0.95	0.95	0.95
$\sigma$ (W/m <sup>2</sup> K <sup>4</sup> )	5.67e-8	5.67e-8	5.67e-8	5.67e-8	5.67e-8	5.67e-8	5.67e-8	5.67e-8
t (in)	0.72	0.72	0.72	0.72	0.72	0.72	0.72	0.72
c <sub>c</sub>	0.90	0.90	0.90	0.90	0.90	1.05	1.10	1.05
E (V)	5.89	5.89	5.89	5.90	5.90	5.96	5.88	5.97
I (A)	2.11	2.11	2.11	2.67	2.67	2.61	2.62	2.66
k (W/mK)	0.205	0.205	0.205	0.205	0.205	0.205	0.205	0.205
T <sub>SS</sub> (K)	317.92	318.58	317.71	315.76	316.39	316.57	317.01	320.77
T <sub>UP</sub> (K)	299.47	299.99	300.26	298.88	298.60	299.89	300.65	301.53
T <sub>∞</sub> (K)	294.04	294.04	294.04	294.04	294.04	294.04	294.04	294.04
T <sub>IR</sub> (K)	298.21	299.03	299.52	300.95	300.88	300.83	301.22	301.53
h	81.45 ± 7.14	66.91 ± 4.05	62.48 ± 2.45	48.99 ± 2.95	48.22 ± 3.09	45.14 ± 3.05	40.91 ± 3.48	37.63 ± 2.93

Table C.11: 052996 (Large Roughness) test data, decreasing heat flux

Parameter	0a	0b	0c	1a	1b	2	3	4
x (in)	3.10	4.48	5.85	9.23	10.98	18.23	25.48	32.73
A <sub>t</sub> (in <sup>2</sup> )	35.06	35.06	35.06	44.62	44.62	44.62	44.62	44.62
$\varepsilon$	0.95	0.95	0.95	0.95	0.95	0.95	0.95	0.95
$\sigma$ (W/m <sup>2</sup> K <sup>4</sup> )	5.67e-8	5.67e-8	5.67e-8	5.67e-8	5.67e-8	5.67e-8	5.67e-8	5.67e-8
t (in)	0.72	0.72	0.72	0.72	0.72	0.72	0.72	0.72
c <sub>c</sub>	0.90	0.90	0.90	0.90	0.90	1.05	1.10	1.05
E (V)	5.89	5.89	5.89	5.27	5.27	4.44	4.54	4.56
I (A)	2.11	2.11	2.11	2.40	2.40	2.01	2.02	2.05
k (W/mK)	0.205	0.205	0.205	0.205	0.205	0.205	0.205	0.205
T <sub>ss</sub> (K)	318.46	319.27	318.34	312.28	312.62	308.13	308.26	310.56
T <sub>UP</sub> (K)	299.76	300.38	300.75	298.56	298.17	298.17	298.53	299.03
T <sub>∞</sub> (K)	294.19	294.19	294.19	294.19	294.19	294.19	294.19	294.19
T <sub>IR</sub> (K)	298.31	299.13	299.62	300.08	299.99	298.73	298.85	299.02
h	81.92 ± 7.52	67.06 ± 4.31	62.78 ± 2.67	45.41 ± 3.38	44.99 ± 3.57	36.87 ± 3.69	37.15 ± 4.70	33.68 ± 3.67

Table C.12: 052996 (Large Roughness) test data, increasing heat flux

Parameter	0a	0b	0c	1a	1b	2	3	4
x (in)	3.10	4.48	5.85	9.23	10.98	18.23	25.48	32.73
A <sub>t</sub> (in <sup>2</sup> )	35.06	35.06	35.06	44.62	44.62	44.62	44.62	44.62
$\varepsilon$	0.95	0.95	0.95	0.95	0.95	0.95	0.95	0.95
$\sigma$ (W/m <sup>2</sup> K <sup>4</sup> )	5.67e-8	5.67e-8	5.67e-8	5.67e-8	5.67e-8	5.67e-8	5.67e-8	5.67e-8
t (in)	0.72	0.72	0.72	0.72	0.72	0.72	0.72	0.72
c <sub>c</sub>	0.90	0.90	0.90	0.90	0.90	1.05	1.10	1.05
E (V)	4.53	4.53	4.53	5.26	5.26	5.93	5.88	5.97
I (A)	1.63	1.63	1.63	2.40	2.40	2.61	2.62	2.66
k (W/mK)	0.205	0.205	0.205	0.205	0.205	0.205	0.205	0.205
T <sub>SS</sub> (K)	308.35	308.83	308.40	310.88	311.37	316.39	316.92	320.68
T <sub>UP</sub> (K)	297.48	297.88	298.12	297.74	297.51	299.66	300.47	301.45
T <sub>∞</sub> (K)	294.15	294.15	294.15	294.15	294.15	294.15	294.15	294.15
T <sub>IR</sub> (K)	296.71	297.20	297.48	299.63	299.63	300.52	301.00	301.37
h	78.81 ± 12.83	65.06 ± 8.33	61.23 ± 6.36	50.12 ± 3.88	48.80 ± 3.96	47.96 ± 3.38	42.93 ± 3.78	39.17 ± 2.97



Table C.13: 052996 (Large Roughness) test data, unheated starting length

Parameter	0a	0b	0c	1a	1b	2	3	4
x (in)	3.10	4.48	5.85	9.23	10.98	18.23	25.48	32.73
A <sub>t</sub> (in <sup>2</sup> )	35.06	35.06	35.06	44.62	44.62	44.62	44.62	44.62
ε	0.95	0.95	0.95	0.95	0.95	0.95	0.95	0.95
σ (W/m <sup>2</sup> K <sup>4</sup> )	5.67e-8	5.67e-8	5.67e-8	5.67e-8	5.67e-8	5.67e-8	5.67e-8	5.67e-8
t (in)	0.72	0.72	0.72	0.72	0.72	0.72	0.72	0.72
c <sub>c</sub>	0.90	0.90	0.90	0.90	0.90	1.05	1.10	1.05
E (V)						5.91	5.89	5.97
I (A)						2.63	2.63	2.67
k (W/mK)	0.205	0.205	0.205	0.205	0.205	0.205	0.205	0.205
T <sub>SS</sub> (K)						314.76	315.65	319.57
T <sub>UP</sub> (K)						298.23	299.49	300.54
T <sub>∞</sub> (K)						293.71	293.71	293.71
T <sub>IR</sub> (K)						299.90	300.61	301.08
h						50.28 ± 3.54	43.30 ± 3.73	38.90 ± 2.33

Table C.14: 053096 (Small Roughness) test data, constant heat flux

Parameter	0a	0b	0c	1a	1b	2	3	4
x (in)	3.10	4.48	5.85	9.23	10.98	18.23	25.48	32.73
A <sub>t</sub> (in <sup>2</sup> )	35.06	35.06	35.06	44.62	44.62	44.62	44.62	44.62
$\varepsilon$	0.95	0.95	0.95	0.95	0.95	0.95	0.95	0.95
$\sigma$ (W/m <sup>2</sup> K <sup>4</sup> )	5.67e-8	5.67e-8	5.67e-8	5.67e-8	5.67e-8	5.67e-8	5.67e-8	5.67e-8
t (in)	0.72	0.72	0.72	0.72	0.72	0.72	0.72	0.72
c <sub>c</sub>	0.90	0.90	0.90	0.90	0.90	1.05	1.10	1.05
E (V)	5.92	5.92	5.92	5.91	5.91	5.82	5.87	5.98
I (A)	2.10	2.10	2.10	2.68	2.68	2.65	2.60	2.68
k (W/mK)	0.205	0.205	0.205	0.205	0.205	0.205	0.205	0.205
T <sub>SS</sub> (K)	318.28	319.42	317.08	311.15	313.11	313.39	312.23	316.11
T <sub>UP</sub> (K)	298.59	297.28	297.93	297.80	297.84	298.86	299.15	300.17
T <sub>∞</sub> (K)	293.80	293.80	293.80	293.80	293.80	293.80	293.80	293.80
T <sub>IR</sub> (K)	304.21	305.65	303.35	301.41	301.71	302.58	303.15	304.30
h	27.87 ± 2.01	21.64 ± 1.88	31.50 ± 2.09	48.94 ± 2.17	44.44 ± 2.11	35.82 ± 1.91	33.65 ± 2.07	29.31 ± 1.75

Table C.15: 053096 (Small Roughness) test data, decreasing heat flux

Parameter	0a	0b	0c	1a	1b	2	3	4
x (in)	3.10	4.48	5.85	9.23	10.98	18.23	25.48	32.73
A <sub>t</sub> (in <sup>2</sup> )	35.06	35.06	35.06	44.62	44.62	44.62	44.62	44.62
ε	0.95	0.95	0.95	0.95	0.95	0.95	0.95	0.95
σ (W/m <sup>2</sup> K <sup>4</sup> )	5.67e-8	5.67e-8	5.67e-8	5.67e-8	5.67e-8	5.67e-8	5.67e-8	5.67e-8
t (in)	0.72	0.72	0.72	0.72	0.72	0.72	0.72	0.72
c <sub>c</sub>	0.90	0.90	0.90	0.90	0.90	1.05	1.10	1.05
E (V)	5.92	5.92	5.92	5.27	5.27	4.43	4.48	4.56
I (A)	2.10	2.10	2.10	2.41	2.41	2.05	2.00	2.07
k (W/mK)	0.205	0.205	0.205	0.205	0.205	0.205	0.205	0.205
T <sub>SS</sub> (K)	318.28	319.24	316.92	307.67	309.34	305.69	304.96	307.08
T <sub>UP</sub> (K)	298.55	297.26	297.96	297.30	297.08	297.14	297.27	297.86
T <sub>∞</sub> (K)	294.08	294.08	294.08	294.08	294.08	294.08	294.08	294.08
T <sub>IR</sub> (K)	304.38	305.98	303.51	300.30	300.52	299.86	300.01	300.66
h	28.30 ± 2.01	21.75 ± 1.88	32.27 ± 2.09	48.33 ± 2.71	43.55 ± 2.69	31.53 ± 2.39	30.87 ± 2.83	27.64 ± 2.18

Table C.16: 053096 (Small Roughness) test data, increasing heat flux

Parameter	0a	0b	0c	1a	1b	2	3	4
x (in)	3.10	4.48	5.85	9.23	10.98	18.23	25.48	32.73
A <sub>t</sub> (in <sup>2</sup> )	35.06	35.06	35.06	44.62	44.62	44.62	44.62	44.62
ε	0.95	0.95	0.95	0.95	0.95	0.95	0.95	0.95
σ (W/m <sup>2</sup> K <sup>4</sup> )	5.67e-8	5.67e-8	5.67e-8	5.67e-8	5.67e-8	5.67e-8	5.67e-8	5.67e-8
t (in)	0.72	0.72	0.72	0.72	0.72	0.72	0.72	0.72
c <sub>c</sub>	0.90	0.90	0.90	0.90	0.90	1.05	1.10	1.05
E (V)	4.59	4.59	4.59	5.28	5.28	5.81	5.88	5.98
I (A)	1.64	1.64	1.64	2.41	2.41	2.65	2.60	2.68
k (W/mK)	0.205	0.205	0.205	0.205	0.205	0.205	0.205	0.205
T <sub>SS</sub> (K)	308.30	308.91	307.72	307.50	309.07	313.05	311.98	315.89
T <sub>UP</sub> (K)	296.79	295.99	296.38	296.80	296.86	298.55	298.96	299.99
T <sub>∞</sub> (K)	293.89	293.89	293.89	293.89	293.89	293.89	293.89	293.89
T <sub>IR</sub> (K)	300.65	301.56	299.94	299.79	300.12	302.14	302.86	304.03
h	26.30 ± 2.04	20.61 ± 2.00	30.36 ± 1.93	50.99 ± 3.11	45.52 ± 2.90	38.56 ± 2.10	35.55 ± 2.22	30.60 ± 1.73

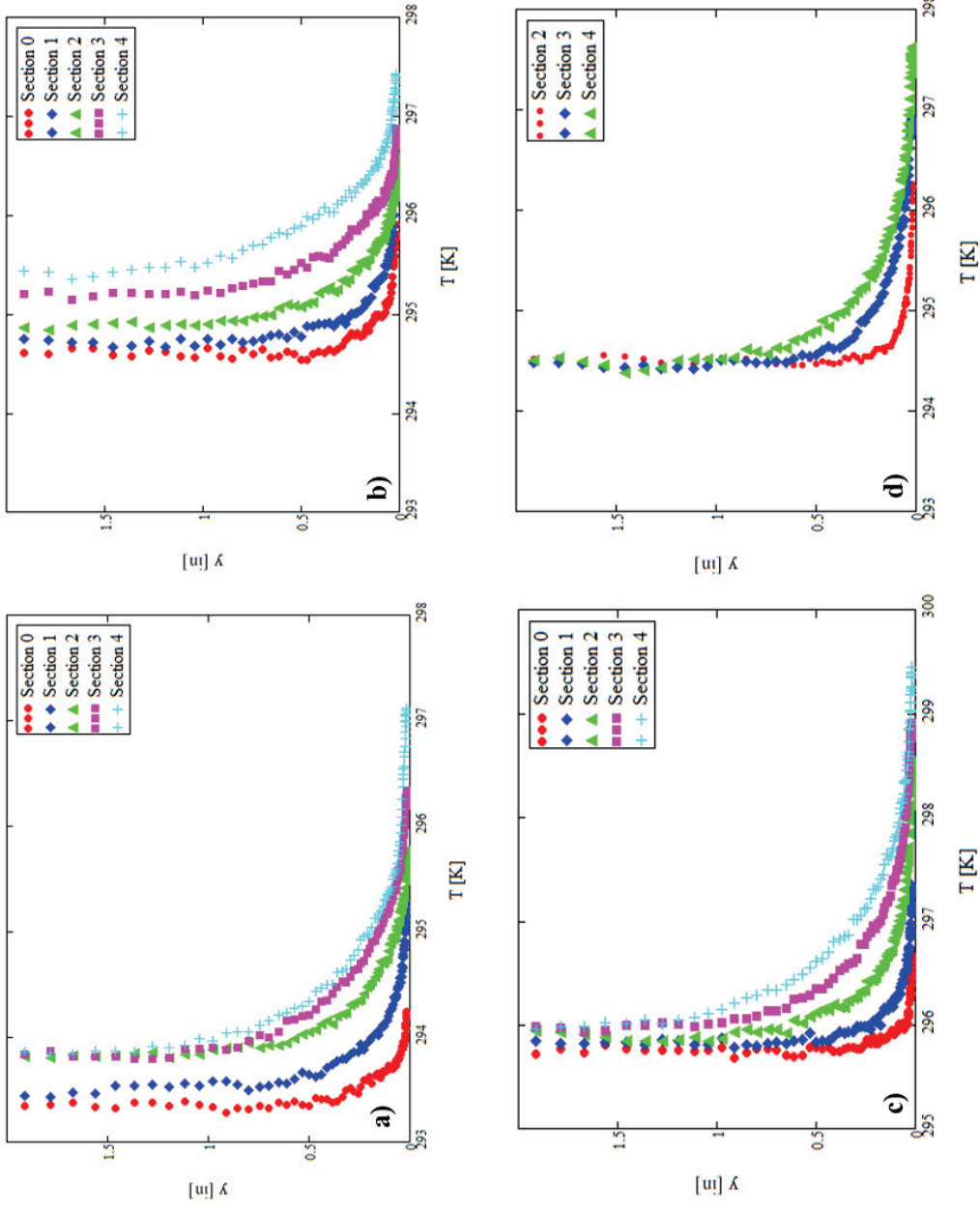
Table C.17: 053096 (Small Roughness) test data, unheated starting length

Parameter	0a	0b	0c	1a	1b	2	3	4
x (in)	3.10	4.48	5.85	9.23	10.98	18.23	25.48	32.73
A <sub>t</sub> (in <sup>2</sup> )	35.06	35.06	35.06	44.62	44.62	44.62	44.62	44.62
$\varepsilon$	0.95	0.95	0.95	0.95	0.95	0.95	0.95	0.95
$\sigma$ (W/m <sup>2</sup> K <sup>4</sup> )	5.67e-8	5.67e-8	5.67e-8	5.67e-8	5.67e-8	5.67e-8	5.67e-8	5.67e-8
t (in)	0.72	0.72	0.72	0.72	0.72	0.72	0.72	0.72
c <sub>c</sub>	0.90	0.90	0.90	0.90	0.90	1.05	1.10	1.05
E (V)						5.81	5.90	5.98
I (A)						2.65	2.62	2.68
k (W/mK)	0.205	0.205	0.205	0.205	0.205	0.205	0.205	0.205
T <sub>SS</sub> (K)						311.68	311.07	315.08
T <sub>UP</sub> (K)						297.31	298.11	299.30
T <sub>∞</sub> (K)						293.36	293.36	293.36
T <sub>IR</sub> (K)						300.91	302.14	303.43
h						42.77 ± 2.41	37.17 ± 2.31	31.01 ± 1.23

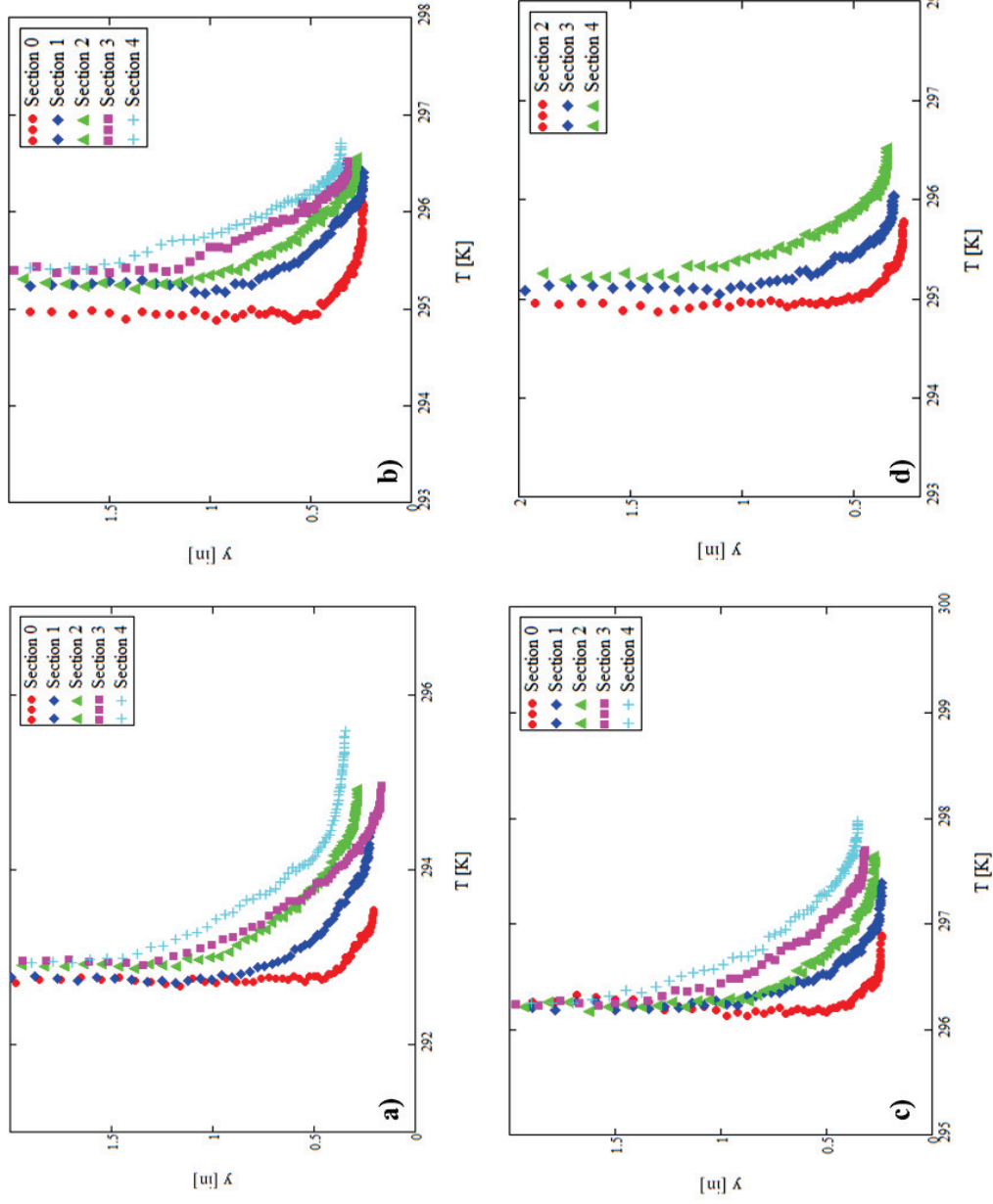
## APPENDIX D

### Boundary Layer Traces

This Appendix provides the full set of thermal boundary layer traces performed for the decreasing, increasing, and unheated starting length boundary conditions. These traces were performed at the center of each test section. For consistency, a similar format to Tecson [5] was used. Figures D.1- D.9 are the raw boundary layer traces, and Figures D.10- D.18 are the nondimensionalized boundary layer traces.

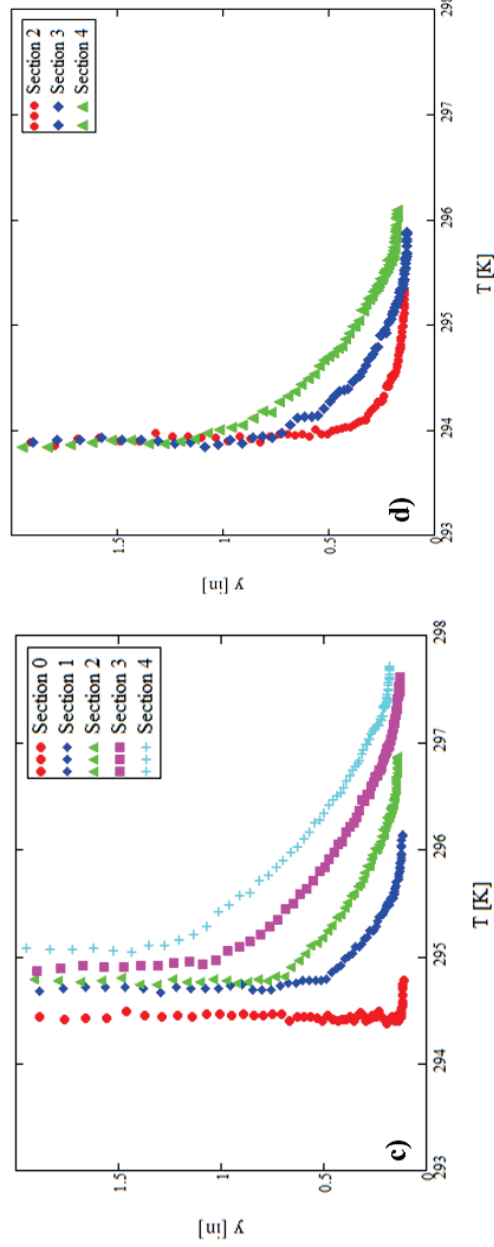
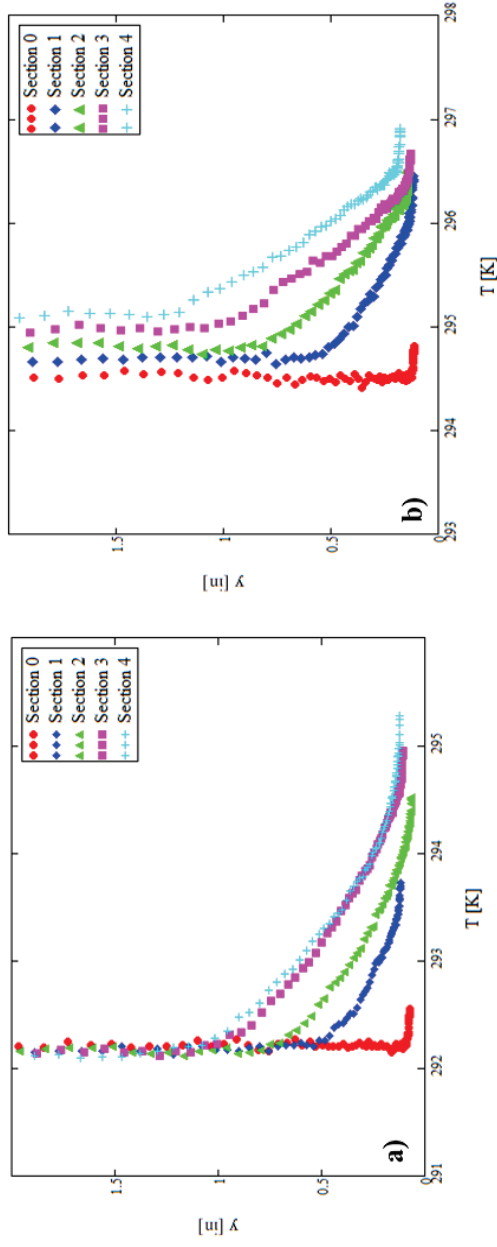


D.1: Smooth-turbulent, raw thermal boundary layer traces for the a) constant heat flux, b) decreasing heat flux, c) increasing heat flux, and d) unheated starting length



D.2: 052996, raw thermal boundary layer traces for the a) constant heat flux, b) decreasing heat flux, c) increasing heat flux, and d) unheated starting length





D.3: 053096, raw thermal boundary layer traces for the a) constant heat flux, b) decreasing heat flux, c) increasing heat flux, and d) unheated starting length

## REFERENCES

- [1] National Transportation Safety Board, 1994, "In-Flight Icing Encounter and Loss of Control."
- [2] Messinger, B. L., 1952, "Equilibrium Temperature of an Unheated Icing Surface as a function of Air Speed," *Lockheed Aircraft Corporation*.
- [3] Nikuradse, J., 1933, "Laws of Flow in Rough Pipes," *VDI-Forschungsheft*, 4, p. 361.
- [4] Schlichting, H., 1936, "Experimental Investigation of the Problem of Surface Roughness," TM-832, National Advisory Committee on Aeronautics.
- [5] Tecson, L., 2013, "Convective Heat Transfer from Realistic Ice Roughness Distributions," MS thesis, Department of Mechanical Engineering, Baylor University.
- [6] McClain, S. T., Vargas, M., Kreeger, R. E., Tsao, J., 2007, "Heat Transfer from Protuberances," *Journal of Thermophysics and Heat Transfer*, **21**(2), pp. 337-345.
- [7] Henry, R. C., Hansman, R. J., Breuer, K. S., 1995, "Heat Transfer Variation on Protuberances and Surface Roughness Elements," *Journal of Thermophysics and Heat Transfer*, **9**(1), pp. 175-180.
- [8] Olsen, W., Walker, E., 1986, "Experimental Evidence for Modifying the Current Physical Model for Ice Accretion on Aircraft Surfaces," NASA TM-87184.
- [9] Anderson, D. N., Shin, J., 1997, "Characterization of Ice Roughness from Simulated Icing Encounters," NASA TM 107400.
- [10] Vargas, M., 2007, "Current Experimental Basis for Modeling Ice Accretions on Swept Wings," *Journal of Aircraft*, **44**(1), pp. 274-290.
- [11] Vargas, M., Tsao, J., 2007, "Observations on the Growth of Roughness Elements Into Icing Feathers," AIAA Paper 2007-0900.
- [12] NASA, 2013, "Icing Branch Gallery,"  
[http://icebox.grc.nasa.gov/gallery/images/C95\\_03918.html](http://icebox.grc.nasa.gov/gallery/images/C95_03918.html)
- [13] Lewis, J. P., Bowden, D.T., 1952, "Preliminary Investigation of Cyclic De-Icing of an Airfoil Using an External Electric Heater," NACA RM E51J30.

- [14] Von Glahn, U. H., Gray, V.H., 1954, "Effect of Ice Formations on Section Drag of a Swept NACA 63A-009 Airfoil with Partial-Span Leading-Edge Slat for Various Modes of Thermal Ice Protection," NACA RM E53J30.
- [15] Wilder, R. W., 1978, "A Theoretical and Experimental Means to Predict Ice Accretion Shapes for Evaluating Aircraft Handling and Performance Characteristics," AGARD Advisory Report No. 127, Aircraft Icing.
- [16] Reehorst, A.L., 1992, "Prediction of Ice Accretion on a Swept NACA 0012 Airfoil and Comparisons to Flight Test Results," AIAA Paper 92-0043.
- [17] Hedde, T., Guffond, D., 1993, "Improvement of the ONERA 3D Icing Code, Comparison with 3D Experimental Shapes," AIAA Paper 93-E53J30.
- [18] Vargas, M., Reshotko, E., 1998, "Physical Mechanisms of Glaze Ice Scallop Formation on Swept Wings," AIAA Paper 98-0491.
- [19] Vargas, M., Reshotko, E., 2000, "LWC and Temperature Effects on Ice Accretion Formation on Swept Wings at Glaze Ice Conditions," AIAA Paper 2000-00483.
- [20] Vargas, M., Reshotko, E., 1999, "Parametric Experimental Study of the Formation of Glaze Ice Shapes on Swept Wings," AIAA Paper 99-0094.
- [21] Hansman, R. J., Yamaguchi, K., Berkowitz, B., Potapczuk, M., 1989, "Modeling of Surface Roughness Effects on Glaze Ice Accretion," *Journal of Thermophysics*, 5(1), pp. 54-60.
- [22] Wright, W. B., Potapczuk, M.G., 2004, "Semi-Empirical Modeling of SLD Physics," AIAA Paper 2004-0412.
- [23] Shin, J., 1994, "Characteristics of Surface Roughness Associated with Leading Edge Ice Accretion," AIAA Paper 94-0799.
- [24] Bragg, M. B., Hutchison, T., Merret, J., Oltman, R., Pokhariyal, D., 2000, "Effect of Ice Accretion on Aircraft Flight Dynamics, AIAA Paper 2000-0360.
- [25] Anderson, D. N., Hentschel, D. B., Ruff, G. A., 2003, "Measurement and Correlation of Ice Accretion Roughness," AIAA Paper 98-0486.
- [26] Tsao, J., Anderson, D. N., 2006, "Latest Developments in SLD Scaling," AIAA Paper 2005-5187.
- [27] Van Fossen, G. J., Simoneau, R. J., Olsen, W. A., Shaw, K. J., 1984, "Heat Transfer Distributions around Nominal Ice Accretion Shapes Formed on a Cylinder in the NASA Lewis Icing Research Tunnel," NASA TM 83557.

- [28] Pais, M. R., 1988, "Local Heat-Transfer Characteristics of Glaze-Ice Accretions on an NACA 0012 Airfoil," *Journal of Aircraft*, **25**(12), pp. 1136-1141.
- [29] Poinssatte, P. E., Van Fossen, G. J., DeWitt, K. J., 1990, "Convective Heat Transfer measurements from a NACA 0012 Airfoil in Flight and in the NASA Lewis Icing Research Tunnel," AIAA Paper 90-0199.
- [30] Bragg, M. B., Cummings, M. J., Lee, S., Henze, C. M., 1996, "Boundary-Layer and Heat-Transfer Measurements on an Airfoil with Simulated Ice Roughness," AIAA Paper 96-0866.
- [31] Dukhan, N., Van Fossen, G. J., DeWitt, K. J., Masiulaniec, K. C., 2003, "Experimental Frossling Numbers for Ice-Roughened NACA 0012 Airfoils," *Journal of Aircraft* **40**(6), pp. 1161-1167.
- [32] McClain, S. T., Vargas, M., Kreeger, R. E., Tsao, J., 2007, "Heat Transfer from Protuberances," *Journal of Thermophysics and Heat Transfer*, **21**(2), pp. 337-345.
- [33] Henry, R. C., Guffond, D., Garnier, F., Bouveret, A., 2000, "Heat Transfer Coefficient Measurement on Iced Airfoil in Small Icing Wind Tunnel," *Journal of Thermophysics and Heat Transfer*, **14**(3), pp. 348-354.
- [34] Tecson, L., McClain, S. T., 2013, "Modeling of Realistic Ice Roughness Element Distributions to Characterize Convective Heat Transfer," AIAA Paper 2013-3059.
- [35] Mart, S. R., 2011, "The Effect of Roughness Element Thermal Conductivity on Turbulent Convection," Master's thesis, Department of Mechanical Engineering, Baylor University.
- [36] The International Association for the Properties of Water and Steam, 2007, "Revised Release on the IAPWS Industrial Formulation 1997 for the Thermodynamic Properties of Water and Steam," <http://www.iapws.org/>.
- [37] White, F. M., 2006, *Viscous Fluid Flow*, 3rd Ed, Boston, McGraw-Hill, Inc., New York, NY.
- [38] Wilke, C. R., 1950, "A Viscosity Equation for Gas Mixtures," *Journal of Chemical Physics*, **18**(4), pp. 517-519.
- [39] Coleman, H. W., and Steele, W. G., 1999, *Experimentation and Uncertainty Analysis for Engineers*, 2nd ed., John Wiley and Sons, Inc., Hoboken, NJ.